KU LEUVEN

ARENBERG DOCTORAL SCHOOL
Faculty of Science

Evolution of nuclear structure of germanium isotopes around $N = 40$

CERN-THESIS-2021-257
//2021

Anastasios Kanellakopoulos

Supervisor:
Prof. dr. G. Neyens

Dissertation presented in partial fulfilment of the requirements for the degree of Doctor of Science (PhD): Physics

September 2021

Evolution of nuclear structure of germanium isotopes around $N = 40$

Anastasios KANELLAKOPOULOS

Examination committee:
Prof. dr. K. Temst, chair
Prof. dr. G. Neyens, supervisor
Prof. dr. P. Van Duppen
Prof. dr. N. Severijns
Prof. dr. X.F. Yang
(Peking University)
Dr. M. Kowalska
(CERN)

Dissertation presented in partial fulfilment of the requirements for the degree of Doctor of Science (PhD): Physics

September 2021

Uitgegeven in eigen beheer, Anastasios Kanellakopoulos, Celestijnenlaan 200D box 2418, B-3001 Leuven (Belgium)

To my sisters,
Amanda and Dora

Acknowledgements

It was January 2017 when I joined IKS to start my PhD studies. I've spent time both at Leuven and CERN and I've met some amazing people along the way. After almost four and a half years this journey is coming to an end and only the sweet memories will remain. Paraphrasing a famous quote: A PhD is about the people you meet along the way.

First of, I must thank my supervisor, Gerda Neyens, for giving me the opportunity to do my PhD studies at KU Leuven and join the IKS team.

Secondly, I'd like to acknowledge the assistance of the members of my committee: the chair, Prof. Dr. Kristiaan Temst, the assessors, Prof. Dr. Nathal Severijns and Prof. Dr. Piet Van Duppen, and the additional jury members, Dr. Magdalena Kowalska and Prof. Dr. Xiaofei Yang.

Naturally, a big and sincere thanks goes to Xiaofei for all the help and valuable input all along the way to the end of this PhD. It was such a joy working with you.

Of course, the biggest thanks goes to Mark for always painstakingly replying my countless questions and all the valuable things that he taught me during my stay at CERN.

I would also like to thank all the members of the COLLAPS collaboration, especially those that helped with their participation in my experiment. I am grateful for all the input that you - Klaus, Wilfred, Rainer, Deyan and Bradley - offered me during these years.

A great thanks to all the people of ISOLDE, the technical group, the target group and the operators. A special thanks to Alberto for coming

a couple of times on a Sunday evening to attempt to fix a dead target. Jenny, thank you for all the help with the CERN administration.

And another great thanks to all the secretary and IT people of IKS: Fabienne, Isabelle, Danielle, Luc and Bert, you have all been more than helpful.

Moreover, I would like to express my gratitude to my colleagues at CERN. Liss, Agi, Kati, Dinko, Frank, Simon Sels, Jared, Maxime and Victoria, thank you very much for the many coffee breaks, after-work drinks, etc., we enjoyed together. Your contribution all along the way was invaluable in many levels beyond just the scientific one.

Along these lines, I'd also like to thank my CERN lunch group: Elpida, Biagio and Patrycja. I really enjoyed all these interesting and funny conversations over lunch and beyond.

As my PhD studies time was split between IKS and CERN, I would like to extend my gratitude to my colleagues at IKS as well. Koen, Greg, Tiago, Ivan, Simon Stegemann, Oleksii, Sandro, Jonas, Ruben, Kristof, Wouter, thank you for all the after-work drinks that made my time in Leuven unforgettable.

And, of course, I can't forget my KU Leuven lunch group: Dragan, Peter, Xu and Milica, it was so much fun hanging out with you.

Dragan and Peter, I think I will not be able to ever again visit Ios after what happened during our visit there. Thank you very much both for all the memories.

Evangelia, our dinners in Cuore was something to look forward when I was visiting Leuven. Dimitris, Dimitris and Magda, the Sunday coffees were the best way to finish my visits there. Thank you all.

As per her request, a single paragraph just for my dearest Belgian, Elise. Well, thank you for teaching me all the intricacies of Belgian culture, like what is a bubble; I still can't apply it in practice. I'll never forget the countless rejections from you and the wildest Monday-morning stories. Dank je wel.

Maxime, I still remember the day you introduced yourself to IKS. On that moment I knew what would follow. Thank you for all the laughs we

had together and for your important help on the many instances when Elise was simply stating: “I don’t get it!”.

Marek, mon chérie, what can I say. Words are not enough... Thanks you so much for all the beers all around Europe, the phone calls, the discussions, the help, for everything.

Varvara, one more academic step we took together. It was so much fun being together at CERN. Thank you for all the help on every aspect of my stay at CERN. Thank you for all the discussions and putting up with my mood.

Lina, I am so grateful that I got to meet you during my stay at CERN and I am so pleased that we get to work together now. Thanks for all the Coronas we enjoyed at R1 and all the advice and guidance.

Theo, thank you very much for being a real mentor and guided me down the path of (nuclear) physics. I miss hanging out to your office and discuss.

Of course a big thanks goes to my good friends from Greece that made the COVID quarantine time so much fun: Filios, Yiota, Gery, Petros, Anastasia, you gave a brighter tone to that difficult time.

Finally, I owe a great “Thank you!” to my family. To my parents: Μαμά, μπαμπά, σας ευχαριστώ τόσο πολύ. To my two sweet sisters: Αδερφούλες μου, σας αγαπώ πολύ πολύ.

Thank you all,
Tassos

August 2021, Athens

Abstract

Collinear laser spectroscopy measurements were performed on $^{68-74}$Ge isotopes ($Z = 32$) using the COLLAPS setup at ISOLDE/CERN. The hyperfine structure of the $4s^2 4p^2\ ^3P_1 \rightarrow 4s^2 4p5s\ ^3P_1^o$ transition in the germanium atom was probed with laser light of 269 nm, produced by combining the frequency-mixing and frequency-doubling techniques. A detailed analysis of the hyperfine spectra of ^{69}Ge, led to revised values of its magnetic and quadrupole moments, which deviate significantly from the results from an earlier study using the atomic beam magnetic resonance technique. The experimental moments of ^{69,71,73}Ge agree well with the effective single-particle value for an odd neutron in respectively the $\nu f_{5/2}$, $\nu p_{1/2}$ and $\nu g_{9/2}$ orbit, using $g_s^{\text{eff}} = 0.7\ g_s^{\text{free}}$, which might suggest rather pure configurations. However, a comparison with large-scale shell-model calculations using the JUN45 interaction, with ^{56}Ni as a core and neutrons limited to $N = 50$, reveal rather mixed wave-functions. Through a comparison of the odd-N isotope magnetic and quadrupole moments with neighbouring isotones, the structural change from the single-particle nature of nickel to deformation in germanium is further investigated around $N = 40$. The experimental mean square charge radii of $^{68-74}$Ge are compared with the droplet model values revealing a weak subshell effect at $N = 40$ and an increased collectivity in the germanium isotopes, as compared to their lower-Z isotones. The odd-even staggering of the radii of the germanium isotopes is found to be larger than for the other isotopes in the region, with less than 40 neutrons. While only one value is available beyond $N = 40$, this value suggests a weakening of the odd-even staggering, but more neutron-rich data are needed to confirm this.

Beknopte samenvatting

Collineair laser spectroscopie experimenten werden uitgevoerd op $^{68-74}$Ge-isotopen ($Z = 32$) met behulp van de COLLAPS-opstelling op ISOLDE/CERN. De hyperfijnstructuur van de $4s^2 4p^2\ ^3P_1 \rightarrow 4s^2 4p 5s\ ^3P_1^o$ transitie in het germaniumatoom werd onderzocht met laserlicht van 269 nm, geproduceerd door het combineren van frequentiemenging- en frequentieverdubbelingstechnieken. Een gedetailleerde analyse van de hyperfijnspectra van ^{69}Ge leidde tot herziene waarden voor het magnetische dipoolmoment en het elektrische quadrupoolmoment, die significant afwijken van de resultaten van een eerdere studie met behulp van de atomaire-bundel magnetische resonantie techniek. De experimentele momenten van ^{69,71,73}Ge komen goed overeen met de effectieve enkeldeeltjeswaarde voor een oneven neutron in respectievelijk de $\nu f_{5/2}$, $\nu p_{1/2}$ en $\nu g_{9/2}$ orbitaal, met $g_s^{\text{eff}} = 0.7\ g_s^{\text{free}}$, wat vrij zuivere configuraties zou kunnen suggereren. Een vergelijking met grootschalige schillenmodelberekeningen met behulp van de JUN45-interactie, met een ^{56}Ni romp en neutronen beperkt tot $N = 50$, onthult echter nogal gemengde golffuncties. Door een vergelijking van de magnetische dipoolmomenten en de elektrische quadrupoolmomenten van het oneven-N isotopen met deze van naburige isotonen, wordt de structurele verandering rond $N = 40$ als functie van het aantal protonen onderzocht. De experimentele gemiddelde kwadratische ladingsstralen van $^{68-74}$Ge worden vergeleken met de waarden van het druppelmodel. Deze vergelijking onthult een zwak subschil effect bij $N = 40$ en een verhoogde collectiviteit in de germaniumisotopen in vergelijking met hun lagere-Z isotonen. De oneven-even effecten in de ladingsstralen van de germaniumisotopen met minder dan 40 neutronen blijkt groter te

zijn dan voor de andere isotopen in de regio. Hoewel er slechts één waarde beschikbaar is na $N = 40$, suggereert deze waarde een afname van het oneven-even verschil in de ladingsstralen, maar er zijn meer neutronenrijke data nodig om dit te bevestigen.

List of Abbreviations

CEC Charge Exchange Cell.

CERN Organisation européenne pour la recherche nucléaire - European Organization for Nuclear Research.

CLS Collinear Laser Spectroscopy.

CoG Centre of Gravity.

COLLAPS Collinear Laser Spectroscopy Beamline.

FWHM Full Width at Half Maximum.

g.s. ground state.

hfa Hyperfine Anomaly.

hfs Hyperfine Structure.

HRS High Resolution Seperator.

IS Isotope Shift.

ISCOOL ISOLDE Beam Cooler.

ISOLDE Isotope Separation Online Device.

OES odd-even staggering effect.

OES odd-even staggering.

PMT Photomultiplier Tube.

SP single particle.

TOF time-of-flight.

Contents

List of Figures

List of Tables

Chapter 1

Introduction

I like to imagine that it was a summer evening in Athens during the late 5th century BCE when Democritus first discussed with Leucippus the idea of an atom. They were probably walking under the sacred hill of Acropolis, with the newly built Parthenon looming above them, granting the city-state of Athens its divine protection.

Democritus and his mentor Leucippus came up with the idea that the universe is composed by fundamental components called atoms (from the greek word ἄτομον, *atomon* meaning uncuttable or indivisible), giving birth to the natural philosophical movement of atomism. The basic principles of this movement were that the atoms are indestructible, always in motion and the space between them is empty. They are invisible to the naked eye, there is an infinite number of atoms in the universe and everything is composed of them.

This idea stayed dormant for centuries, only to be revived in the early 17th century with Galileo Galilei being one of the most famous advocates. In the late 18th century, the idea of atom started entering modern science, culminating with Dalton, formulating the modern atomic theory at the end of the 18th century - beginning of the 19th century. But in 1897, J.J. Thompson discovered the "corpuscle", later renamed as electron, a negatively-charged particle 1800 times smaller than that of hydrogen, the smallest atom. J.J. Thompson proposed that the atoms were divisible, where the negatively-charged electrons were distributed in a uniform sea

of positive charge, which came to be the plum pudding atomic model.

In 1909, the plum pudding model of Thomspon was disproved by Lord Ernest Rutherford and his students Hans Geiger and Ernest Marsden in the famous gold foil experiment. In this experiment, by observing the scattering angle of α-particles from a thin golden foil to large and even backward angles, Rutherford concluded that the atom consisted of mostly empty space, with all of its positive charge concentrated in its centre in a very tiny volume, surrounded by a cloud of electrons. This positively charged tiny space, occupied by positively charged particles, named protons, was the atomic nucleus and gave birth to a whole new area of physics, namely the nuclear physics.

Thus, the incredible discoveries in physics of the early 20th century have begun. In 1931, James Chadwick discovered the neutron, a neutral particle making up the atomic nuclei along with protons, and thus complete the components of a nucleus. One discovery was followed by another, until 1949 when the development of the nuclear shell model, by Eugene Paul Wigner, Maria Goeppert Mayer and J. Hans D. Jensen, changed our perspective of the nucleus.

The nuclear shell model is analogous to the atomic shell model, with an important difference: the spin-orbit interaction is the key of its success. Protons and neutrons are occupying the lowest energy available orbital. The shells for protons and for neutrons are independent of each other. When adding nucleons (protons or neutrons) to a nucleus, there are certain points where the binding energy of the next nucleon is significantly less than the last one. These points correspond to the number of nucleons 2, 8, 20, 28, 50, 82 and 126 are being called “magic numbers”. Therefore, “magic nuclei” exist where one nucleon type is at a “magic number”, and “doubly magic nuclei”, where both are “magic”. This was the first model that was predicting all the magic numbers across the known nuclei at the time and its success was its predictive power of the spin and parity of nuclear ground states, and to some extent their excited states.

Many experiments were performed in the effort to understand this system better. With the advent of radioactive beam facilities and new experimental techniques, the validity of the shell model was put to test

and was severely challenged. One such radioactive beam facility that has systematically pushed the boundaries of our knowledge in the nuclear structure field is the ISOLDE facility, at CERN, Switzerland. ISOLDE has yielded a wealth of experimental results since its creation in 1957 that have contributed in the development of nuclear theories.

Magic numbers seemed to disappear and new ones were appearing when moving away from stability. By changing the number of neutrons in a nucleus, its properties change and reveal unexpected phenomena previously unknown. Studying the structure of these nuclei can help us shed some light on the origin of these phenomena. In order to do that we need reliable high-resolution experimental techniques. One such technique is the collinear laser spectroscopy, which gives us access to the nuclear moments and charge radii, observables that can help us understand the inner machinations of the nucleus.

One such region of interesting nuclear phenomena appearing, is the region above the major proton shell closure at $Z = 28$, known as the nickel region. In this work, the experimental campaign for measuring the nuclear moments and charge radii of the germanium isotopes ($Z = 32$) around stability will be discussed. The outline of this work is as follows: in Chapter 3 the physics case and motivation behind this measurement will be presented and in Chapter 2, concepts of nuclear and atomic physics theory will be given, while bridging the two physics domains. In Chapter 4, the experimental setup will be presented, followed by Chapter 5, where the analysis procedure will be explained. Finally, in Chapter 6, the nuclear moments and charge radii results will be presented followed by a discussion and finally in Chapter 7, the conclusions will be presented next to the future outlook for the physics in this region.

In this thesis, a peer-reviewed article is presented. Article I is added to Section 6 and summarises the analysis, results and comparison to theory of the nuclear moments of the odd-A germanium isotopes, i.e. ^{69,71,73}Ge.

I. Nuclear moments of germanium isotopes near N = 40,
A. Kanellakopoulos, X. F. Yang, M. L. Bissell, M. L. Reitsma, S. W. Bai, J. Billowes, K. Blaum, A. Borschevsky, B. Cheal, C. S. Devlin, R. F. Garcia Ruiz, H. Heylen, S. Kaufmann, K. König, Á. Koszorús, S. Lechner, S. Malbrunot-Ettenauer, R. Neugart, G.

Neyens, W. Nörtershäuser, T. Ratajczyk, L. V. Rodríguez, S. Sels, S. J. Wang, L. Xie, Z. Y. Xu, and D. T. Yordanov,
Physical Review C **102**, 054331 – *Published 30 November 2020*

Chapter 2

Concepts of nuclear and atomic physics

In this chapter, basic concepts of nuclear and atomic physics will be presented. First, a general introduction to the nuclear many-body problem will be given, followed by an explanation of the nuclear properties under investigation in this thesis. Then, an introduction to the hyperfine interaction in the atom will be presented. Using the hyperfine interaction and studying the electromagnetic effects arising from it, nuclear observables can be extracted to be used to understand the nuclear structure of the atomic nucleus.

2.1 The Nucleus: A Many-Body Problem

The atomic nucleus is a complex quantum system. It consists of multiple protons and neutrons that are all interacting with one another under the strong nuclear, electromagnetic and weak nuclear interactions. But the ingredients of the nucleus, i.e. the protons and neutrons, are not fundamental particles. These, in their turn, are consisting each of 3 quarks where their interaction is described by the Quantum Chromodynamics (QCD) theory. Nevertheless, using QCD as a starting point to solve the many-body problem of the nucleus is an extremely challenging approach

that could provide a description of very light nuclear systems (i.e hydrogen and helium isotopes), using tools coming from effective field theory or models describing nucleon-nucleon interactions.

The nuclear many-body problem can be described as:

$$H\left|\Psi\right\rangle = (T+V)\left|\Psi\right\rangle = E\left|\Psi\right\rangle \tag{2.1}$$

where H the Hamiltonian of the system, is the sum of the kinetic T and the potential V energy operators. This can be written as:

$$V = \sum_{i<j} v_{ij} + \sum_{i<j<k} v_{ijk} + \sum_{i<j<k<l} v_{ijkl} + ... \tag{2.2}$$

where the individual sums represent the two body interactions v_{ij}, three body interaction v_{ijk} and so on. The particular challenge here is the description of the inter-nucleon interactions (v_{ij}, v_{ijk}, ...) in the V operator. In order to tackle this problem, a number of nuclear models have been developed with varying levels of success in describing different nuclear properties.

2.1.1 The Nuclear Shell Model

One of cornerstone of science is the observation of emerging patterns. Such patterns were noticed at the end of 1940s by the measurement of precise experimental nuclear observables for isotopes around the valley of stability. This led to the emergence of the concept of "magic numbers" and the development of the nuclear shell model by M. Goeppert Mayer [1]. By magic numbers we are referring to configuration of protons and neutrons that lead to nuclear systems with enhanced stability, like tightly bound valence nucleons or high excitation energies. Such evidence of magicity appear close to stability for numbers 2, 8, 20, 28, 50, 82, and 126. Haxel, Suess, Jensen and Mayer independently showed that by taking into account the spin-orbit interaction, the magic numbers, spins, and many properties of these isotopes could be explained. Beginning with the harmonic oscillator potential SHO, modifying it by an l^2 term and adding the spin-orbit $l \cdot s$ contribution leads to the emergence of the

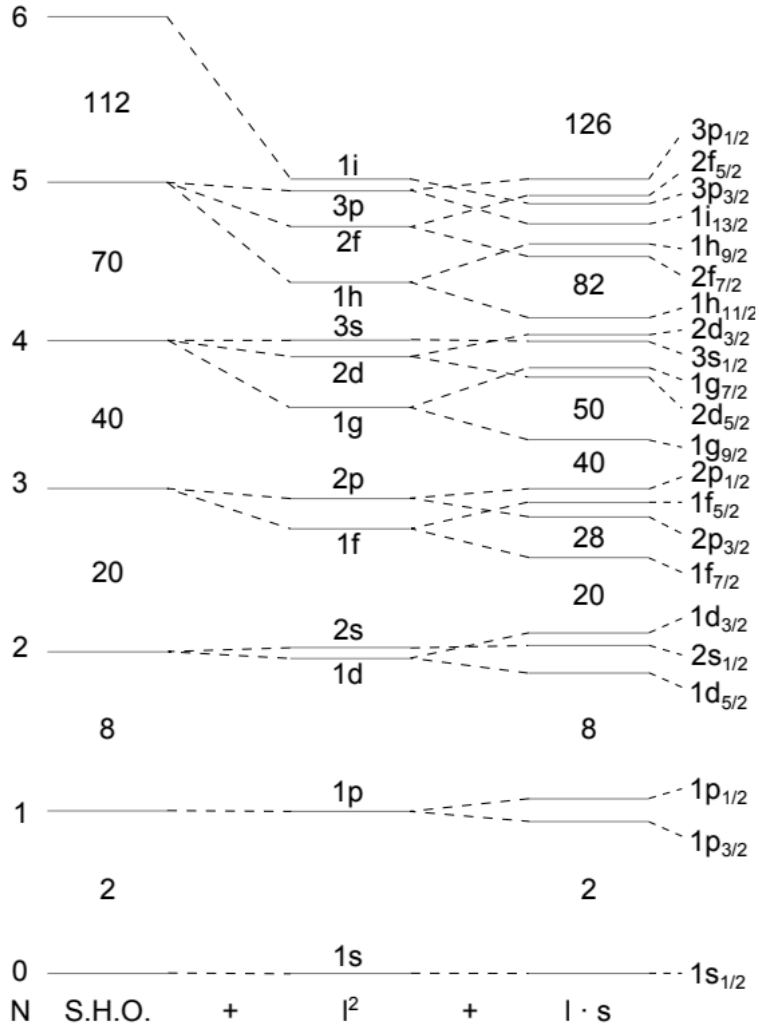

Figure 2.1: Nuclear shell model beginning with the harmonic oscillator potential SHO, modifying it by an l^2 term and adding the spin-orbit $l \cdot s$ contribution leading to the observed magic numbers.

magic numbers that are experimentally observed. Thus, the mean-field potential of the nuclear shell model can be written as:

$$U(r) = \frac{1}{2}m\omega^2 r^2 + C\,l^2 + D\,l \cdot s \tag{2.3}$$

According to the nuclear shell model, protons and neutrons gradually fill up orbitals with well-defined quantum numbers. Pairs of protons and neutrons form couples with spin 0. All the paired nucleons sitting below a magic number form an inert core where its nucleons do not contribute to the electromagnetic properties of the nucleus as their spins couple to zero. The valence space is defined by the orbits in which nucleons outside of the core are allowed to scatter. The unpaired nucleons occupy orbitals in the valence space and determine the electromagnetic properties of the nuclear system. While simple in its conception, this model works remarkably good for isotopes sitting near close to magic numbers. But more complicated models are needed to describe the experimental properties of isotopes with protons and neutrons far away from the magic numbers, models that include the interaction between the nucleons, leading to the development of the configuration interaction shell model.

In the framework of the configuration interaction shell model, and by restricting the many-body problem to two-body interactions, the nuclear Hamiltonian can be rewritten as:

$$H = \sum_{i}^{A}[T_i + U(r_i)] + \left(\sum_{i<j}^{A} V_{ij} - \sum_{i=1}^{A} U(r_i)\right) = H_0 + H_{\text{res}} \tag{2.4}$$

where $U(r)$ is the mean-field potential, H_0 the Hamiltonian of the non-interacting shell model describing a nucleon moving independently in a mean field created by all other nucleons and H_{res} describes the residuals interactions and can be considered as a perturbation in H_0.

For the calculations following this approach, firstly, a core and a valence space is chosen. The core consists of filled orbitals containing nucleons that are not interacting at all with any other nucleons. The valence space contains orbitals that nucleons are occupying and freely interact with

another. In principle, the valence space contains an infinite number of orbitals that participate in the interaction and nucleons can be excited to. But in practice, we put an upper limit to the orbitals taking part in the interaction and thus truncating the valence space and the Hamiltonian.

2.1.2 Shell model calculations

There are many different phenomenological interactions available depending on the core and the valence space in question. One of the most widely used for the region above $Z = 28$ is the JUN45 [2] interaction. The model space of the JUN45 interaction assumes a ^{56}Ni inert core and a valance space consisting of the $2p_{3/2}$, $1f_{5/2}$, $2p_{1/2}$ and $1g_{9/2}$ orbits that can yield reliable results for nuclei with $28 < Z, N < 50$.

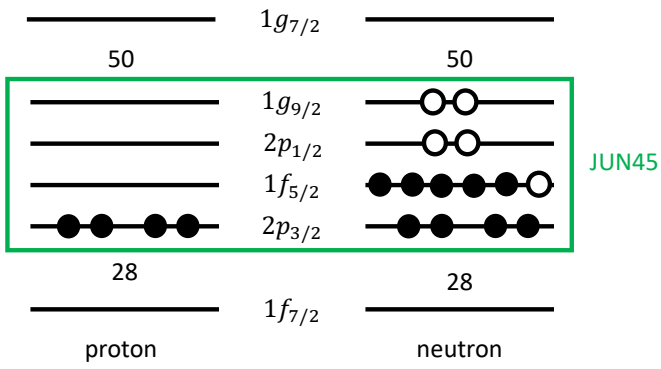

Figure 2.2: Proton and neutron orbitals around the $Z, N = 28$ and the $Z, N = 50$ major shell closures according the nuclear shell-model. The model space of the effective interaction JUN45 is also marked [3].

2.2 Nuclear properties

In order to understand the structure of the ground state (and long-lived isomeric states) of a nucleus, a variety of observables are needed, i.e. spin, electromagnetic moments, size and deformation, binding energy

and decay properties. The family of laser spectroscopy techniques offers a reliable probe and can determine the spin, electromagnetic moments, size and deformation of a nucleus, as it has been done in this thesis. These observables are described below.

2.2.1 Nuclear spin

The nucleons of a nucleus sit on different orbits that are characterised by an orbital angular momentum, while every nucleon has an intrinsic spin 1/2. The coupling of these two leads to the total angular momentum of a nucleon: $j = l \pm 1/2$. Coupling the total angular momenta of each nucleon results in the total angular momentum of the nucleus, namely the nuclear spin I.

In a nucleus with an even number of protons and neutrons, all its nucleons in the ground state are paired, leading to a nuclear spin $I = 0$. When there is only one unpaired nucleon in the valence space, the nuclear spin is solely determined by the total angular momentum of this single nucleon, provided that the isotope appears close to a semi-magic isotopic/isotonic chain and the single nucleon behaves in the context of the independent particle shell model. For isotopes with two valence nucleons, one proton and one neutron, the nucleon spins are coupling together to form a total angular momentum with values between $I = j_1 + j_2, j_1 + j_2 - 1, ..., |j_1 - j_2 - 1|, |j_1 - j_2|$.

Every nuclear spin state is also characterised by a parity, which is determined by the parity of the orbits occupied by the unpaired valence nucleons. However, parity is not an observable. It is inferred in a model-dependent way based on the calculated configuration of a nuclear state.

2.2.2 Nuclear magnetic dipole moment

The motion of the nucleons inside a nucleus gives rise to the magnetic moment of the nucleus. The magnetic moment is a sensitive probe of the orbital occupation of the valence nucleons. There are two different contributions to the magnetic moment, the orbital movement of the

charged nucleons and the intrinsic moment of all the nucleons. Thus, the magnetic moment operator can be written as:

$$\mu = \sum_{i=1}^{Z} g_l^{\pi} l_i + \sum_{i=1}^{Z} g_s^{\pi} s_i + \sum_{j=1}^{N} g_l^{\nu} l_j + \sum_{j=1}^{N} g_s^{\nu} s_j \tag{2.5}$$

where $l_{i,j}$ is the orbital angular momentum and $s_{i,j}$ the intrinsic spin operator of the ith, jth nucleon. The factors g_l and g_s are the orbital and spin gyromagnetic factors respectively, which are different for protons and neutrons: $g_l^{\pi} = 1$ and $g_l^{\nu} = 0$ since neutrons do not have a net charge, $g_s^{\pi} = +5.5856946893(16)$ and $g_s^{\nu} =$ -3.82608545(90) [4], which are the experimentally measured values for a free proton and neutron respectively. The magnetic moment is in units of nuclear magneton $\mu_N = e\hbar/2m_{\pi} = 5.0507837461(15)\ 10^{-27}$ J/T [4].

The single particle magnetic moment for a nucleon in an orbital j can then be derived as:

$$\mu(j = l + 1/2) = j g_l + \frac{g_s - g_l}{2} \tag{2.6}$$

$$\mu(j = l - 1/2) = j g_l + \frac{g_s - g_l}{2} \frac{j}{j+1} \tag{2.7}$$

where these values are also called Schmidt values. Comparing the Schmidt values with experimental magnetic moments near shell closures, reveals a discrepancy stemming from the assumption of free nucleon spin gyromagnetic factors. For that reason, the effective gyromagnetic factors are used to improve the agreement, assuming values that depend on the region of the nuclear chart. For the $Z > 28$ region, common values are $g_{s,\text{eff}}^{\pi} = 0.7\ g_{s,\text{free}}^{\pi}$ and $g_{s,\text{eff}}^{\nu} = 0.7\ g_{s,\text{free}}^{\nu}$ [5, 6]. The magnetic moment resulting from the coupling of a proton and neutron can be shown to be:

$$\mu = \frac{I}{2}\left[\frac{\mu_{\pi}}{I_{\pi}} + \frac{\mu_{\nu}}{I_{\nu}} + \left(\frac{\mu_{\pi}}{I_{\pi}} - \frac{\mu_{\nu}}{I_{\nu}}\right)\frac{I_{\pi}(I_{\pi}+1) - I_{\nu}(I_{\nu}+1)}{I(I+1)}\right] \tag{2.8}$$

where μ_{π} the proton and μ_{ν} the neutron magnetic moments. Finally, the magnetic moment can be written as:

$$\mu = \frac{gI}{\mu_N} \tag{2.9}$$

where g is the g-factor, I the nuclear spin and μ_N the nuclear magneton.

2.2.3 Nuclear quadrupole moment

The distribution of the protons and neutrons inside a nucleus give rise to the quadrupole moment of the nucleus. The quadrupole moment is a probe of the deformation of a nucleus. The quadrupole moment operator is:

$$Q_z = \sum_i \frac{e_i}{e}(3z_i^2 - r_i^2) \tag{2.10}$$

where $r^2 = x^2 + y^2 + z^2$ and e_i the charge of a nucleon. Expressing the quadrupole moment in spherical coordinates as a rank 2 tensor:

$$Q_2^0 = \sqrt{\frac{16\pi}{2}} \sum_i \frac{e_i}{e} r_i^2 Y_2^0(\theta_i, \phi_i) \tag{2.11}$$

The expectation value of the Q_2^0 in the nuclear state $M = I$ is the spectroscopic quadrupole moment Q_s:

$$Q_\mathrm{s} = \begin{pmatrix} I & 2 & I \\ -I & 0 & I \end{pmatrix} \langle I||Q_2^0||I\rangle \tag{2.12}$$

For $I \leq 1/2$, $Q_\mathrm{s} = 0$ since the value of the $3j$ symbol is 0 for these I. Same as with the nuclear magnetic moments, the introduction of effective charges is necessary to improve the agreement with the experimental values. For the $Z > 28$ region, common values are $e_\pi^\mathrm{eff} = 1.5\ e_\pi^\mathrm{free}$ and $e_\nu^\mathrm{eff} = 1.1\ e_\nu^\mathrm{free}$, in the $2p_{3/2}, 1f_{5/2}, 2p_{3/2}, 1g_{9/2}$ valence space.

In a system with one nucleon outside a closed shell, the quadrupole moment will be determined by the quadrupole moment of the single particle:

$$Q_{\text{s.p.}} = -\frac{e_n}{e}\frac{2j-1}{2j+2}\langle r^2\rangle_{\text{s.p.}} \tag{2.13}$$

where e_n is the charge of the single nucleon. When nucleons are filling a particular shell model orbital j, in a seniority-1 configuration, the quadrupole moment of odd n nucleons can be calculated via [7]

$$Q_{\text{s}} = Q_{\text{s.p.}}\frac{2j+1-2n}{2j-1} \tag{2.14}$$

Following this simple framework, it is expected that the quadrupole moments of nuclei will have a linear relation to the occupation number of a nucleon orbit and will be zero when the orbit is half-full.

2.2.4 Nuclear mean-square charge radius

The nuclear mean-square charge radius is the second radial moment of the nuclear charge distribution and can be expressed as

$$\langle r^2\rangle = \frac{\int \rho(r) r^2 dr}{\int \rho(r) dr} \tag{2.15}$$

This monopole moment of the nucleus is a probe of the size and shape of a nucleus. Laser spectroscopy can not extract the mean-square charge radius $\langle r^2\rangle$, but rather the difference of the mean-square charge radii between two different isotopes $\delta\langle r^2\rangle^{AA'}$.

Usually, the liquid drop model is used to roughly approximate the charge radius of a nucleus. Beginning with the liquid drop model though, a more general and refined model can be constructed, namely the droplet model. The power of the droplet model is focused on the finiteness of the thickness of the nuclear surface and the finiteness of the nuclear compressibility. The density distributions of neutrons and protons are no longer considered to be constant inside a sharp boundary and zero outside, as they may be in the liquid drop model. In the droplet model the densities are only approximately constant in the bulk of the system,

and instead of a sharp boundary there is a diffuse surface region in which the densities decrease smoothly to zero [8].

The first step to construct the nuclear density distribution of the droplet model is to estimate the size of the nuclear system (with neutrons and protons together), where the mean radius R can be expressed [8] as

$$R = r_0 A^{1/3} \left(1 + \overline{\varepsilon}\right) \tag{2.16}$$

where

$$\overline{\varepsilon} = \frac{-2a_2 A^{-1/3} B_s + L\overline{\delta}^2 + c_1 Z^2 A^{-4/3} B_c}{K} \tag{2.17}$$

$$\overline{\delta} = \frac{I + \frac{3}{16}\frac{c_1}{Q} Z A^{-2/3} B_v}{1 + \frac{9}{4}\frac{J}{Q} A^{-1/3} B_s} \tag{2.18}$$

$$I = \frac{N - Z}{A} \tag{2.19}$$

where B_s the ratio of the surface area of a deformed nucleus to that of a sphere with equal volume, B_c the analogous term for the Coulomb energy and B_v is associated with variations in the Coulomb potential over the surface when a nucleus is deformed [9]. Values for r_0, a_2, c_1, L, K, Q, J can be found in Refs. [10, 9, 11]. The neutron-skin thickness t can be calculated [8] as

$$t = \frac{2}{3}\frac{I - \overline{\delta}}{B_\mathrm{s}} R \tag{2.20}$$

and the effective sharp radii for the neutron R_n and proton R_z distribution can be expressed [9] as

$$R_\mathrm{n} = R + \frac{Z}{A}t \quad \text{and} \quad R_\mathrm{z} = R - \frac{N}{A}t \tag{2.21}$$

Second step is to construct a representation of shape of the density distribution [9]. Using Legendre polynomials

$$r = nR\left(1 + \alpha_2 P_2 \alpha_4 P_4 + \alpha_6 P_6 + \dots\right) \tag{2.22}$$

where n is the normalisation coefficient and equal to

$$n = 1 - \frac{1}{5}\alpha_2^2 - \frac{2}{105}\alpha_2^3 + \frac{2}{25}\alpha_2^4 - \frac{2}{35}\alpha_2^2\alpha_4 - \frac{1}{9}\alpha_4^2 \dots \tag{2.23}$$

As a result, the coefficients B_s, B_c, B_v [9] are becoming

$$B_\mathrm{s} = 1 + \frac{2}{5}\alpha_2^2 - \frac{4}{105}\alpha_2^3 - \frac{66}{175}\alpha_2^4 - \frac{4}{35}\alpha_2^2\alpha_4 + \alpha_4^2 + \dots \tag{2.24}$$

$$B_\mathrm{c} = 1 - \frac{1}{5}\alpha_2^2 - \frac{4}{105}\alpha_2^3 + \frac{51}{245}\alpha_2^4 - \frac{6}{35}\alpha_2^2\alpha_4 - \frac{5}{27}\alpha_4^2 + \dots \tag{2.25}$$

$$B_\mathrm{v} = 1 - \frac{1}{5}\alpha_2^2 - \frac{2}{105}\alpha_2^3 - \frac{253}{1225}\alpha_2^4 - \frac{4}{105}\alpha_2^2\alpha_4 + \frac{4}{9}\alpha_4^2 + \dots \tag{2.26}$$

The next step into refining the droplet model is the redistribution effect where the protons (and neutrons to some extent) are pushed toward the surface by the Coulomb repulsion. The redistribution creates a central depression in the proton distribution that increases all the radial moments. It also increases the charge on the ends of a deformed shape, resulting in an increase in the quadrupole and other even-order multipole moments [9].

The last step is to add the diffuseness effect in the droplet model that is integrated using convolution methods. When a normalised, spherically symmetric, short-ranged function is folded into a sharp-surfaced distribution the resulting diffuse distribution still has the same volume integral (contains the same number of particles). The most significant is that the multipole moments of the distribution remain unchanged [9].

Thus, the charge radius of a nucleus according the droplet model can be expressed [9] as

$$\langle r^2 \rangle_\mathrm{droplet} = \langle r^2 \rangle_\mathrm{u} + \langle r^2 \rangle_\mathrm{r} + \langle r^2 \rangle_\mathrm{d} \tag{2.27}$$

where $\langle r^2 \rangle_u$ is the contribution from the size and shape of the uniform nuclear distribution

$$\langle r^2 \rangle_{\mathrm{u}} = \frac{3}{5} R^2 \left(1 + \alpha_2^2 + \frac{10}{21}\alpha_2^3 - \frac{27}{35}\alpha_2^4 + \frac{10}{7}\alpha_2^2\alpha_4 + \frac{5}{9}\alpha_4^2 + \dots \right) \quad (2.28)$$

the term $\langle r^2 \rangle_r$ is the contribution from the redistribution and its effect on the shape

$$\langle r^2 \rangle_{\mathrm{r}} = \frac{12}{175} C' R^2 \left(1 + \frac{14}{5}\alpha_2^2 + \frac{28}{15}\alpha_2^3 - \frac{29}{5}\alpha_2^4 + \frac{116}{15}\alpha_2^2\alpha_4 + \frac{70}{26}\alpha_4^2 + \dots \right) \quad (2.29)$$

and the term $\langle r^2 \rangle_d$ is the contribution from the diffuseness

$$\langle r^2 \rangle_{\mathrm{d}} = 3\sigma^2 \quad (2.30)$$

where

$$C' = \frac{1}{2} \left(\frac{9}{2K} + \frac{1}{4J} \right) \frac{Ze^2}{R_{\mathrm{z}}} \approx 0.0156 Z A^{-1/3} \quad (2.31)$$

and values for σ can be found in Refs. [10, 9, 11].

The trends of the experimental values of the charge radii in a long isotopic chain can reveal information on the changing nuclear structure (occupation of different single particle levels or collective correlations) in the region. A sudden slope change in the trend indicates the crossing of the shell closure, something that is observed across all the magic numbers of the nuclear chart [12]. A sudden slope change can also denote sudden structural changes and evolution of deformation.

Another effect that is present across the whole nuclear chart is the odd-even staggering (OES) effect. This is related to the fact that the radius of the odd-N isotope is normally smaller than the average of the two neighbouring even-N isotopes [13]. The source of the increased radius

of the even-N nuclei is the pair scattering effect [14] which is blocked in the case of odd-N nuclei [15]. Naturally, there is exceptions to that, something that is referred to as inverted OES, present in various regions of the nuclear chart including the nickel region ($Z > 28$). The inverted OES effects is an indication of collectivity effects and deformation as it will be discussed in Ch. 3.In order to study the OES effect better, the staggering parameters D is defined as:

$$D = \langle r^2 \rangle^N - \frac{1}{2}\left(\langle r^2 \rangle^{N-1} + \langle r^2 \rangle^{N+1}\right) \tag{2.32}$$

2.3 The Hyperfine Interaction

The finite size and the inner structure of the nucleus, via its electromagnetic moments, interact with the electromagnetic fields generated by the movement of electrons, leading to what is known as hyperfine structure (hfs) in the atomic electron energies. This interaction is causing the splitting of the fine structure energy states, by coupling the nuclear spin I with the atomic (electron induced) spin J to the total angular momentum F giving rise to the hyperfine levels, ranging between $|I - J| \leq F \leq |I + J|$. By performing a multipole expansion to this electromagnetic interaction between nucleus and electrons, the contribution from the different nuclear electromagnetic moments can be observed [16] as

$$H = H_{E0} + H_{M1} + H_{E2} + ... \tag{2.33}$$

where H_{E0} is the electric monopole contribution, H_{M1} the magnetic dipole contribution, H_{E2} the electric quadrupole contribution and so on.

2.3.1 Magnetic dipole hyperfine constant A

The interaction between the magnetic dipole moment of the nucleus and the magnetic field created by the electrons over the nuclear volume can be described as

$$H_{M1} = -\boldsymbol{\mu} \cdot \boldsymbol{B_0} = -\frac{\mu B_0}{\hbar^2 IJ} \boldsymbol{I} \cdot \boldsymbol{J} \tag{2.34}$$

with the energy of a hyperfine state with quantum numbers (F, J, I), relative to the energy of the J-state, given by:

$$\Delta E_{M1} = -\frac{1}{2}\frac{\mu B_0}{IJ}\left(F(F+1) - I(I+1) - J(J+1)\right) = -\frac{1}{2}\frac{\mu B_0}{IJ} K \tag{2.35}$$

where K is

$$K = F(F+1) - I(I+1) - J(J+1) \tag{2.36}$$

We can define the A hyperfine constant, describing the strength of the interaction between the magnetic moment of the nucleus μ and the magnetic field created by the electrons at the position of the nucleus B_0, as

$$A = \frac{\mu B_0}{IJ} \tag{2.37}$$

In case of $I = 0$ (no magnetic moment) or $J = 0$ (no magnetic field induced by electrons), the interaction Hamiltonian is zero and thus, there will be no magnetic dipole interaction and $A = 0$.

2.3.2 Electric quadrupole hyperfine constant B

It originates from the interaction between the electric quardupole moment of the nucleus and the electric field gradient of the electronic cloud surrounding the nucleus. This interaction results into an energy shift relative to the energy of the J-state as a function of F that can be described as

$$\Delta E_{E2} = eQ_{\mathrm{s}}V_{\mathrm{zz}} \frac{\frac{3}{4}K(K+1) - I(I+1)J(J+1)}{2I(2I-1)J(2J-1)} \tag{2.38}$$

The B hyperfine constant describes the interaction between the spectroscopic electric quadrupole moment of the nucleus Q_s with the electric field gradient created by the electrons at the position of the nucleus V_{zz}, as

$$B = eQ_{\mathrm{s}}V_{\mathrm{zz}} \tag{2.39}$$

In case of $J < 1$, then $V_{\mathrm{zz}} = 0$ and in case of $I < 1$, then $Q_{\mathrm{s}} = 0$. In both cases, there will be no quadrupole interaction and as a result $B = 0$.

2.3.3 Isotope shift

When comparing the difference in the fine energy levels between two different isotopes, one can observe what is known as the isotope shift (IS). This effect originates from the monopole part of the electromagnetic interaction Hamiltonian.

$$\delta\nu^{AA'} = \nu^{A'} - \nu^{A} \tag{2.40}$$

The IS has two different components, namely the mass shift $\delta\nu_{MS}$ and the field shift $\delta\nu_{FS}$ and thus can be expressed as

$$\delta\nu^{AA'} = \delta\nu_{\mathrm{MS}} + \delta\nu_{\mathrm{FS}} \tag{2.41}$$

The mass shift is depending on the transition frequency and the mass of the nucleus in question, while the field shift depends on the electronic configuration of the states of the atomic transition and the change in the nuclear mean square charge radius of the two considered isotopes. The mass shift is dominating the isotope shift in the light nuclei, while the field shift dominates in the heavy.

The Mass Shift

The mass shift arises from the motion of the nucleus and the electronic cloud around their common center-of-mass. Two isotopes differ in the

number of neutrons, which translates in a difference in their mass and subsequently in a different reduced mass for the whole atomic system. This is known as the normal mass shift $\delta\nu_{\mathrm{NMS}}$.

At the same time, this mass difference between the isotopes invokes differences in the correlations between electrons, an effect known as the specific mass shift $\delta\nu_{\mathrm{SMS}}$.

Concluding, the mass shift can be expressed as

$$\delta\nu_{\mathrm{MS}} = \delta\nu_{\mathrm{NMS}} + \delta\nu_{\mathrm{SMS}}$$

$$M_{\mathrm{NMS}}\frac{m_{A'} - m_A}{m_{A'}m_A} + M_{\mathrm{SMS}}\frac{m_{A'} - m_A}{m_{A'}m_A} = M\frac{m_{A'} - m_A}{m_{A'}m_A} \tag{2.42}$$

where M_{NMS}, M_{SMS} and M are the normal, specific and total mass shift constants, respectively. The normal mass shift M_{NMS} is calculated $M_{\mathrm{NMS}} = m_e\nu_0$ where m_e is the electron mass and ν_0 is the transition frequency. The specific mass shift is rather hard to be calculated theoretically.

The Field Shift

The field shift arises from the fact that nuclei are not point particles and have an extended charge distribution. This charge distribution interacts with the electric field induced by the electron cloud at the position of the nucleus.

$$\delta\nu_{\mathrm{FS}} = F\left(\delta\langle r^2\rangle + \frac{C_2}{C_1}\delta\langle r^4\rangle + ...\right) \simeq F\delta\langle r^2\rangle^{AA'} \tag{2.43}$$

where the C_i are expansion parameters (Seltzer coefficients) determined by theory [17] and F is the field shift constant. We often omit higher order corrections and simply keep the first term. The field shift can nowadays be rather well calculated using state-of-the-art atomic theory calculations [18, 19].

2.4 Probing nuclear structure with atomic physics

Collinear laser spectroscopy (CLS) is a technique using atomic physics phenomena in order to extract nuclear observables. By irradiating an atom with laser light, the hyperfine structure can be probed, from which the nuclear moments can be extracted in a nuclear-model-independent way.

2.4.1 Extracting nuclear electromagnetic moments

As we have seen in eq. 2.37, in order to extract the magnetic dipole moment from the A hfs constant, we would need knowledge of the B_0 value. But with the use of a reference isotope with a known magnetic moment measured through another method from literature, one could extract the magnetic moment μ, easily, as:

$$\mu = \frac{A\,I}{A_{\text{ref}}\,I_{\text{ref}}}\mu_{\text{ref}} \tag{2.44}$$

Note here that eq. 2.44 is based on the assumption that the ratio of the A hfs parameter of the two involved fine levels is constant for the whole isotopic chain. Unfortunately, this is only an approximation and in case of the presence of hyperfine anomaly, a change in the number of neutrons can lead to differences in the value of the A ratio across the isotopic chain. There are two mechanisms that give rise to hyperfine anomaly; the Breit-Rosenthal-Crawford-Schawlow effect that stems from difference in the extended nuclear charge distribution [20] and the Bohr-Weisskopf effect that stems from the extended distribution of the magnetisation over the nuclear volume [21]. In the context of this thesis, the presence of the hyperfine anomaly effects is expected to be below our observation limit and thus, the effect is neglected [22].

In order to extract the spectroscopic electric quadrupole moment from eq. 2.39, one needs to evaluate the V_{zz} atomic parameter. But with the use of a literature value from a reference (typically a stable) isotope, we could extract the quadrupole moment Q_{ref} as:

$$Q_{\rm s} = \frac{B}{B_{\rm ref}} Q_{\rm s,\ ref} \tag{2.45}$$

2.4.2 Extracting changes in charge radii

In order to extract the changes in the mean square charge radii from the isotope shifts, a careful evaluation of the field shift F and the mass shift M parameters is necessary. As we have seen already in sec. 2.3.3, it is:

$$\delta\nu^{AA'} = F\delta\langle r^2\rangle^{AA'} + M\frac{m_{A'} - m_A}{m_{A'}\, m_A} \tag{2.46}$$

In order to avoid theoretical input for the F and M atomic parameters, we can apply what is known as a King plot analysis, where we use measured charge radii for stable isotopes (using another experimental method, e.g. elastic electron scattering, muonic atom spectroscopy, optical spectroscopy), to calibrate F and M. Working on eq. 2.46, we can get:

$$\begin{aligned} \mu^{AA'}\delta\nu^{AA'} &= F\mu^{AA'}\delta\langle r^2\rangle^{AA'} + M \\ \delta\nu^{AA'}_{\rm mod} &= F\delta\langle r^2\rangle^{AA'}_{\rm mod} + M \end{aligned} \tag{2.47}$$

where $\mu^{AA'}$ is the reduced mass

$$\mu^{AA'} = \left(\frac{m_{A'} - m_A}{m_{A'}\, m_A}\right)^{-1} \tag{2.48}$$

One can observe in eq. 2.47, the linear relation between the modified isotope shift $\delta\nu^{AA'}_{\rm mod}$ and the modified changes in mean square charge radii $\delta\langle r^2\rangle^{AA'}_{\rm mod}$ (modified by the reduced mass). Thus, using the measured isotope shifts for a set of isotopes with charge radii known from literature [23], one can extract the field and mass shift from the seemingly easy task of fitting a straight line to the data.

In the context of this thesis, we use the nuclear radius parameter $\Lambda_{\mu e}$ that is defined as:

$$\Lambda_{\mu e} = \delta\langle r^2\rangle_{\mu e} + \frac{C_2}{C_1}\delta\langle r^4\rangle_{\mu e} + ... \simeq \delta\langle r^2\rangle_{\mu e} \simeq \delta\langle r^2\rangle \tag{2.49}$$

The nuclear radius parameter $\Lambda_{\mu e}$ is calculated from combined analysis of the elastic electron scattering and muonic atom spectroscopy data and in a first approximation is equal to differences in the mean square charge radii $\delta\langle r^2\rangle$ [23]. As mentioned earlier in Sec. 2.3.3, C_i are expansion parameters, called Seltzer coefficients, determined by theory, found in Ref. [17].

Chapter 3

Motivation

As it was introduced in Ch. 2, the nuclear shell model was a great innovation in the field, with its unprecedented predictive power of ground state properties. With the radioactive beam facilities that appeared after the 1960s, gradual access to exotic isotopes away from the valley of stability became available. This brought to light a huge variety of nuclear phenomena, not previously observed, and challenged the shell model.

The single-particle shell model is a microscopic model of independent, non-interacting particles in the orbitals of a spherically symmetric potential $U(r)$, which is generated by all the nucleons. On the other hand, in the collective models a nucleus and its properties are described as the collective motion (rotations and vibrations) of a macroscopic object [24].

In recent years, considerable efforts have been directed to the study (experimental and theoretical alike) of the shell structure of nuclei in the vicinity of the magic number $Z = 28$. The nickel isotopic chain is one of the most important in the region since it is located at a proton shell closure that arises due to the spin-orbit interaction, namely the $Z = 28$, where the $\pi f_{7/2}$ is fully filled and separated from the higher lying $\pi f_{5/2}, \pi p_{3/2}$ and $\pi p_{1/2}$ levels. At the same time, the region spans between two major neutron shell closures; beginning at the $N = 28$, the neutrons are gradually filling the negative parity $p_{3/2}$, $f_{5/2}$, $p_{1/2}$ and $g_{9/2}$ neutron orbitals, reaching the $N = 50$ shell closure. Studying the

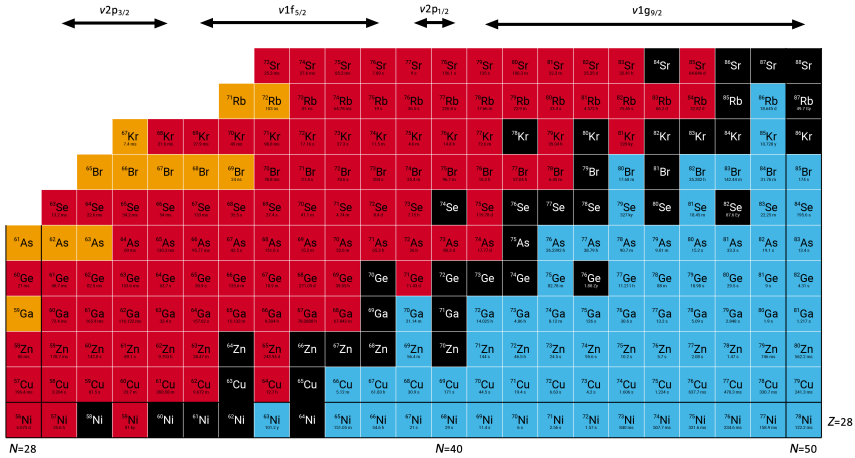

Figure 3.1: Chart of the nuclides above $Z = 28$, in the nickel region.

isotopic chain of copper ($Z = 29$), zinc ($Z = 30$) and gallium ($Z = 31$) has revealed a multitude of nuclear structure phenomena in the region.

One of the most interesting phenomena present in the nickel region is the emergence of a weak subshell effect at $N = 40$. The $N = 40$ harmonic oscillator magic number has been widely debated [25, 26]. The high excitation energy of the first 2^+ state in ^{68}Ni and its small half-life [27], as well as the low $B(E2)$ transition rate [28] are signatures of magicity. However, they are attributed to the parity change between the pf orbits below $N = 40$ and the gds above it [29]. At the same time, high-precision mass measurements have revealed a weak sub-shell effect in the nucleus of ^{68}Ni [30, 31]. Nevertheless, all these signatures seem to disappear quickly while moving away from $Z = 28$. Another excellent observable for the investigation of shell and subshell closures are the mean square charge radii. While there are sparse data for the nickel isotopic chain, the aforementioned subshell effect is also present in the charge radii of the copper isotopes [32]. This effect can also be seen on the magnetic dipole and electric quadrupole moments of the copper isotopes [33] as well as in the excitation energies and $B(E2)$ transition rates and it can again, be attributed to the parity change of the orbitals below and above $N = 40$. This indicates the persistence of the subshell effect for $Z = 29$,

despite the absence of such signatures in other observables. By adding more protons, and moving up to zinc and gallium isotopes, all signs of the $N = 40$ subshell effect disappear [31, 30]. The germanium ($Z = 32$), with 4 protons above the Z =28 shell closure, thus filling the $\pi p_{3/2}$ orbit, offers a further test ground for the evolution of this weak subshell effect (e.g. two neutron separation energies [34]), that might become visible again, due to the filled proton orbit.

The magnetic dipole moment is a sensitive probe of the single particle nature of a nuclear state and of the main component of its wave function. Additionally, the spectroscopic electric quadrupole moment is a probe of the deformation of a nuclear state. Knowledge of these moments is of key importance in understanding the configuration of protons and neutrons in any state, the shells they are occupying and their correlations. Studying the nuclear moments of the isotopic chains in the region has yielded a wealth of information about the shell evolution in the neighbourhood of nickel. The copper isotopes ($Z = 29$) with one proton outside the magic $Z = 28$ is one of the first cases addressed. For the odd-A isotopes, the experimental magnetic moment and g-factor of the ground state (g.s.) of $^{69}Cu_{40}$ are close to the effective single particle (SP) values of a $\pi p_{3/2}$ configuration indicating the magicity of $N = 40$ [33]. This magic behaviour of $N = 40$ is mostly because of the parity change that does not allow $M1$ excitations from the negative parity pf orbitals below into the positive $\nu g_{9/2}$ [33]. Moving above the $N = 40$, there is an increased discrepancy between the experimental values and the effective single particle values up to ^{75} Cu, where there is a spin inversion of the g.s. from $3/2^-$ to $5/2^-$ (between $N = 43$ and $N = 45$) [33, 35]. The spin inversion was established experimentally in a laser spectroscopy study, where the hyperfine structures of ^{73}Cu and ^{75}Cu revealed directly the spins of these isotopes [35]. From $N = 40$ onwards, excitations from the $\pi f_{7/2}$ to the $\pi f_{5/2}$ are becoming increasingly important because of the attractive tensor force between neutrons filling the $\nu g_{9/2}$ and protons in the $\pi f_{5/2}$, which leads to a decreasing energy gap between the two f-orbitals [33]. For ^{75}Cu the dominant wave function component comes from a single proton in the $\pi f_{5/2}$ [35] as suggested by the measured moments. The quadrupole moments around $N = 40$ reveal a core-polarisation effect with the addition or removal of neutrons as indicated by their increasingly negative values while moving away from $N = 40$

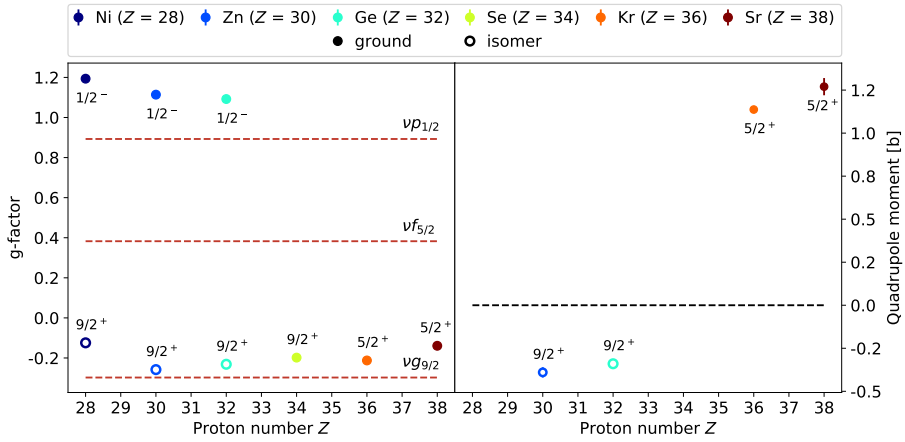

Figure 3.2: g-factor and quadrupole moments for the isotones of $N = 39$ of the even-Z isotopic chain in the region of nickel [36].

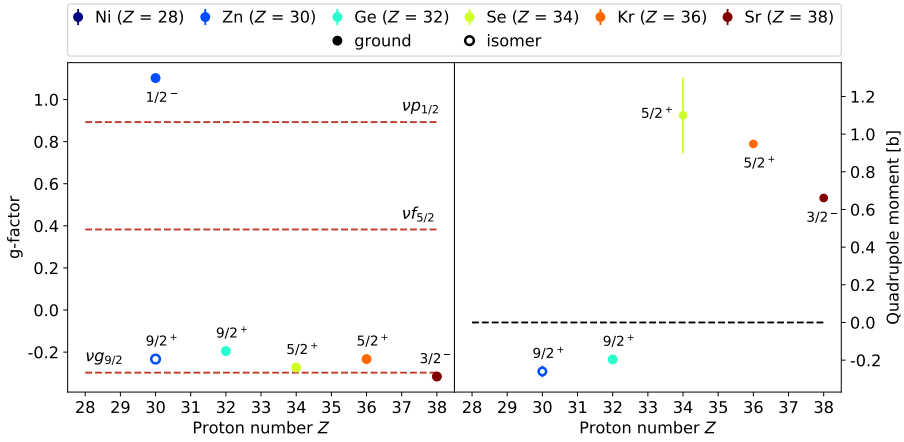

Figure 3.3: g-factor and quadrupole moments for the isotones of $N = 41$ of the even-Z isotopic chain in the region of nickel [36].

[33].

The zinc isotopic chain ($Z = 30$) is located one proton heavier. When filling the $\nu g_{9/2}$, from $N = 41$ onwards, the g.s. spin is expected to be $9/2^+$, but this is true only for $^{79}_{49}$Zn and not for ^{71,73,75,77}Zn. The

g-factors and spins of the long-lived high-spin states in $^{69-79}$Zn could be measured through high-resolution laser spectroscopy [37], revealing respectively, $9/2^+$, $9/2^+$, $5/2^+$, $7/2^+$, $7/2^+$, $9/2^+$. The g-factors are found to be all consistent with that of an unpaired neutron in the $\nu g_{9/2}$ orbital. This suggests that for the isomers in ^{69,71}Zn and ground state of ^{79}Zn, with $I = 9/2^+$, the leading term in their wave function is coming from a single unpaired neutron in the $\nu g_{9/2}$ configuration. Also, for the ^{75,77}Zn g.s., with $I = 7/2^+$, their magnetic and quadrupole moment are in agreement with a seniority-3 $\nu(g_{9/2})^3_{7/2}$ configuration [37]. Finally, the $5/2^+$ isomeric state of ^{73}Zn has a g-factor agreeing with unpaired neutrons in the $\nu g_{9/2}$ orbital but its large quadrupole moment does not coincide with the seniority-3 $5/2^+$ prediction [37, 38]. To reproduce the large quadrupole moment, large-scale shell model calculations, had to include the excitation of protons and neutrons across $Z = 28$ and $N = 50$ respectively. A T-plot analysis revealed a triaxial shape for the isomeric state [38]. A T-plot is a graphical representation of the potential energy surface of a nucleus as a function of deformation parameters (β_2 and γ). On top of it, the MCSM (Monte Carlo shell model) basis vectors are plotted as a function of deformation parameters and as circles of varying size where the size is representing the contribution of this particular eigenstate [39].

These spin inversion and collectivity phenomena can also be observed in the gallium nuclei ($Z = 31$), where the ground state of the odd-Z even-N gallium is dominated by the orbital occupied by the unpaired proton. The g-factor of ^{71}Ga ($N = 40$) is closest to the effective single particle moment indicating an odd-proton in the $\pi p_{3/2}$ as the leading configuration in the g.s. For ^{67,69}Ga and ^{75,77}Ga, with $I^\pi = 3/2^+$, their deviation from the $\pi f_{5/2}$ effective SP value indicates a more mixed configuration. Their opposite sign of quadrupole moment suggests a different structure for the isotopes below and above $N = 40$, which can be explained due to the gradual emptying of the $p_{3/2}$ orbital. The $\pi(p_{3/2})^3$ configuration has a positive quadrupole moment but the $\pi(p_{3/2})^1$ configuration has a negative value. Thus, the negative quadrupole moment of ^{75,77}Ga suggests that their g.s. wave function is dominated by a $\pi(p^1_{3/2}f^2_{5/2})$ configuration. Finally, ^{73}Ga has a g.s. spin $I = 1/2^-$ of a collective nature, with the g-factor experimental value being away from any effective SP value [40, 41].

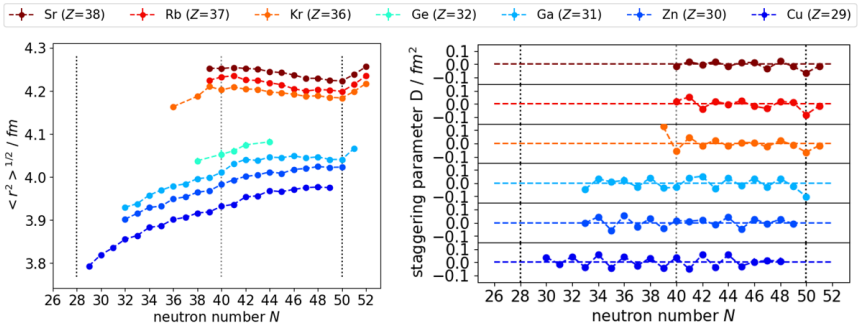

Figure 3.4: Literature mean square charge radii in the region of nickel (left) and staggering parameters for the same isotopic chains (right). The staggering parameter D is defined in Eq. 2.32.

All these phenomena revealed by the nuclear moments of the nuclei in the region, i.e. g.s. spin inversion, mixed configurations and onset of collectivity, set this region as a frontier of understanding the nature of shell evolution. In Fig. 3.2 and 3.3 we can see the g-factors and quadrupole moments of the isotones at $N = 39$ and $N = 41$ of the even-Z isotopic chains in the region. The moments of the heavier even-Z isotopes in the region, namely Se ($Z = 34$) [42, 43], Kr ($Z = 36$) [44], and Sr ($Z = 38$) [45, 46, 47], reveal similar phenomena present on the chains as well. Studying the germanium nuclear moments will help in understanding the evolution of single particle and collectivity effects around $N = 40$ as a function of Z and pave the way for further studying the nuclear structure in this region.

In most isotopic chains, the mean square charge radii display what is known as the odd-even staggering effect (OES) [13]. According to this, isotopes with an odd number of neutrons have a smaller radius compared to the average of the even neutron isotopic neighbours and details to its source are given in Ch. 2. Around the $N = 40$, the appearance of the inverted odd-even staggering effect is observed with increasing number of protons beyond $Z = 28$ (Fig. 3.4). The effect has been originally observed in the charge radii of krypton ($Z = 36$), rubidium ($Z = 37$) and strontium ($Z = 38$) isotopic chains [48, 44, 49]. The same effect has been recently observed in the charge radii of the lighter zinc [50], and more

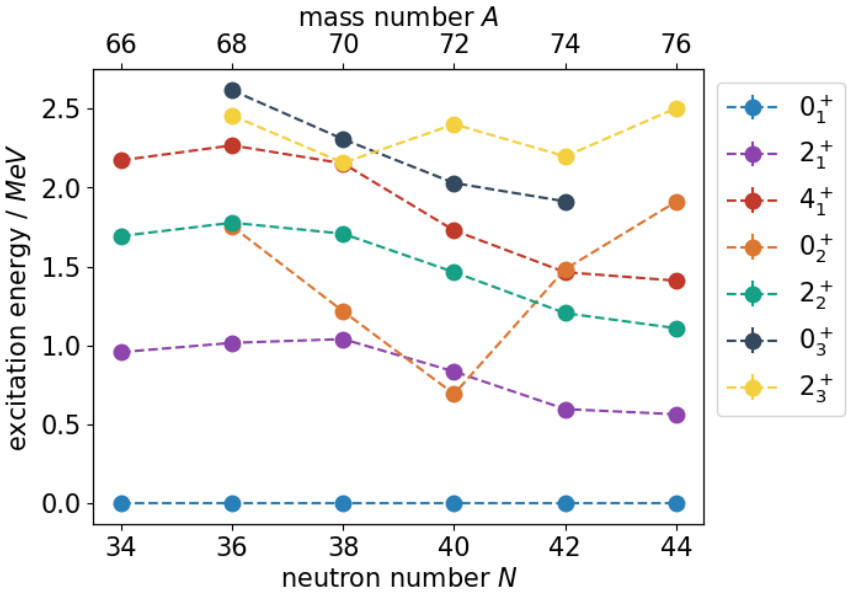

Figure 3.5: Excitation energy of the low-lying states of the even-even germanium isotopes ($Z = 32$).

strongly in gallium [51] as seen in Fig. 3.4 from the staggering parameters at $N = 40$, 41. The few mean square charge radii values available in literature for germanium isotopes give no indication for the presence of an inverted odd-even staggering effect for $Z = 32$. A systematic study of the charge radii of the germanium isotopes will provide further insight on the strength and magnitude of the effect and its evolution as a function of Z.

Finally, the understanding of the nuclear structure of germanium nuclei belong to one of the most challenging cases due to their low-lying structure and the inherent challenge of interpreting their systematics as a function of neutron number N. There is an irregular behaviour in the nuclear observables between the nuclei below and above the $N = 40$ where they exhibit a competition between different configurations associated with a variety of shapes [52]. The even-even germanium nuclei, around $N = 40$, have at least one low-lying excited 0^+ state with different properties

to that of the ground state [52], e.g. shape. The energy of the 0_2^+ level reaches a minimum at $^{72}Ge_{40}$ where it becomes the first excited state, as seen in Fig. 3.5. Such a feature is very rare in even-even nuclei and has been observed in only a few systems near or at closed shells, with most famous being the lead isotopes at ^{186}Pb [53, 54, 55, 56, 57, 58] and in the nickel isotopes at ^{68}Ni [59, 60]. There are also systems where a subshell acts like a closed shell, i.e. ^{96,98}Zr, where the Z=38 is observed as a subshell [61, 62]. All these occurrences have been explained as shape coexistence due to the presence of intruder configurations, namely configurations where excitations of at least one pair of nucleons across a shell/subshell energy gap happens [52]. The uniqueness of ^{72}Ge is the fact that it is far from any known closed shells whilst a first excited 0^+ state is present at low excitation energy. Additionally, the appearance of the highest 2_1^+ level on ^{70}Ge instead of ^{72}Ge, indicating an absence of a subshell effect at $N = 40$, poses an obstacle for collective models to describe the nature and origin of this abnormal 0_2^+ state in ^{72}Ge [63, 64]. Recent results of multi-step Coulomb excitation experiments shed some light on this problem [64, 65, 66]. In Fig. 3.6, the mean square intrinsic quadrupole moment $< Q^2 >$ is plotted for the 0_1^+ and 0_2^+ states of ^{70,72,74,76}Ge. This quantity is a measure of the deformation of a nucleus, in the same manner as the spectroscopic quadrupole moment Q_s [67]. A non-zero value is interpreted as a departure from the spherical shape for a nucleus in this state. It is evident that the 0^+ g.s. of the germanium isotopes is deformed while the 0_2^+ is becoming fast spherical when moving away from $N = 40$ and ^{72}Ge. Observing the evolution of $< Q^2 >$ with the neutron number, there is a shape transition when going from ^{70}Ge to ^{74}Ge, i.e. the ground state configuration for ^{70}Ge becomes the 0_2^+ excitation in ^{74}Ge. The recent results for ^{72}Ge indicate that this shape transition is more subtle compared to older results [52] since for ^{72}Ge the $< Q^2 >$ is almost the same for both 0_1^+ and 0_2^+ [65].

In the collective model, the β parameter is a measure of the quadrupole deformation while the γ is a measure of the axial symmetry. The energy staggering parameter

$$S(I) = \frac{[E(I) - E(I-1)] - [E(I-1) - E(I-2)]}{E(2_1^+)} \tag{3.1}$$

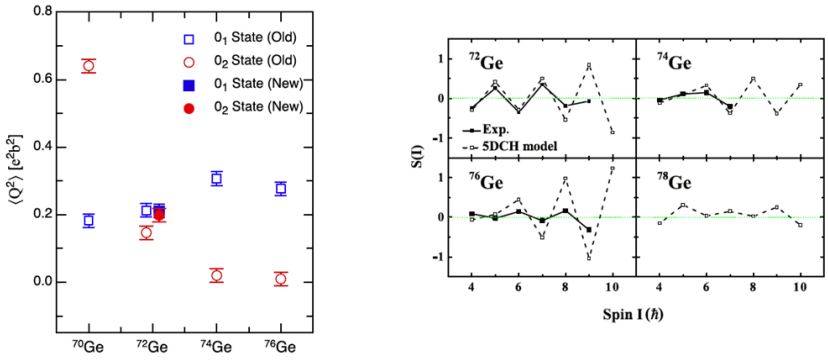

Figure 3.6: Mean square quadrupole moment $< Q^2 >$ of the 0_1^+ and 0_2^+ states of $^{70-76}$Ge [66] (left). Energy staggering parameter $S(I)$ of $^{72-78}$Ge [64] (right).

is an indicator of the behaviour of the γ parameter in the collective model [68]. An oscillating pattern with positive values for even spins and negative values for odd, with an increasing oscillating amplitude as a function of spin indicates a γ-rigid nucleus. The opposite pattern exists for a γ-soft nucleus. Especially, the sign of $S(4)$ is a strong indicator of the nature of the γ degree of freedom [69]. In Fig. 3.6, the experimental values of the energy staggering for ^{72,74,76}Ge are presented. ^{72}Ge follows that of a triaxial γ-soft potential, i.e. negative values at even spin and positive at odd spin, ^{76}Ge that of a triaxial γ-rigid shape while ^{74}Ge is somewhere in between where at low spin resembles ^{72}Ge and at higher spin ($I < 5\hbar$) that of ^{76}Ge, marking ^{74}Ge as a transition nucleus between a γ-soft to γ-rigid triaxial shape [64, 70].

All these interesting phenomena, present in the nickel region and more specifically on the germanium isotopic chain, i.e. evolution of subshell effect at $N = 40$, presence of inverted odd-even staggering effect on mean square charge radii and indications of collectivity, triaxiality and shape evolution around $N = 40$, set germanium nuclei as an intriguing case for understanding their nuclear structure. The observables yielded by laser spectroscopy, such as magnetic dipole moments, spectroscopic quadrupole moments and mean square charge radii, can prove to be a

useful addition to our effort in understanding the underlying physics in the germanium isotopes.

Finally, in Tab. 3.1, the nuclear information of the ground state and low-lying isomeric states of ^{67,69,71,73,75}Ge that are available in literature are presented.

Table 3.1: Nuclear literature data

Isotope	E_x (keV)	I^π	$t_{1/2}$	μ (μ_N)	Q_s (b)	Ref.
$^{67}Ge_{35}$	0	$1/2^-$	18.9(3) min			
	751.70(6)	$9/2^+$	146(4) ns	-0.849(18)		[71]
					0.92(9)	[72, 73]
$^{69}Ge_{37}$	0	$5/2^-$	39.05(10) h	0.733(7)	0.028(7)	[74]
	397.94(2)	$9/2^+$	2.81(5) μs	-1.001(3)		[75]
					0.75(8)	[72, 73]
$^{71}Ge_{39}$	0	$1/2^-$	11.43(3) d	+0.547(5)		[76]
	174.943(9)	$5/2^-$	79(2) ns	+1.018(10)		[77]
	198.354(14)	$9/2^+$	20.41(18) ms	-1.0413(7)		[78]
					0.34(5)	[79, 80]
$^{73}Ge_{41}$	0	$9/2^+$	stable	-0.8794677(2)		[81]
				-0.87824(5)		[82]
					-0.285(15)	[76]
					-0.18(3)	[83]
					-0.196(1)	[84]
	13.2845(15)	$5/2^+$	2.91(3) μ s	1.08(3)	0.70(8)	[73]
				-0.94(3)		[85]
					-0.4(3)	[86]
$^{75}Ge_{43}$	0	$1/2^-$	82.78(4) min	+0.510(5)		[74]

Chapter 4

Experimental Setup

The optical hyperfine structure spectra of $^{68-74}$Ge isotopes were measured by high-resolution collinear laser spectroscopy at the COLLAPS beam line, located at ISOLDE at CERN. The experiment took place in May 2018. In this chapter a brief description of the facility will be given, followed by a detailed description of the measurement technique and the developments performed for this beam time. Additionally, a study of the behaviour of the digital multimeters is presented.

4.1 The ISOLDE facility

ISOLDE (Isotope Separation Online Device) is the Radioactive Ion Beam facility of CERN, the European Organisation for Nuclear Research, located at Geneva, Switzerland. ISOLDE is one of the oldest ISOL facilities in the world, approved by the CERN council in 1964 and the first beams were delivered in 1967 [87].

The proton source consists of a hydrogen gas bottle connected with the proton ion source, located at one end of the linear accelerator LINAC 2 (replaced by LINAC 4 in 2020). The hydrogen atoms are passing through an electric field to strip off their single electron, leaving only protons to enter the LINAC 2 accelerator where they are accelerated to 50 MeV. The protons are then injected into the Proton Synchrotron Booster

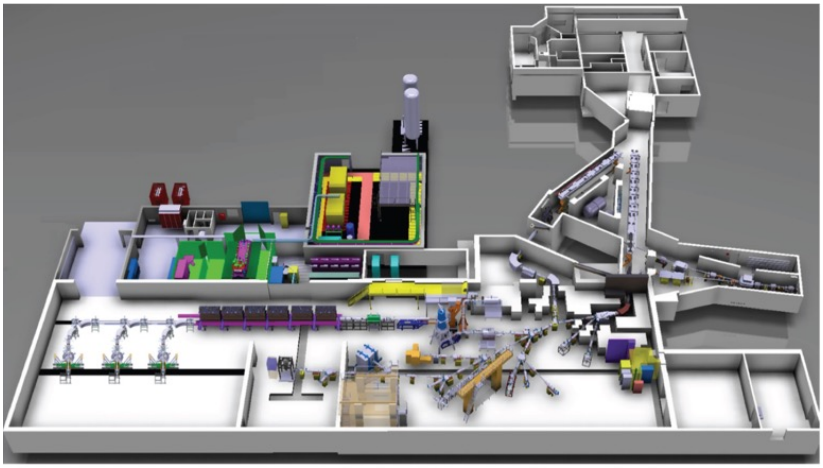

Figure 4.1: Layout of the ISOLDE facility at CERN.

(PSB), consisting of four superimposed synchrotron rings. The protons are accelerated to 1.4 GeV and released in bunches every 1.2 s with a temporal length of 2.4 μs. Each bunch contains $3{\cdot}10^{13}$ protons ($\sim$ 1 ngr) corresponding to a maximum beam current of approximately 2 μA delivered to the ISOLDE facility. The incoming protons are impinging onto the ISOLDE target and a large variety of nuclei is produced via various nuclear reactions. A graphical representation of the ISOLDE experimental hall is presented in Fig. 4.1.

In order to produce Ge isotopes with about 40 neutrons, a thick ZrO_2 target is used, heated over 2500°C. A sulphur leak was introduced to the target as well, heated to 1800° - 2200°C. The germanium atoms, are diffusing out of the target material and binding with the sulphur vapour that is flushed in the target container to form volatile GeS molecules. The volatile molecules are effusing to the heated target line and into the ionisation chamber of a hot plasma VADIS ion source. Without the use of sulphur gas to create the volatile germanium molecules, the germanium atoms would interact chemically with the various materials of the target and would thus not leave the target container. In the VADIS ion source, the radioactive molecular gas is bombarded with electrons, emitted from the cathode of the electron gun, to break the GeS molecules

apart and ionise the Ge atoms. The plasma is contained by a magnetic field, created by an electromagnet surrounding the ionisation chamber of the ion source.

The Ge^+ are then electrostatically pulled out of the target unit, accelerated to 50 keV and guided through the High-Resolution Separator (HRS). The HRS is a mass separator consisting of two electromagnets, the first with a 60° angle and the second with a 90° angle in the opposite direction, offering a mass-resolving power of about $\sim$ 1/2000 - 1/3000. After the mass separation, the radioactive ions are injected into the ISOLDE radio-frequency (RFQ) quadrupole cooler-buncher, ISCOOL [88]. This is a He gas-filled linear Paul trap that bunches and reduces the transverse emittance of the ionic beam. The electrode potentials can be remotely controlled to adjust the cooling parameters and to control the trapping and release times in the millisecond scale. The released bunches have a low energy spread ($<$ 5 eV) and a well defined time structure. The energy of the bunched beam is defined by the ISCOOL platform potential, that is approximately equal to the one on the extraction electrode of the target. The germanium ions were trapped for 5 ms and extracted in bunches of 5 μs temporal width.

4.2 Collinear Laser Spectroscopy

Collinear laser spectroscopy is a powerful technique to study the nuclear structure of ground and long lived isomer states all across the chart of the nuclides. Properties such as magnetic dipole and spectroscopic electric quadrupole moments as well as differences in the mean square charge radii between isotopes can be extracted, leading to information on the structure of such states. The technique is based on overlapping a laser beam with an atomic/ionic beam. By changing the frequency of the laser light observed by the atoms, the hyperfine transitions can be probed and resolved by using a narrow-band CW laser beam. The acquired hyperfine spectrum gives access to the nuclear structure information hidden therein. Applying this technique in an ISOL-type radioactive ion beam facility, where isotopes of different mass are easily selected by changing automatically the mass separator settings, one can perform

systematic studies of the evolution of the nuclear structure from the stable isotopes up to exotic isotopes away from the valley of stability.

In collinear laser spectroscopy, the use of an accelerated atomic/ionic beam improves significantly the resolution that can be achieved in the experiment. Because the ions are produced in a hot cavity, their energy (and thus their velocity) is Doppler broadened due to their thermal motion. This velocity spread induces a "Doppler broadening" of the spectral lines. When the ions are accelerated however, they will all be subjected to the same increase in their kinetic energy while the energy spread remains constant

$$\delta E = \delta\left(\frac{mu^2}{2}\right) = mu\delta u = const. \tag{4.1}$$

As a result, their velocity spread is decreasing with increasing velocity, such that the observed spectral line width is no longer Doppler broadened, and becomes comparable to the excited state lifetime-induced line width.

4.2.1 The COLLAPS setup

After the Ge^+ are ejected from ISCOOL, they are guided to the COLLAPS beam line. The ionic beam is sent through a charge exchange cell (CEC), filled with sodium vapour, in order to be neutralised in-flight by exchanging one electron with the alkali cloud. After the charge exchange and the reconfiguration of the atomic electrons, the ground state $4s^2 4p^2\ ^3P_1$ of Ge I was populated.

The emerging atomic Ge beam is overlapped with a co-propagating laser beam, in collinear geometry, tuned to resonantly excite the $4s^2 4p^2\ ^3P_1 - 4s^2 4p5s\ ^3P_1^o$ (269.13411 nm) transition of the Ge atom. Between the available lines (seen in Fig. 4.2), this atomic line was chosen because primarily the lower level is highly populated after the CEC process [89, 90], while additionally, it provides an adequate hfs splitting that could be reliably resolved. The $4s^2 4p^2\ ^3P_0$ of the ground state triplet was not considered as a viable option since the expected population after the CEC reconfiguration is minimal and it does not present a hfs splitting.

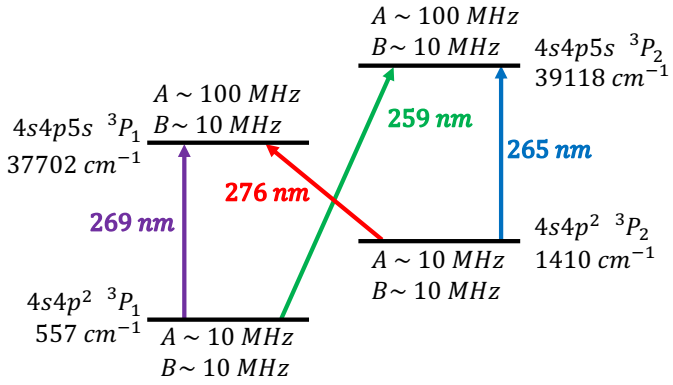

Figure 4.2: Structure of the germanium atom. The states with their expected hfs splitting are presented along with the transitions considered. The 269 nm lines was chosen as preferable.

In order to scan over the frequency space of the hyperfine structure, a varying voltage in the range of ±500 V was applied on the ionic germanium beam prior to its neutralisation, so that the resonant excitation condition for neutral germanium was achieved through Doppler tuning. At the end of the beamline, four photomultiplier tubes (PMTs) are detecting the photons from the fluorescent de-excitation of the resonantly excited atoms as a function of the acceleration/deceleration scanning voltage. One aspherical lens placed in front of every PMT focuses the photons on the entrance window of the detector. A UG11

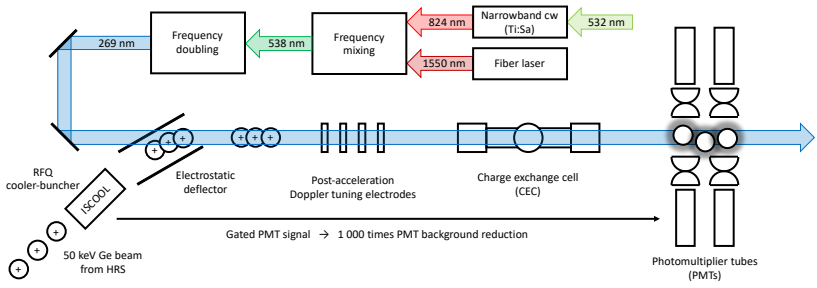

Figure 4.3: Layout of the COLLAPS beamline.

Schott Optical Filter (a bandpass filter that shows its highest transmission in the UV wavelength ranges) was placed in front of every PMT in order to suppress the scattered light, coming from the beam contaminants in the optical detection region, that in the initial tests was blinding our detectors and no signal was observed. A graphical representation of the COLLAPS beamline can be seen in Fig. 4.3.

For this experimental campaign, the new DAQ system of COLLAPS was used, namely TILDA [91]. The system consists of two FPGA cards (NI-7852R), one for data acquisition from the PMTs and one for pulse pattern generation to control the ISOLDE time gates (i.e. accumulation and release and ISOLDE beam gate), mounted on a PXI chassis. The FPGAs have a base-clock of 40 MHz, operated at 100 MHz, thus allowing for a 10 ns time resolution. The DAQ cycle is triggered by the release of the ion bunch from ISCOOL (t_0). The following information is then recorded:

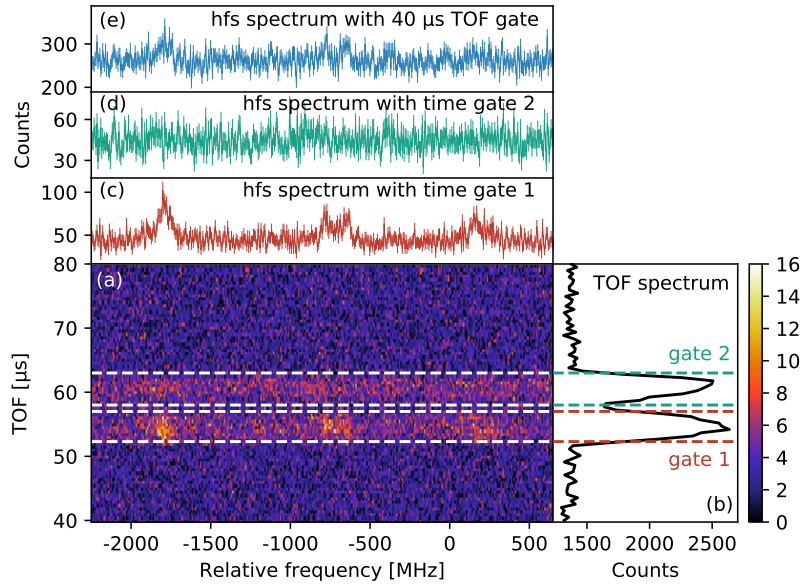

Figure 4.4: Colour-coded 2D plot with time vs frequency (voltage step) vs counts acquired for ^{73}Ge with the new DAQ system (TILDA) of COLLAPS [3].

the photon counts recorded by each PMT, the scanning voltage, and the time of flight (TOF: time difference between the release time of ion bunch from ISCOOL and arrival of ion bunch at the photo-detectors) with a 10 ns resolution. This allows the reconstruction of the data in a full 3D matrix with TOF vs scanning voltage vs photon counts. This real-time recording function is essential for the Ge experiment due to the high isobaric contamination released from ISCOOL along with the radioactive Ge ion bunch. With this DAQ, a time gate can be applied to choose only the events from the fluorescence decay of the ion bunch, allowing a significant reduction of the huge contamination-related background in the hfs spectrum. This time gate can be realised visually for both online monitoring and offline analysis.

In order to demonstrate this, a full 3D matrix acquired for ^{73}Ge during the experiment is presented in Fig. 4.4. On the TOF spectrum (Fig. 4.4(b)), one can see the existence of two components. The early component (gate 1) corresponds to the germanium atomic bunch while the late one (gate 2) probably comes from the possible molecular contamination released from the ISCOOL and yields no resonant photons (Fig. 4.4(d)). By gating on the first component of the TOF spectrum and eliminating the possible contaminants, the hfs spectrum of ^{73}Ge was reconstructed (seen in Fig. 4.4(c)), allowing the reduction of the background by almost one order of magnitude (seen by comparing Fig. 4.4(c) and (e)). The mass of the second bunch is approximately 15 u heavier and its chemical composition cannot be defined unambiguously taken into account the production and chemistry of germanium and the other elements at $A = 73$.

4.2.2 Production of the 269 nm line of Ge I

The $4s^2 4p^2\,{}^3P_1 - 4s^2 4p 5s\,{}^3P_1$ (269.13411 nm) line of the atom of germanium sits in a region of the electromagnetic spectrum that was inaccessible to the COLLAPS cw laser setup, prior the experiment. Typically, the production of the UV light of 269 nm, is obtained by frequency doubling the fundamental green light of 538 nm. In order to produce this green light with a cw laser system, a blue or UV pump laser (like an Argon-ion laser) is required which is not available anymore in the

COLLAPS laser lab and it is not under production anymore. The lack of such pump laser creates a wavelength gap in the green region, between 500-550 nm, that the commonly used Ti:Sa or Dye laser systems do not cover. The spectral coverage of the COLLAPS laser up is presented in a graphical manner in Fig. 4.5. In order to close this gap, a new frequency production scheme has been integrated in the laser lab, based on the frequency mixing technique. This development in the COLLAPS laser system was chosen as the preferable action because it offers a bridging option for producing light in the green region, which will be useful for future cases, as well. At the same time for germanium there are not any other viable options. All strong atomic transitions in germanium starting from the ground state triplet, need laser light that has a fundamental in the 500-550 nm (see Fig. 4.2) region while an ionic transition in germanium would be challenging since the known strong transitions sit in the deep UV (i.e. ∼100 nm).

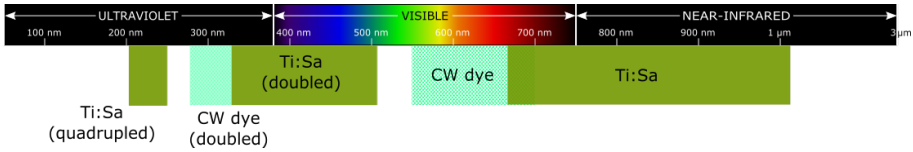

Figure 4.5: Spectral coverage by the COLLAPS CW laser systems, prior to the introduction of the frequency mixing method.

For this technique, we used the 824 nm laser light produced by a Ti:Sa[1] laser and a 1550 nm light produced by a fiber laser[2]. The two laser beams were superimposed and then single-pass through a periodically poled crystal[3], generating green laser light with the summing frequency of 538 nm ($\frac{1}{\lambda} = \frac{1}{\lambda_1} + \frac{1}{\lambda_2}$). This light was then coupled into a frequency doubling unit[4] to generate the second harmonic of 269 nm. Approximately 90 mW of laser power where ending up in the beamline.

A fraction of the output of the mixing unit was fiber coupled to a HighFinesse WSU wavelength meter used to lock the Ti:Sa cavity. The

[1]Sirah Matisse-2 Ti:Sa
[2]NKT Photonics Koheras Boostik and NKT Photonics Koheras Adjustik E15
[3]Sirah MixTrain
[4]Sirah WaveTrain

wavemeter was regularly calibrated with a stabilised diode laser (Toptica DL pro 780) locked to the $F = 2 \rightarrow F = 3$ hyperfine transition of the D1 line in ^{87}Rb [92]. The wavemeter calibration was happening after every set of isotope-reference isotope (^{72}Ge) measurement, typically every 1 hour.

4.3 Scanning the Hyperfine Structure

The energy of the atoms is defined by the sum of the different voltages applied along their path. As mentioned above, the scanning of the hyperfine structure is performed by applying a varying voltage and through Doppler tuning the frequency space is scanned. As a result, precise knowledge of the ion acceleration voltage at every moment and controlling possible voltage variations in time, is essential for extracting reliable data when converting the observed velocity to the light frequency seen by the atoms.

The total external potential applied to the ion beam at the end of the COLLAPS beam line can be expressed as

$$V_{\text{tot}} = V_{\text{ISCOOL}} - V_{\text{fluke}} - f_k V_{\text{line}} \tag{4.2}$$

where V_{ISCOOL} is the platform voltage applied on the ISCOOL cooler/buncer, V_{fluke} is a fixed offset voltage applied on every isotope in order to account for the mass shift and V_{line} is the varying scanning voltage in the range of $\pm$ 10 V. Finally, f_k is a multiplication factor (called kepco factor) that provides linear amplification to the scanning voltage, with typical values $\sim$50, that needs to be calibrated for every individual experimental run.

The voltage values of V_{ISCOOL} and V_{fluke} were recorded at the beginning and the end of every hfs measurement. For every measurement, the mean of these two was taken as the final voltage value in order to combat any voltage drifts during the measurement. V_{ISCOOL} was recorded by an Agilent 34461A Digital Multimeter, connected to a calibrated voltage divider with ratio 1:5001.39, while V_{fluke} was recorded by an Agilent 34461A Digital Multimeter and a NI PXI-4071 Digital

Multimeter (henceforth called Agilent and PXI respectively), connected to a calibrated voltage divider with ratio 1:1000.01.

In order to convert voltage to frequency, the relativistic Doppler effect has to be employed,

$$\nu = \nu_{\text{laser}}\sqrt{\frac{1-\beta}{1+\beta}}, \text{ with } \beta = \sqrt{1 - \frac{m^2c^4}{eV_{\text{tot}} + mc^2}} \tag{4.3}$$

where ν_{laser} is the laser frequency used during the experiment and m the atomic mass from AME2016 [93].

4.3.1 Calibration of the kepco factor

To determine the kepco factor (mentioned in eq. 4.2), a calibration measurement of the real voltage against the scanning voltages needs to be performed in regular intervals during the experiment. As real voltage, we define (from Eq. 4.2) the voltage that is applied on the post-acceleration electrodes (seen in Fig. 4.3)

$$V = V_{\text{fluke}} + f_k V_{\text{line}} \tag{4.4}$$

The slope of the line of these measurements is the kepco factor f_k.

In each experiment there are up to three different fluke power supplies used to be able to switch between different isotopes voltage settings fast. The kepco calibration was performed for each power supply separately and the extracted kepco factors for each individual fluke power supply was in statistical agreement with each other (seen in Fig. 4.6). As a result all measurements, irrespective of the fluke power supply, were treated as equal and the weighted mean of all the kepco scans was chosen as the final value for both the Agilent and PXI multimeters, seen in Tab. 4.1 and in Fig. 4.6.

Table 4.1: Kepco factor f_k values

	Agilent	PXI
f_k	50.4565(12)	50.4568(12)

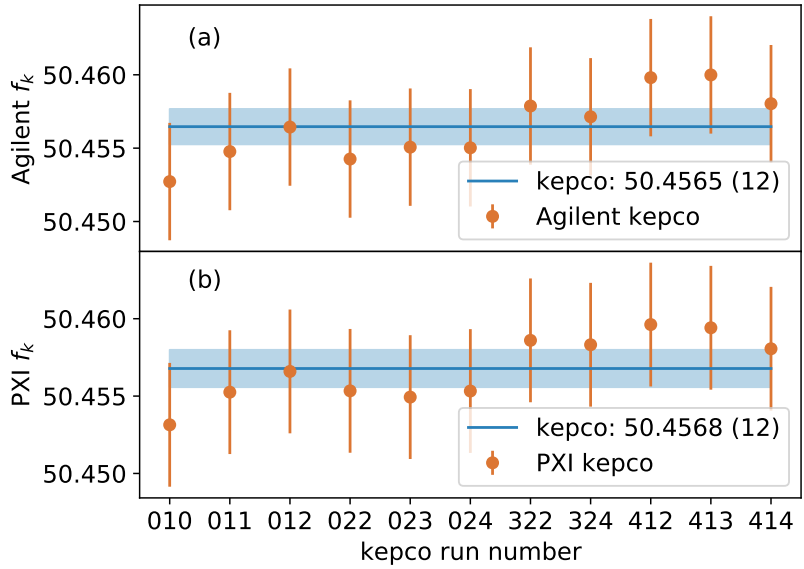

Figure 4.6: Values of all the kepco scans during the experiment and mean kepco factor f_k for (a) the Agilent and (b) the PXI multimeters.

4.4 Studying the multimeters behaviour

Based on the details mentioned above (Eq. 4.2), the importance of accurate voltage readings becomes apparent for accurate conversion to frequency space. For that reason, in this experiment the V_{fluke} was recorded at the beginning (i.e. preScan) and the end (i.e. postScan) of every hfs measurement from two different digital multimeters (the Agilent and the PXI), leading to a set of four values per hfs measurement available. This multiplet of values offers the unique chance to investigate the behaviour and performance of the two different multimeter devices.

At first, the level of discrepancy between the preScan and postScan

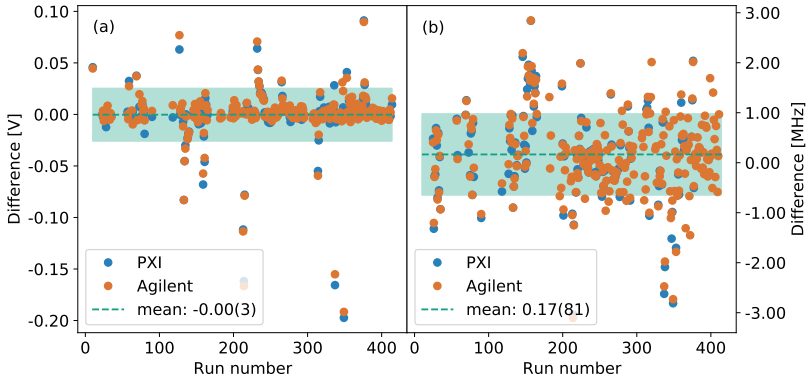

Figure 4.7: Difference between the preScan and postScan readings for every run in (a) voltage and (b) frequency space.

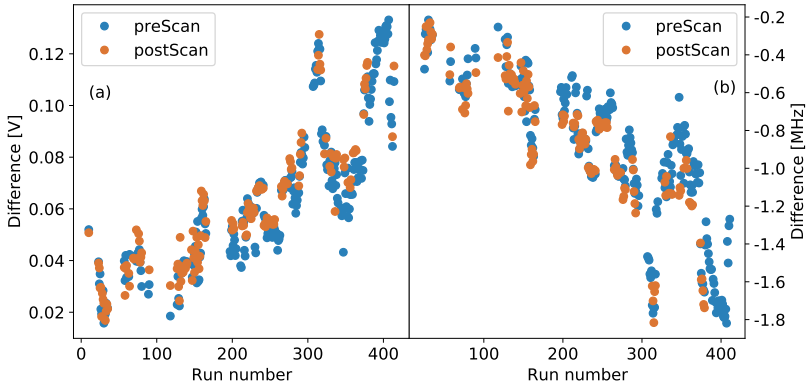

Figure 4.8: Difference between the readings of the two digital multimeters (Agilent & PXI) for every run in (a) voltage and (b) frequency space.

measurements was evaluated. As seen in Fig. 4.7(a), the average of the difference between the preScan and postScan value is $d_{\mathrm{V}} = 0.00(3)$ V which is equivalent to $d_{\mathrm{f}} = 0.0(8)$ MHz (seen in Fig. 4.7(b)) for both multimeters. This leads to the conclusion that we have a systematic uncertainty on the voltage reading of ± 0.03 V leading to a ± 0.8 MHz uncertainty.

On the other hand, we wanted to test the level of discrepancy between

the readings of the two different devices. The difference in the readings of the two multimeters reveals a slow voltage drift over the duration of the experiment, as in Fig. 4.8(a). This drift corresponds to a 1.5 MHz drift over a 5 days period (seen in Fig. 4.8(b)). Moreover, we also see some short-term fluctuations of the order of 1 MHz. This raises the question about the source of this drift and the validity of the readings from each device individually.

This led us to check the calibration of the two devices. Both Agilent devices have been calibrated by the manufacturer at the beginning of the year while the PXI multimeter needs to be auto-calibrated every couple weeks to remove any possible drifts over time. Unfortunately, the PXI has not been calibrated for a few months before the experiment. After the experiment, an auto-calibration was performed and a number of readings were taken to check if there is any change. As we can see on Fig. 4.9, before the calibration there was an offset of ~ 0.2 V between the readings of the two multimeters while after the calibration this difference is reduced to zero. Concluding, a decision was reached to omit the use of the PXI readings for the conversion of voltage to the frequency space, and only use the Agilent data.

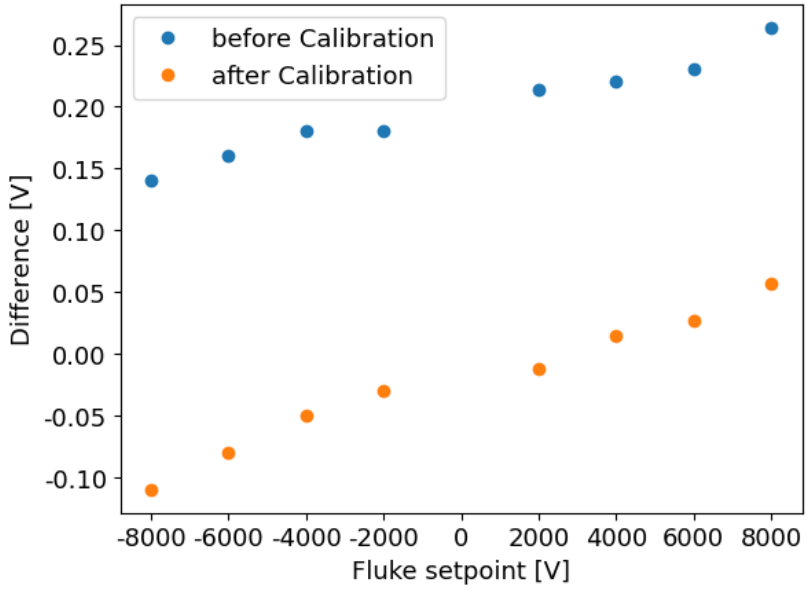

Figure 4.9: Difference in the digital multimeter readings before and after the PXI auto-calibration.

Chapter 5

Analysis & Results

In this chapter, the analysis procedure will be described in detail. Aspects of the analysis that need special care will be presented.

5.1 Hyperfine Spectra

In chapter 2 the physics behind hyperfine structure has been described while in chapter 4 it was mentioned that in any laser spectroscopy experiment, transitions between the hyperfine structure of an atomic line are being probed with the use of laser light.

In the case of the measurements in the context of this thesis, the $4s^2 4p^2\,{}^3P_1 - 4s^2 4p5s\,{}^3P_1^o$ (269.13411 nm) line of the atom of germanium has been probed. In Fig. 5.1 an example is given for the probed transitions in the hfs of an atom of ^{73}Ge in the 269 nm line (top panel) and how this is realised in a hfs spectrum (bottom panel).

It is interesting to notice that every hyperfine transition marked in Fig. 5.1 is expected to correspond to one peak in the hyperfine spectrum. However, since the experimental resolution is ($\sim$ 100 MHz), one notices less peaks: in Fig. 5.1, the leftmost two transitions marked in the hfs are appearing as a single peak in the spectrum. For that reason, before

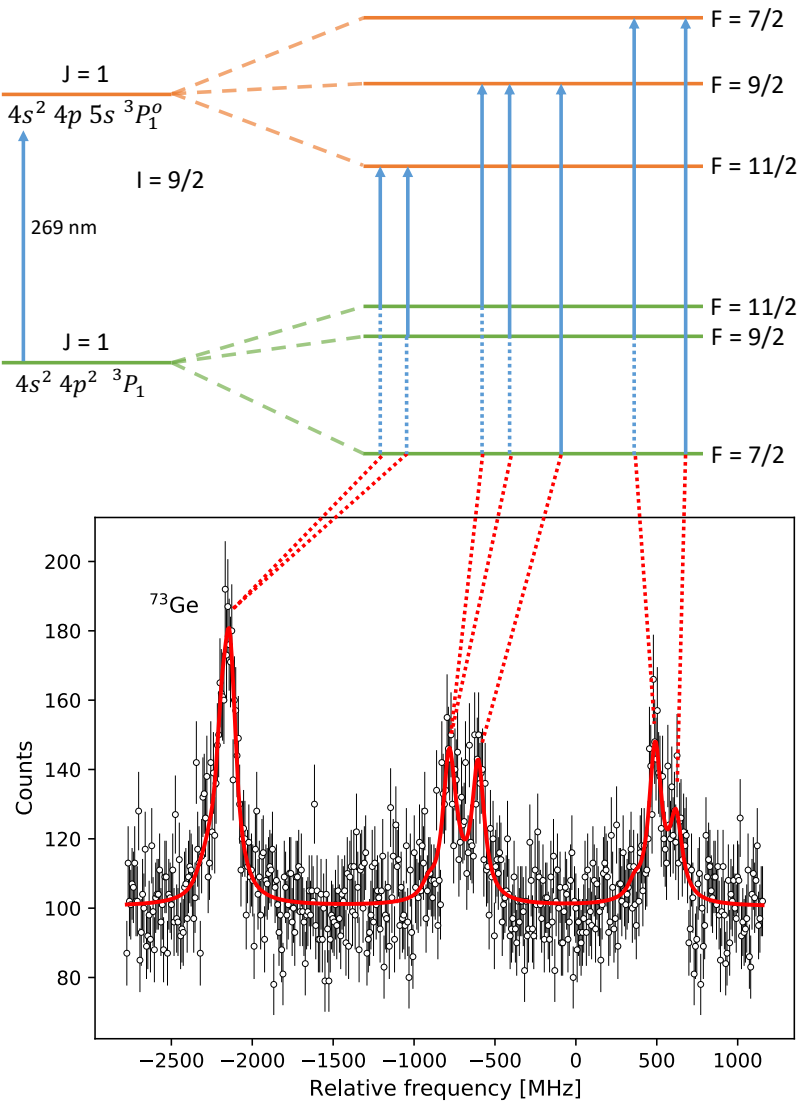

Figure 5.1: Transitions probed in the 269 nm line ($4s^2 4p^2\ ^3P_1 - 4s^2 4p 5s\ ^3P_1^o$) in the hfs of the atom of ^{73}Ge and the experimentally acquired hfs spectrum for this line. Every peak on the spectrum corresponds in a transition in the hfs.

commencing with the extraction of hfs constants, an investigation of the line shape of a single transition is needed.

5.2 Line shape investigation

There are various experimental conditions that influence the line shape of any hfs spectrum along physical phenomena that affect it as well. In this section we will discuss the line shape profile and sidepeaks investigations. By line shape profile, we refer to the mathematical function that better describes the shape of the peaks in the spectra, i.e. gaussian, lorentzian and voigt (a convolution of gaussian and lorentzian). On the other hand, by sidepeaks we refer to the appearance of small satellite peaks appearing next to the main peaks, as will be detailed further.

To facilitate the analysis procedures described below, custom Python scripts were created, using the SATLAS package [94]. SATLAS is a collection of Python libraries dedicated to the analysis of hfs spectra, providing a variety of hfs-related functions and tools such as fitting multiple spectra simultaneously, fixing the ratio of hfs constants and fixing a parameter to be fitted within a certain range (e.g. of a literature value), among others.

5.2.1 Line shape profile

The most common line shape profile describing the shape of a peak in a hfs spectrum is a voigt profile, i.e. the convolution of a lorentzian and a gaussian profile. This stems from the different physical effects that simultaneously influence the line shape of the hfs peaks. The lorentzian contribution comes from the natural line width of the line under study and other homogeneous effects like power broadening and laser line width, while the contribution from Doppler broadening is described by the gaussian profile.

In order to investigate the line shape properties and their evolution during this experiment, the spectra of the even-even isotope ^{72}Ge, which contain only one hfs peak, were fitted, with a voigt profile. In Fig. 5.2(a)

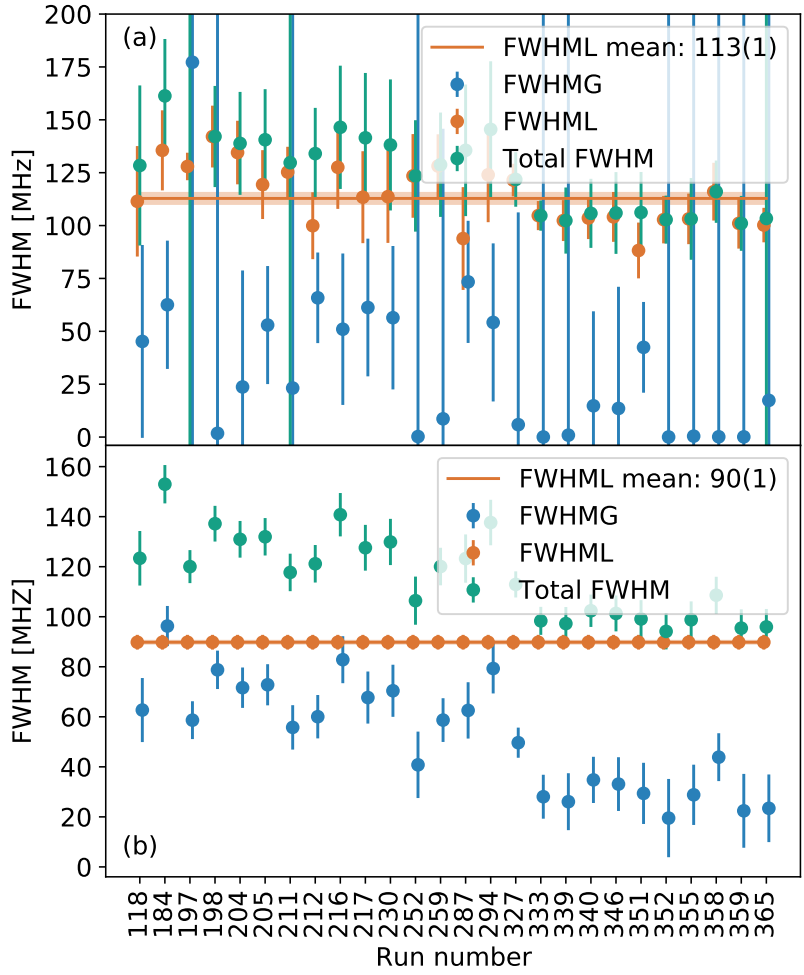

Figure 5.2: FWHM (gaussian, lorentzian and total) for all the spectra of ^{72}Ge fitted with a voigt profile and (a) with no side peaks and (b) with one side peak and a common FWHML for all spectra that were fitted simultaneously. More details in the text.

the result of this process is presented, where one can see, firstly that the gaussian FWHM (Full Width at Half Maximum) cannot be resolved (i.e. the relative uncertainty of the parameter being in the order of 500% or more) and secondly that the lorentzian FWHM is constant during the whole experiment and scatters around a mean value. This is an observation that is validated by the logbook entries as well, where the laser power during the experiment was measured regularly (beginning of every scan) at the end of the beamline, and found to be constant and around 2.5 mW. For that reason, it was decided to fit all the spectra of ^{72}Ge simultaneously and assume a voigt profile with one shared lorentzian FWHM for all the fitted spectra.

5.2.2 Side peaks

In Fig. 5.4, a spectrum of ^{72}Ge is presented, where one can notice an asymmetry on the low energy side of the single-peak (left side), hinting the existence of side peaks in the spectra that come from resonant collisional excitations in the CEC (observed in most of the previous COLLAPS experiments [95, 96]). To further investigate that, as a continuation of the above, the spectra of ^{72}Ge were fitted simultaneously. The assumed lineshape was a voigt profile with one shared lorentzian FWHM and one side peak with the same lineshape as the main peak with an offset from the main peak and poisson factor of the side-peak intensity that is the same for all fitted spectra. The side peak offset is defined as the distance between the main and the first satellite peak; every subsequent peak has the same offset from the previous one. The poison factor defines the intensity of the first side peak relative to the main; the intensity of the other sidepeaks is calculated from the Poisson-factor. The results are presented in Fig. 5.2(b), where the total, gaussian and lorentzian FWHM for each spectrum is plotted. In Fig. 5.4, a comparison between the best fit with no sidepeaks (blue) and one sidepeaks (red) is presented, where the effect of adding a side peak can be observed in the position of the centre of gravity (CoG). Such a change in the position of the main peak ($\sim$ 5 MHz) is affecting the isotope shift (IS) of each isotope, making apparent the importance of assuming a correct line shape, especially for this data set where the isotope shifts are expected to be in the order of a few dozen MHz.

Table 5.1: Side-peak parameters for different number of side peaks

N	FWHML (MHz)	Offset (MHz)	Poisson factor	Reduced χ^2
1	90(3)	-128(3)	0.095(6)	1.098
2	88(3)	-125(3)	0.100(7)	1.095
3	88(3)	-125(3)	0.100(7)	1.095
4	88(3)	-125(3)	0.100(7)	1.095
5	88(3)	-125(3)	0.100(7)	1.095

The process was repeated for up to five sidepeaks as seen in Fig. 5.3, where the offset, the poisson factor and the reduced χ^2 of each spectrum is plotted. The small change of the reduced χ^2 as well as the statistically insignificant increase of the side peak parameters (seen in Tab. 5.1) leads to the conclusion to use only one side peak in the final line shape.

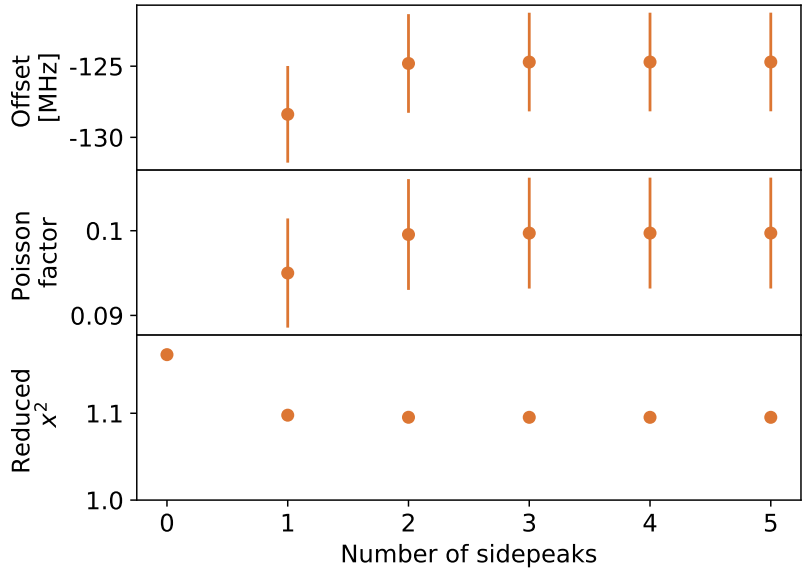

Figure 5.3: Side-peak parameters for different number of side peaks.

5.3 Fitting procedures

In this section, the individual fitting procedure for every different isotope is presented. During this experiment, hfs spectra of $^{68-74}$Ge were acquired and analysed. First, the procedure for fitting the reference isotope, ^{72}Ge, is discussed, followed by the procedures for fitting the even-Z and then the more challenging odd-Z isotopes of germanium. A list of all the files used for this analysis can be found in Appendix A.

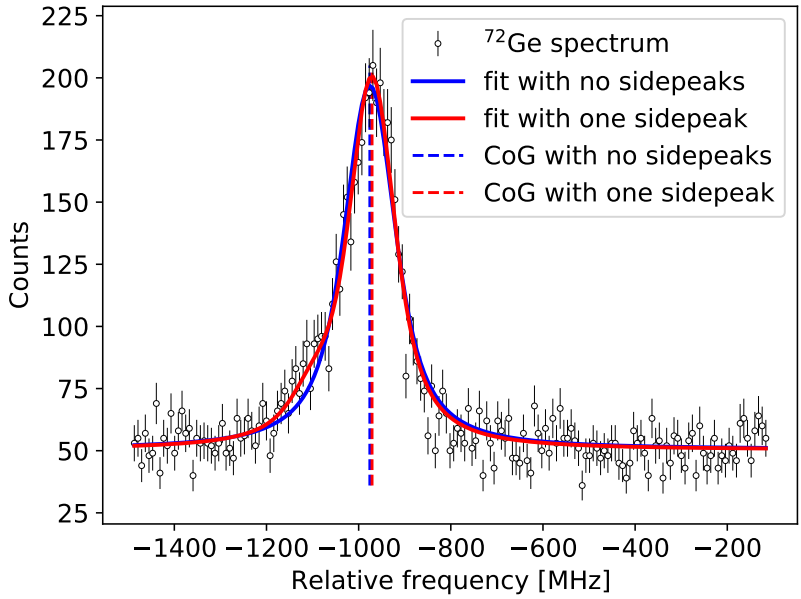

Figure 5.4: Hfs spectrum of ^{72}Ge fitted with no (blue) and one (red) side peak. The peak is fitted with a voigt profile. More details in the text.

5.3.1 Fitting the reference isotope: ^{72}Ge

The reference isotope of choice was ^{72}Ge, as it is the stable germanium isotope produced abundantly in the target. There were 26 reference hfs spectra acquired. An overview of the experimental parameters for each spectrum is given in Appendix A. All the hfs spectra of ^{72}Ge were

fitted simultaneously with a voigt profile including one side peak. The lorentzian FWHM and the side peak parameters, i.e. offset and poisson factor, were shared parameters and their fitted results are presented in Tab. 5.2, while the best fit can be seen by the red line in Fig. 5.4. The centre of gravity was an independent variable for every spectrum and was fitted separately. Results for the CoG are presented in Fig. 5.5 and in Tab. B.1 in Appendix B.

One might notice both in Figs. 5.2 and 5.5 that the files after run 300 present a more stable behaviour (i.e. less scattering of the FWHM and COG). The reason behind this, is a power trip that happened before run 327, that lead to a restart of the voltage power supplies of the high tension of ISCOOL. The big scatter of the cog values before run 300 does not affect the analysis of the individual spectra as explained in Sec. 4.3.

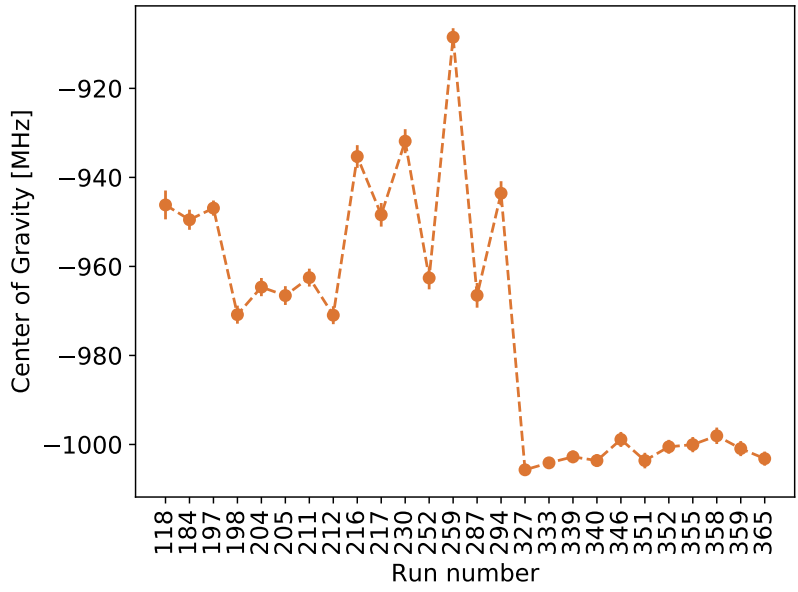

Figure 5.5: Centre of gravity (CoG) of the hfs spectra of ^{72}Ge.

Table 5.2: Results for the shared parameters of the ^{72}Ge fit.

Isotope	FWHML (MHz)	Offset (MHz)	Poisson factor
^{72}Ge	90(3)	-128(3)	0.095(6)

5.3.2 Fitting the even Z isotopes: ^{68,70,74}Ge

The line shape used for fitting the even-Z isotopes of germanium is similar to that of ^{72}Ge. The side peak offset was fixed to the value calculated using kinematics and the mass difference between each isotope and ^{72}Ge. In more detail, using the position of the side peak in the spectra of ^{72}Ge, the expected side peak position for all other isotopes can be calculated theoretically via Eq. 4.2. Note here that by fixed value, it is meant that the value was fittable within the gaussian uncertainty obtained by error propagation from the result of the reference isotope. It was also tested that the side peak offset acquired by fitting this parameter freely was in statistical agreement with the value calculated by kinematics.

The poisson factor of the side peak and the lorentzian FWHM were also fixed to the value of ^{72}Ge, after first checking the statistical agreement between the free-fitted and fixed parameters. This was chosen to combat the low statistics present in individual hfs spectra or the small number of acquired spectra per isotope.

Table 5.3: Results for the shared parameters of the ^{68,70,74}Ge fit and extracted isotope shifts.

Isotope	FWHML (MHz)	Offset (MHz)	Poisson factor	IS (MHz)
^{68}Ge	90(3)	-136(3)	0.095(6)	-46(5)
^{70}Ge	89(3)	-132(3)	0.095(6)	-32(2)
^{74}Ge	92(4)	-126(5)	0.102(10)	+51(2)

In each isotope, the three-aforementioned parameters (lorentzian FWHM,side peak offset and poisson factor) were shared in the simultaneous fit and the results are presented in Tab. 5.3 while the best fits are seen in Fig. 5.6. The extracted isotope shifts for each isotope are presented in Tab. 5.3 as well, while the centres of gravity

for each spectrum and its corresponding reference isotope spectrum are given in Appendix B.

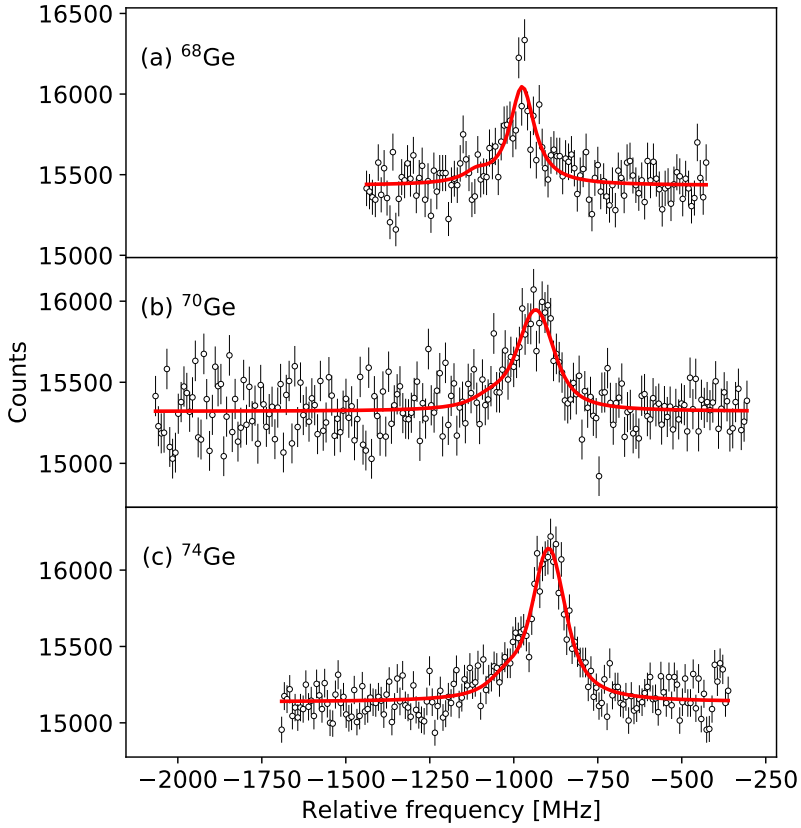

Figure 5.6: Hfs spectrum of ^{68,70,74}Ge. The peaks are fitted with a voigt profile. More details in the text.

5.3.3 Fitting the odd Z isotopes: ^{69,71,73}Ge

Fitting the odd Z isotopes of germanium can be more challenging since their hfs spectra present more than one peak because of their non-zero nuclear spins. As it has been already discussed in Fig. 5.1, these

peaks might partially or fully overlap, making the fitting process more complicating.

In order to ease this process, the lorentzian FWHM and the poisson factor of the side peak were restricted to the range of the value acquired from ^{72}Ge and the side peak offset was restricted to the range of the value calculated by kinematics. All three parameters were again shared for the simultaneous fit. The centre of gravity was an independent variable for every spectrum and was fitted separately. Results for these shared parameters are given in Tab. 5.4

Table 5.4: Results for the shared parameters of the ^{69,71,73}Ge fit.

Isotope	FWHML (MHz)	Offset (MHz)	Poisson factor
^{69}Ge	88(3)	-133(4)	0.092(7)
^{71}Ge	88(3)	-128(3)	0.098(6)
^{73}Ge	89(3)	-127(3)	0.095(6)

For the odd-A isotopes of germanium, there are hfs constant values available in literature with high precision, especially for ^{73}Ge where the level of accuracy is beyond what could be achieved by the CLS technique. Non-zero hfs constants means that multiple peaks will be present in the hfs spectrum and every peak will have a different intensity which can be calculated via the Racah formalism.

The Racah formalism, though, describes the peak intensity in a hfs spectrum with no laser power. But, in most CLS experiments, some hfs transitions might saturate from the applied laser power resulting in deviations between the observed and theoretically expected peak intensity.

For all these reasons, each isotope was fitted fixing the hfs constants to literature and free peak intensities, shared for all the spectra of each isotope. To check the statistical validity of such a procedure, each isotope was also fitted additionally with no constraints in the hfs constants, once with free peak intensities and once with intensities fixed to Racah values.

To be more precise, for fitting ^{73}Ge, the hfs constants were first fixed to the high-accuracy literature values [76]. Also, in the hfs spectrum of this isotope, the hfs transition $F = 9 \rightarrow F = 9$ lays in-between the

Table 5.5: Results of hfs constants and isotope shift for ^{73}Ge.

Hfs constants:	A_l (MHz)	A_u (MHz)	B_l (MHz)	B_u (MHz)	IS (MHz)
fixed to lit.	+15.5480(18)	-262.2(12)	-54.566(9)	+40(6)	+ 8(3)
free	+16.1(5)	-262.8(7)	-43(5)	+30(6)	+5(2)
free & Racah int.	+15.8(4)	-261.3(4)	-48(4)	+42(4)	+12(2)

Table 5.6: Results of hfs constants and isotope shift for ^{71}Ge.

Hfs constants:	A_l (MHz)	A_u (MHz)	B_l (MHz)	B_u (MHz)	IS (MHz)
fixed to lit.	-87.005(3)	+1460.8(16)			-67(4)
free	-84.7(14)	+1461.9(17)			-67(4)
free & Racah int.	-86(2)	+1449(3)			-70(3)

Table 5.7: Results of hfs constants and isotope shift for ^{69}Ge.

Hfs constants:	A_l (MHz)	A_u (MHz)	B_l (MHz)	B_u (MHz)	IS (MHz)
fixed to lit.	-23.40(3)	+496.2(6)	+8.28(8)	-24(3)	-81(7)
free	-29.0(7)	+494.6(9)	+32(2)	-21(3)	-78(7)
free & Racah int.	-27.8(7)	+494.8(7)	+31(3)	-29(3)	-83(7)

doublet in the middle of the spectrum (as seen in Fig. 5.1) with very low intensity, resulting in difficulty in resolving it. For that reason, this specific transition in the spectrum of ^{73}Ge is set to its Racah value. The results of the different fitting procedures for fitting ^{73}Ge are presented in Tab. 5.5 while the best fit is shown in Fig. 5.7(c), corresponding to hfs constants fixed to literature values and free peak intensities. The isotope shifts of the different fitting procedures for ^{73}Ge are also presented in Tab. 5.5, while all the centre of gravity values are given in Appendix B.

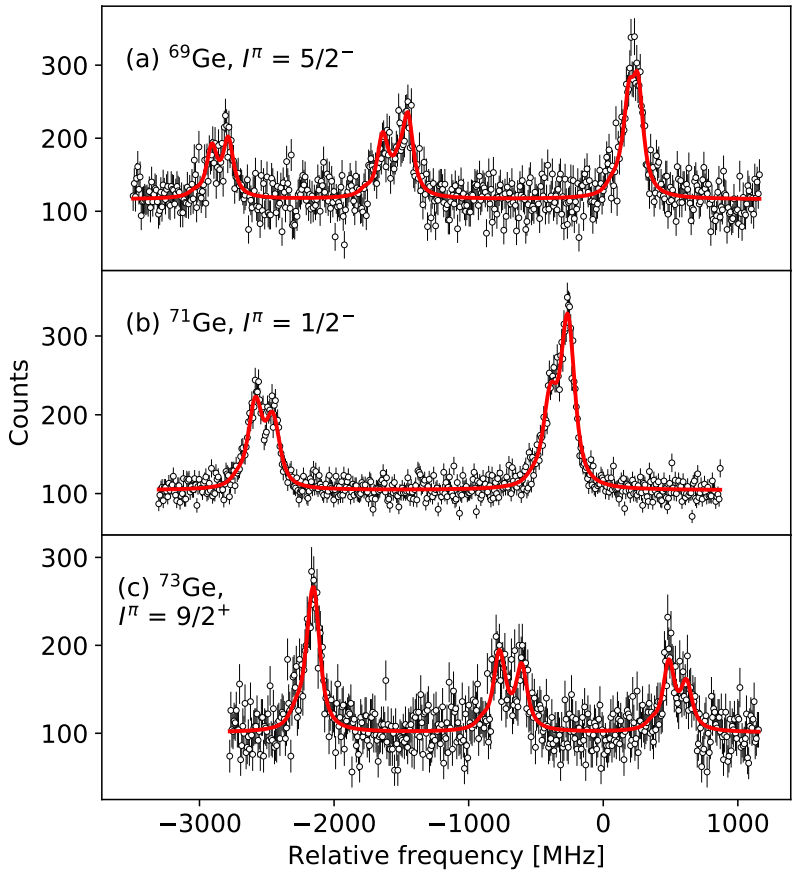

Figure 5.7: Hfs spectrum of ^{69,71,73}Ge. The peaks are fitted with a voigt profile. More details in the text.

For ^{71}Ge, the fitting process included fixing the hfs constants to the high-accuracy literature values [97] as well. Results for this isotope are presented in Tab. 5.6 and Fig. 5.7(b) where the best fit is shown. The isotope shifts results for ^{71}Ge are also presented in Tab. 5.6, while all the centre of gravity values are given in Appendix B. Note here the absence of B factors since the nuclear spin of ^{71}Ge is $I = 1/2^-$.

Following the standard process for ^{69}Ge proves to be problematic. Fixing the hfs constants to the literature values [74] results in the A and B ratio not being in agreement with the values of ^{71,73}Ge, as seen in Tab. 5.8. For the A ratio, a possible reason would be the presence of Hyperfine Anomaly (hfa) but the disagreement is too large for hfa to be the source ($\sim$30%). On the other hand, hfa would not explain the B ratio disagreement. For that reason, the spectra of ^{69}Ge were fitted with free hfs parameters assuming there is mistake in literature. This will be discussed further in the next chapter and in the publication therein. Results are presented in Tab. 5.7 along with the best fit in Fig. 5.7(a) where it is to be noted that the best fit corresponds to free hfs constants and not fixed in literature values. The isotope shifts of the different fitting procedures for ^{69}Ge are also presented in Tab. 5.7, while all the centre of gravity values are given in Appendix B.

Table 5.8: Ratios of A and B factors for ^{69,71,73}Ge.

Isotope	Hfs constants:	A_u/A_l	B_u/B_l
^{73}Ge	fixed to lit.	-16.87(8)	-0.73(11)
^{71}Ge	fixed to lit.	-17.79(2)	
^{69}Ge	fixed to lit.	-21.21(4)	-2.8(4)
^{69}Ge	free	-17.1(4)	-0.64(11)

5.3.4 Analysis summary

In Tabs. 5.10 & 5.9 the final hfs parameters for ^{69,71,73}Ge and isotope shifts for $^{68-74}$Ge are presented, as extracted from this analysis.

Table 5.9: Isotope shifts for $^{68-74}$Ge.

Isotope	$\delta\nu^{A,72}$ (MHz)
^{68}Ge	-46(5)
^{69}Ge	-78(7)
^{70}Ge	-32(3)
^{71}Ge	-67(4)
^{72}Ge	0
^{73}Ge	+8(3)
^{74}Ge	+51(2)

Table 5.10: Final hfs constants for ^{69,71,73}Ge.

Isotope	I^π	A_l (MHz)	A_u (MHz)	B_l (MHz)	B_l (MHz)
^{73}Ge	$9/2^+$	+15.5480(18) [76]	-262.2(12)	-54.566(9) [76]	+40(6)
^{71}Ge	$1/2^-$	-87.005 [97]	+1460.8(16)		
^{69}Ge	$5/2^-$	-29.0(7)	+494.6(9)	+32(2)	-21(3)

Chapter 6

Structure of germanium nuclei

In this chapter the nuclear moments and mean square charge radii of the germanium isotopes will be presented. A discussion and interpretation of the results is also presented. In this chapter, the publication of the nuclear moments of ^{69,71,73}Ge is also included.

6.1 Article I: Nuclear moments of germanium isotopes near $N = 40$

This article presents details about the experiment of germanium isotopes. The experiment took place at COLLAPS in May 2018. The analysis of the hfs spectra is presented and the extracted hfs parameters are compared with atomic Fock-space coupled-cluster (FSCC) calculations. The extracted nuclear moments of ^{69,71,73}Ge are presented, and compared with calculated values of the JUN45 interaction. The germanium moments are compared with the moments of other isotopic chains in the region and systematics of the nuclear structure evolution are discussed.

I have participated in the experiment and analysed the data, and prepared the draft of the paper with help of X.F. Yang. The paper was published in Physical Review C **202**, 054331 (30 November 2020).

Nuclear Moments of Germanium Isotopes around $N = 40$

A. Kanellakopoulos,[1] X. F. Yang,[2,1,*] M. L. Bissell,[3] M. L. Reitsma,[4] S. W. Bai,[2] J. Billowes,[3] K. Blaum,[5] A. Borschevsky,[4] B. Cheal,[6] C. S. Devlin,[6] R. F. Garcia Ruiz,[7,†] H. Heylen,[7] S. Kaufmann,[8,9] K. König,[8,‡] Á. Koszorús,[1,§] S. Lechner,[7,10] S. Malbrunot-Ettenauer,[7] R. Neugart,[5,9] G. Neyens,[1,7] W. Nörtershäuser,[8] T. Ratajczyk,[8] L. V. Rodríguez,[5,11,¶] S. Sels,[7,**] S. J. Wang,[2] L. Xie,[3] Z. Y. Xu,[1,††] and D. T. Yordanov[11]

[1] *Instituut voor Kern- en Stalingsfysica, KU Leuven, B-3001, Leuven, Belgium*

[2] *School of Physics and State Key Laboratory of Nuclear Physics and Technology, Peking University, Beijing 100871, China*

[3] *Department of Physics and Astronomy, The University of Manchester, Manchester, M13 9PL, United Kingdom*

[4] *Faculty of Science and Engineering, Van Swinderen Institute for Particle Physics and Gravity, University of Groningen, 9747 AG Groningen, The Netherlands*

[5] *Max-Planck-Institut für Kernphysik, D-69117 Heidelberg, Germany*

[6] *Oliver Lodge Laboratory, Oxford Street, University of Liverpool, Liverpool, L69 7ZE, United Kingdom*

[7] *Experimental Physics Department, CERN, CH-1211 Geneva 23, Switzerland*

[8] *Institut für Kernphysik, TU Darmstadt, D-64289 Darmstadt, Germany*

[9] *Institut für Kernchemie, Universität Mainz, D-55128 Mainz, Germany*

[10] *Technische Universität Wien, Karlsplatz 13, A-1040 Wien, Austria*

[11] *Institut de Physique Nucléaire,*

CNRS-IN2P3, Université Paris-Sud,
Université Paris-Saclay, 91406 Orsay, France

(Dated: July 24, 2021)

Collinear laser spectroscopy measurements were performed on ^{69,71,73}Ge isotopes ($Z = 32$) at ISOLDE-CERN. The hyperfine structure of the $4s^2 4p^2\ ^3P_1 \rightarrow 4s^2 4p 5s\ ^3P_1^o$ transition of the germanium atom was probed with laser light of 269 nm, produced by combining the frequency-mixing and frequency-doubling techniques. The hyperfine fields for both atomic levels were calculated using state-of-the-art atomic relativistic Fock-space coupled-cluster calculations. A new ^{73}Ge quadrupole moment was determined from these calculations and previously measured precision hyperfine parameters, yielding $Q_{\rm s} = -0.198(4)$ b, in excellent agreement with the literature value from molecular calculations. The moments of ^{69}Ge have been revised: $\mu = +0.920(5)\ \mu_N$ and $Q_{\rm s}= +0.114(8)$ b, and those of ^{71}Ge have been confirmed. The experimental moments around $N = 40$ are interpreted with large-scale shell-model calculations using the JUN45 interaction, revealing rather mixed wave function configurations, although their g-factors are lying close to the effective single-particle values. Through a comparison with neighboring isotones, the structural change from the single-particle nature of nickel to deformation in germanium is further investigated around $N = 40$.

* xiaofei.yang@pku.edu.cn
† Present address: Massachusetts Institute of Technology, Cambridge, MA, USA
‡ Present adress: National Superconducting Cyclotron Laboratory, Michigan State University, East Lansing, Michigan 48824, USA
§ Present address: Oliver Lodge Laboratory, Oxford Street, University of Liverpool, Liverpool, L69 7ZE, United Kingdom
¶ Present address: Experimental Physics Department, CERN, CH-1211 Geneva 23, Switzerland
** Present address: Instituut voor Kern- en Stalingsfysica, KU Leuven, B-3001, Leuven, Belgium
†† Present address: Department of Physics and Astronomy, University of Tennessee, 37996 Knoxville, TN, USA

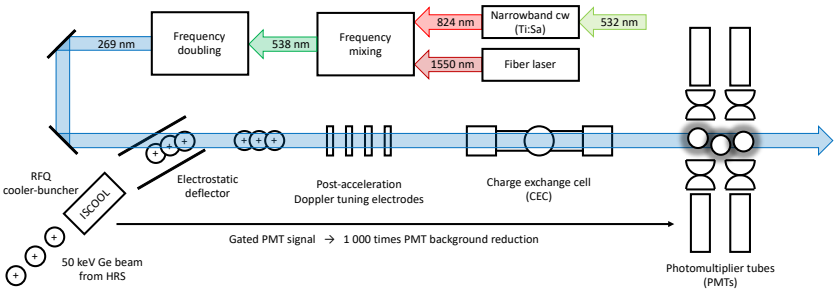

FIG. 1. A schematic view of the COLLAPS experimental setup and the laser frequency-mixing and frequency-doubling system. For details see text.

I. INTRODUCTION

Over the years, structural changes have been intensively investigated in the region between the semi-magic ^{68}Ni and the doubly-magic ^{78}Ni [1–6]. The investigation involves multiple experimental methods as well as theoretical models, which provide various nuclear properties (masses, spins, life-times, transition probabilities, excitation energies, moments and radii), aiming to get a global view of the nuclear structure in this region. As studies deepen, more interesting nuclear phenomena appear. Some examples are: collective effects occur around and above $N = 40$ [7–10]; the proton $p_{3/2}$ and $f_{5/2}$ orbitals invert as neutrons are filling the neutron $g_{9/2}$ orbital due to the tensor part of the monopole interaction [5, 8, 11]; a spherical shape coexists with a deformed state around the neutron closed shells $N = 40, 50$ [12–14]; the indication of a weak sub-shell effect observed at $N = 40$ disappears quickly with more protons added above $Z = 28$ [3, 7].

The nuclear properties of ground and isomeric states, such as spins,

moments and charge radii, have made significant contributions in elucidating the above-mentioned nuclear phenomena. This was achieved by laser spectroscopy measurements on the isotopic chains of nickel ($Z = 28$), copper ($Z = 29$), zinc ($Z = 30$) and gallium ($Z = 31$) [3, 5–8, 11, 13–18]. Nuclear spins and magnetic dipole moments are sensitive probes of the single-particle nature or configuration mixing of the wave functions [5, 6, 8, 11], while the electric quadrupole moment and charge radii tell us more about the nuclear shape and collectivity [3, 13, 14].

Deformation, triaxiality and shape coexistence have been observed for zinc isotopes, which have also been reported for germanium isotopes around $N = 40$ based on γ-spectroscopy and reaction experiments [7, 19–21]. Germanium ($Z = 32$) has four protons outside the $Z = 28$ major shell closure, which may induce additional correlations leading to a complex wavefunction and collective effects for the low-lying states of germanium isotopes around $N = 40$ [19, 22, 23]. This collective feature can be further investigated with the nuclear moment measurements of germanium isotopes around $N = 40$ in combination with wave function calculations using large-scale shell-model interactions.

Until now, collinear laser spectroscopy has not been applied to study germanium isotopes, due to the fact that (1) germanium species cannot be easily produced at ISOL facilities, and (2) the suitable fine structure transitions are not easily accessible with standard laser equipment. In this article, we report the first hyperfine structure (hfs) measurement in

the $4s^2 4p^2\,{}^3P_1 \rightarrow 4s^2 4p5s\,{}^3P_1^o$ transition of ^{69,71,73}Ge atoms by combining the frequency-mixing and frequency-doubling laser techniques. State-of-the-art relativistic Fock-Space Coupled-Cluster (FSCC) calculations of the atomic hyperfine fields and electric field gradients have been performed, showing a good agreement with the experimental values, and thus benchmarking these atomic theories. The calculations also reveal that incorrect nuclear moments have been reported for ^{69}Ge from earlier atomic beam magnetic resonance studies [24]. The extracted nuclear moments are compared with large-scale shell-model calculations using the JUN45 interaction in the $f_{5/2}pg_{9/2}$ model space in order to understand the collective effects. The systematic comparison of the nuclear moments of the $9/2^+$ states in zinc ($Z = 30$), germanium ($Z = 32$) and selenium ($Z = 34$) allow the investigation of the structural evolution from single-particle to collective effects around $N = 40$ as more protons are added above the $Z = 28$ shell closure.

II. EXPERIMENTAL PROCEDURE

The experiment was performed at the collinear laser spectroscopy setup, COLLAPS [25], located at ISOLDE-CERN. The radioactive germanium isotopes were produced by a 1.4-GeV proton beam impinging on a ZrO_2 target with a sulphur leak. The sulphur vapour was introduced into the target material where the sulphur atoms bind to form volatile GeS molecules. These molecules easily diffuse out of the target and then disassociate under electron impact to form germanium

ions inside a plasma source. The germanium ions were accelerated to 50 keV, mass separated using the high-resolution isotope separator (HRS) and subsequently cooled and bunched in a gas-filled linear Paul trap (ISCOOL) [26]. The accumulated ions were released in short bunches with a typical temporal width of 5 μs every 5 ms. Due to the large isobaric contamination in all of the Ge beams [27], the accumulation time was optimized at 5 ms to avoid the overfilling of the ISCOOL.

As shown in Fig. 1, the bunched ion beam was then deflected into the COLLAPS beamline, where it was neutralized in-flight by passing through a charge exchange (CE) cell filled with sodium vapor. The state $4s^2 4p^2\,{}^3P_1$ of the germanium atom was populated in the neutralization process [28]. A frequency fixed continuous-wave (cw) laser beam, overlapped with the germanium beam in a collinear geometry, was used to probe the $4s^2 4p^2\,{}^3P_1 - 4s^2 4p5s\,{}^3P_1^o$ (269.13411 nm) transition of the germanium atom. By applying a varying voltage to the germanium ions before entering the CEC, neutralized germanium atoms were resonantly excited to the $4s^2 4p5s\,{}^3P_1^o$ state through Doppler tuning. The emitted fluorescence photons from the resonantly excited atoms were detected as a function of the tuning voltage, by the use of 4 photomultiplier tubes (PMTs) [29]. A software time gate was applied in order to select photons only when each bunch of germanium atoms passes and de-excites in front of the PMTs. This resulted in a reduction of the background from laser stray light, non-resonantly scattered photons and PMT dark counts by a

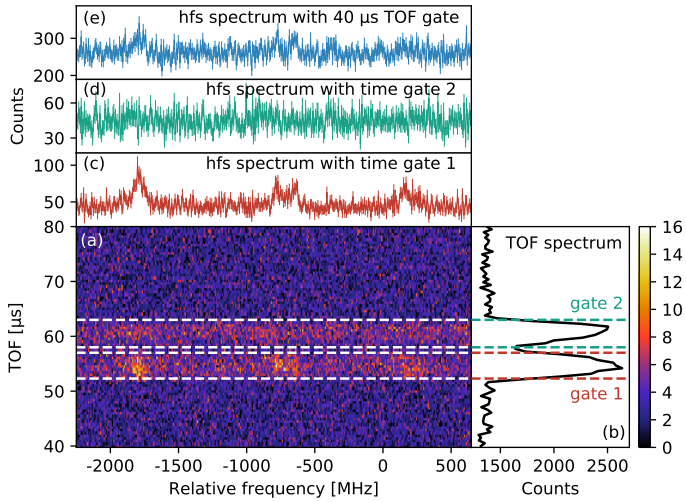

FIG. 2. Color-coded 2D plot with time vs frequency (voltage step) vs counts acquired for ^{73}Ge with the new DAQ system (TILDA) of COLLAPS. The two components presented in the TOF spectrum are corresponding to the germanium atom bunch (gate 1 in red) and the possible molecular contamination bunch (gate 2 in green). Gating on the germanium atom bunch allows the hfs spectrum to be reconstructed with a significantly reduced background.

factor of about 10^3.

To take full advantage of ISCOOL and to retain as much information on the beam structure in the recorded data as possible, a new data acquisition system (DAQ) was introduced at COLLAPS. It was developed at the TRIGA-SPEC setup in Mainz [30] and here we report its online-operation. The main advantage of this DAQ is the time-resolved photon detection. In order to reduce the photon background, the detection of photons has to be restricted to the time window when the bunched beam is traversing the detection region. Previously, this was realized by hardware gating,

which had to be adapted in advance for each isotope according to the time-of-flight (TOF) recorded. With the new DAQ, photons are recorded with a time stamp relative to the ion extraction trigger of ISCOOL. This is shown for ^{73}Ge in Fig. 2(a): the x-axis represents the scanning voltage, converted into frequency, while the y-axis is the TOF since the ISCOOL extraction pulse. The number of photons detected within a 500-ns interval during n-time extractions from ISCOOL are color-coded. These numbers are integrated along a specified time in Fig. 2(b), which provides the time structure of the bunch. Integration along a fixed frequency reveals the hfs resonance spectrum of the isotope, as illustrated in Fig. 2(c). The spectra in Fig. 2(c)-(d) are obtained by selecting events within the specific time window indicated with dashed horizontal lines in Fig. 2(a) and with their corresponding colored dashed lines in Fig. 2(b).

In Fig. 2(a) three regions can be clearly distinguished. Outside of the dashed lines, the background is dominated by stray laser light, which is weak compared to the more intense signal within the time gate of the bunch. One can clearly see that the bunch is separated into two parts, the first one arriving after about 52 μs, while the second one is delayed by another 5 μs. The time interval between two bunches released from ISCOOL is about 1000 times longer. Thus, the two consecutive 'bunches' seen in Fig. 2(a) are from photons emitted from two different species. Those with a heavier mass arrive later in front of the PMT's. In the first time window (gate 1) clear resonance spots are seen, as well as an additional beam-related but frequency-independent background (see also

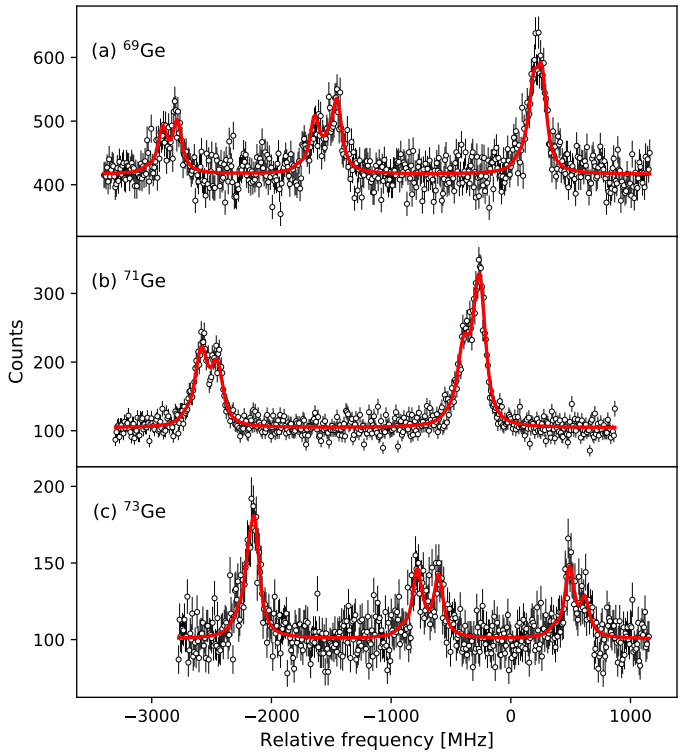

FIG. 3. Hyperfine structure spectra of ^{69,71,73}Ge in the $4s^2 4p^2\ ^3P_1 \rightarrow 4s^2 4p 5s\ ^3P_1^o$ transition. The red lines show the best fit with a Voigt line profile. Note that the production of the known short-lived isomers of ^{71,73}Ge ($T_{1/2}(^{71m}\mathrm{Ge}) = 20.41(18)$ ms and $T_{1/2}(^{73m}\mathrm{Ge}) = 499(11)$ ms) [31, 32] is at least 100 times lower than that of the ground state [33]. Thus, these isomers could not be observed in this experiment.

Fig. 2(c)). This background is attributed to the de-excitation of all contaminant neutral particles that were excited in the CE process. The second part of the bunch (gate 2) does not exhibit any resonance-like structures, only beam-related photon background, as seen in Fig. 2(d). It

is assumed that this beam-related photon background is due to laser-light scattering from the molecular contamination in the beam and de-excitations of these molecules excited via the CE process.

With the latest DAQ, these individual parts of the bunch can be clearly separated in online and offline analysis. Therefore, by gating on the first component (gate 1) instead of the plotted range (40 μs) of the TOF spectrum, the hfs spectrum of ^{73}Ge was obtained with a much improved signal-to-background ratio, as shown in Fig. 2(c) and Fig. 2(e), respectively.

One challenge for the laser spectroscopy measurement of germanium atoms is the production of the 269 nm cw laser light. It requires frequency-doubling of the wavelength 538 nm. This wavelength is lying in the 'green gap' region, which is not covered by the commonly used continuous wave (cw) Ti:Sa and dye laser systems. To bridge this wavelength gap, a frequency mixing method was employed. As shown in Fig. 1, a 824 nm laser beam from a Ti:Sa laser cavity (Sirah Matisse-2) and a 1550 nm laser beam generated by a single-frequency fiber laser (Koheras Boostik E 15) are superimposed and single-pass through a periodically poled crystal in a frequency mixing unit (Sirah MixTrain) to generate the sum frequency of 538 nm ($\frac{1}{\lambda} = \frac{1}{\lambda_1} + \frac{1}{\lambda_2}$). This light is then coupled into a frequency doubling unit (Sirah WaveTrain) to produce 269 nm light with an output power around 90 mW. A small fraction of the output light from the frequency mixing unit was locked to a wavelength meter (HighFinesse WSU10), which was regularly calibrated

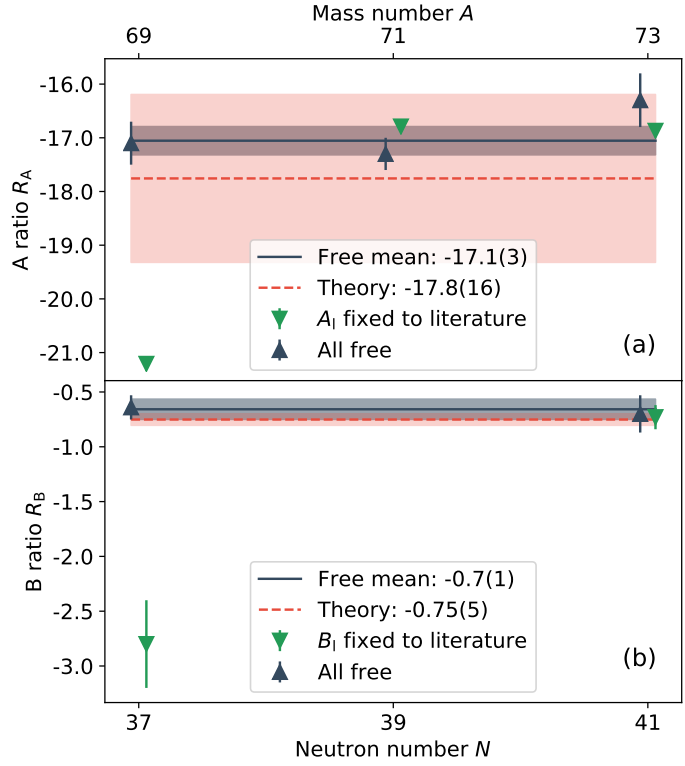

FIG. 4. Ratio of the A (a) and B hyperfine constants (b) for the $4p^2\,{}^3P_1$ (lower) and $4p5s\,{}^3P_1^o$ (upper) atomic states, deduced with two fitting procedures. One with the A_I and B_I values for each isotope fixed (green) to the high-precision value reported in literature [24, 34, 36], and one with all hyperfine constants as free fit parameters (black). The hyperfine constants ratios calculated with atomic relativistic FSCC are shown by red dashed lines.

with a stabilized diode laser (Toptica DLPRO780) locked to the $F = 2 \rightarrow F = 3$ hyperfine transition of the D1 line in ^{87}Rb.

TABLE I. Magnetic and electric hfs constants (A and B) for both atomic states ($4s^2 4p^2\,{}^3P_1$ and $4s^2 4p 5s\,{}^3P_1^o$) obtained from this work. The numbers from Refs. [24, 34, 35] are also summarized as a comparison.

A	N	I^π	$T_{1/2}$	$A_\mathrm{l}^\mathrm{lit}$ (MHz)	A_l (MHz)	A_u (MHz)	$B_\mathrm{l}^\mathrm{lit}$ (MHz)	B_l (MHz)	B_u (MHz)
69	37	$5/2^-$	39.05(10) h	$\mp$23.40(3) [24]	$-29.0(7)$	$+494.6(9)$	$\pm$8.28(8) [24]	$+32(2)$[a]	$-21(3)$[a]
71	39	$1/2^-$	11.43(3) d	$-87.005(3)$ [34]		$+1460.8(16)$			
73	41	$9/2^+$	stable	$+15.5480(18)$ [35]		$-262.2(12)$	$-54.566(9)$ [35]		$+40(6)$

[a] Correlation C(B_l, B_u) = -0.445

III. RESULTS

The obtained hfs spectra of ^{69,71,73}Ge isotopes, as shown in Fig. 3, were fitted with a χ^2-minimization Python routine using the SATLAS package [37]. A Voigt profile with one side peak was used to compensate for the slightly asymmetric resonance peaks, which resulted from the energy loss due to the population of higher atomic states or the collision-excitation in the charge exchange process [38, 39]. All the recorded hfs spectra of each individual isotope were fitted simultaneously, generating one optimal reduced χ^2, with magnetic dipole and electric quadrupole hyperfine constants (A and B) as common fit parameters for each isotope.

The A and B parameters for the lower atomic state ($4s^2 4p^2\,{}^3P_1$), named A_l and B_l in the following, are reported in literature with high precision for each of the three odd-A germanium isotopes from atomic beam magnetic

TABLE II. Deduced $R_\mathrm{A} = A_\mathrm{u}/A_\mathrm{l}$ and $R_\mathrm{B} = B_\mathrm{u}/B_\mathrm{l}$ for ^{69,71,73}Ge isotopes with the A_l and B_l fixed to literature values or with all hyperfine constants as free fit parameters.

	R_A		R_B	
	All free	A_l fixed to lit.	All free	B_l fixed to lit.
^{69}Ge	−17.1(4)	−21.21(4)	−0.64(11)	−2.8(4)
^{71}Ge	−17.3(3)	−16.79(2)		
^{73}Ge	−16.3(5)	−16.87(8)	−0.70(17)	−0.73(11)

resonance experiments [24, 34–36], as summarized in Tab. I. We therefore fitted our data in two ways: (1) with the A_l and B_l values fixed to the literature value and upper hyperfine constants as free fit parameters for each isotope, and (2) with all lower and upper hyperfine constants as free fit parameters. The ratio of the hyperfine parameters of the upper and lower atomic states ($R_\mathrm{A} = A_\mathrm{u}/A_\mathrm{l}$, $R_\mathrm{B} = B_\mathrm{u}/B_\mathrm{l}$) reflect the ratio of the atomic hyperfine fields of both levels. These ratios should be the same for all isotopes, apart from a possible small hyperfine anomaly that can cause some scatter of the order of at most a few percent in R_A. In Table II, as well as in Fig. 4, the ratio of R_A and R_B resulting from the two fit procedures are shown. When using the first fitting procedure, both the A and B factor ratios for ^{69}Ge deviate strongly from those observed for the other isotopes, suggesting a problem with the reported hyperfine parameters of ^{69}Ge [24], from which the literature nuclear moments have been deduced. When all four hyperfine parameters are free fit parameters, the deduced ratios of R_A and R_B are consistent for all three isotopes, as shown in Tab. II and Fig. 4. To corroborate these conclusions, state-of-the-art atomic calculations were performed, as discussed in the following section.

A. Atomic hyperfine field calculations

To further investigate the aforementioned discrepancy between the hyperfine constants from literature and our experimental results for ^{69}Ge, we performed atomic calculations to obtain the hyperfine fields of

TABLE III. Atomic A_0 and q parameters extracted from ^{73}Ge experimental results and calculated with atomic relativistic FSCC method.

At. state	$A^{\rm exp}$ (MHz)	$A_0^{\rm exp}$ (MHz)	$A_0^{\rm th}$ (MHz)	$B^{\rm exp}$ (MHz)	$q^{\rm exp}$ (MHz/b)	$q^{\rm th}$ (MHz/b)
$4p^2\,{}^3P_1$	+15.5480(18) [35]	−79.667(10)	−74(6)	−54.566(9) [35]	+278.4(14)	+277(8)
$4p^2\,{}^3P_2$	−64.4270(7) [35]	+330.12(2)	+321(11)	+111.825(13) [35]	−571(3)	−564(17)
$4p5s\,{}^3P_1^o$	−262.2(12)[a]	+1343(6)	+1314(45)	+40(6)[a]	−204(31)	−208(13)

[a] Hyperfine parameters measured in this work.

TABLE IV. Magnetic dipole and electric quadrupole moments of ^{69,71,73}Ge isotopes compared with JUN45. The numbers from Refs.[24, 35, 40, 41] are also summarized as a comparison.

A	N	I^π	$\mu^{\rm lit}$ (μ_N)	$\mu^{\rm exp}$ (μ_N)	$\mu^{\rm JUN45}$ (μ_N)	$Q_{\rm s}^{\rm lit}$ (b)	$Q_{\rm s}^{\rm exp}$ (b)	$Q_{\rm s}^{\rm JUN45}$ (b)
69	37	$5/2^-$	0.735(7)[24]	+0.920(5)	+1.048	+0.027(5)[24]	+0.114(7)	+0.150
71	39	$1/2^-$	+0.54606(7) [35]	+0.547(5)	+0.438			
73	41	$9/2^+$	−0.87824(5) [40]	-0.904(21)[a]	−0.955	−0.196(1) [41]	-0.198(4)[a]	−0.258

[a] Weighted mean of the moments extracted from the measured hyperfine parameters and calculated hyperfine fields of the 3 transitions in Tab. III.

three atomic fine structure levels ($4s^2 4p^2\ ^3P_1$, $4s^2 4p^2\ ^3P_2$ and $4s^2 4p5s\ ^3P_1^o$), for which experimental information is available for the stable ^{73}Ge isotope [35].

High-quality treatment of relativistic and electron correlation effects is required to obtain accurate and reliable computational results. Therefore, the multireference relativistic FSCC method [42, 43] is employed for the investigation of the electric field gradients (EFGs) ($q^{\rm th}$) and the hyperfine magnetic field constants ($A_0^{\rm th}$). This method was shown to be one of the most powerful approaches for treatment of spectra and properties of heavy many-electron atoms [44].

The FSCC method requires a closed shell reference state from which the ground state and excited states can be reached by adding or removing electrons. Neutral germanium has an open shell ground state electron configuration [Ar]$3d^{10}4s^2 4p^2$ and thus the closed shell Ge^{2+} system ([Ar]$3d^{10}4s^2$) is used as the reference state. The ground state and excited states of interest are reached by adding two electrons to the corresponding virtual orbitals, which comprise the model space. The intermediate Hamiltonian (IH) approach is applied to avoid the intruder-state problem [45]. The finite field method [46] is used to determine the $q^{\rm th}$ and $A_0^{\rm th}$ properties, as described in Refs. [47, 48]. All calculations are carried out in the framework of the Dirac-Coulomb Hamiltonian and the nuclear charge distribution is modeled by a Gaussian function as described in Ref. [49]. The $q^{\rm th}$ calculations were carried out using the DIRAC15 program package [50], while DIRAC17

was used for the $A_0^{\rm th}$ calculations [51]. The final values are obtained using the full 4-component DC Hamiltonian and the relativistic core-valence 4-zeta basis set of Dyall [52] (cv4z), augmented by three diffuse functions in each symmetry in an even-tempered fashion. A large model space was used, consisting of the $4p$ $5s$ ($4d$ $5p$ $6s$ $4f$ $5d$ $6p$ $7s$ $5f$ $5g$ $7p$ $6d$ $7d$ $8p$ $6g$ $8s$ $6f$) orbitals, where the orbitals in parentheses are in the intermediate space P_i. All the electrons were correlated and virtual orbitals with energies up to 500 a.u. were included in the calculation. The finite field perturbation strength λ was 1×10^{-6} for the $q^{\rm th}$ calculations and 1×10^{-4} for $A_0^{\rm th}$.

To estimate the uncertainty on the calculated values, we have investigated the effect of various computational parameters: the error from the limited size of the basis set, model space and virtual space, while also estimating the contribution from higher order excitations and the relativistic Gaunt term. These sources of error are combined by assuming them to be independent to give a total conservative uncertainty estimate for each calculated property. The uncertainty of $q^{\rm th}$ is 3.0 % for the $4p^2\ {}^3P_1$ and $4p^2$ states and 6.4 % for $4p5s\ {}^3P_1^o$, while for $A_0^{\rm th}$ the uncertainties are 7.8 %, 3.5 % and 3.4 % respectively for these three states. The final recommended values and uncertainties for $q^{\rm th}$ and $A_0^{\rm th}$ are shown in Tab. III. Further details on the procedure used for the calculation of these properties and the uncertainties can be found in Ref. [53].

The calculated atomic observables, A_0 and q, are proportional to the

magnetic hyperfine field (B_0) created by the electrons at the point of the nucleus, $A_0 = B_0/J$, and to the electric field gradient (V_{zz}) created by the electronic cloud, $q = eV_{zz}$, respectively. Here, J is the atomic spin. These atomic observables are related to the measured A and B parameters as follows: $A_0 = AI/\mu$ and $q = B/\,Q_{\rm s}$, with μ and $Q_{\rm s}$ the nuclear magnetic dipole moment and electric quadrupole moment, respectively, and I the nuclear spin. From the experimental hyperfine constants of the three atomic states taken from Refs. [35] and measured in this work, as well as the experimental magnetic and quadrupole moments from Refs. [40, 41], we can calculate the experimental A_0 and q parameters for ^{73}Ge. These can be directly compared with atomic theory calculations, as presented in Tab. III. A remarkable agreement is achieved for both A_0 and q, for all three states within less than 5%. We further compared the ratios ($R_{\rm A}$, $R_{\rm B}$) of hyperfine constants of two atomic states ($4p^2\,{}^3P_1$ and $4p5s\,{}^3P_1^o$) measured in this work with the atomic calculation, as shown in Fig. 4. The ratios of the hyperfine constants from theory show a good agreement with experimental values for all three isotopes of ^{69,71,73}Ge obtained with fitting procedure (2). This further supports our experimental result for the $A_{\rm l}$ and $B_{\rm l}$ hyperfine constants of ^{69}Ge.

B. Hfs constants and nuclear moments

As mentioned above, both our experimental results and the atomic calculations are inconsistent with the literature hyperfine constants for the $4p^2\,{}^3P_1$ atomic state of ^{69}Ge. A revision of the lower state hfs parameters

of ^{69}Ge is therefore suggested. From our measurements, the upper-state hyperfine parameters, A_{u} and B_{u}, can also be determined for the first time for all isotopes, yielding an independent measurement of the nuclear moments. For ^{71,73}Ge, the final A_{u} and B_{u} are obtained with A_{l} and B_{l} fixed to the literature values [34, 35], since they are known with high-precision. In Tab. I, the revised hyperfine parameters of the lower atomic state for ^{69}Ge, and the newly measured hyperfine constants of the upper atomic state for ^{69,71,73}Ge are shown together with literature values.

A precise nuclear magnetic moment of ^{73}Ge has recently been redetermined using gas-phase NMR measurements on GeH_4 [40] and a precise electric quadrupole moment was extracted from molecular microwave data of GeO and GeS [41]. Thus, the magnetic dipole μ and electric quadrupole Q_{s} moments of ^{69,71}Ge can be calculated from the experimental A and B parameters in a model independent way relative to those of ^{73}Ge, by using:

$$\mu = \frac{IA}{I_{\mathrm{ref}} A_{\mathrm{ref}}} \mu_{\mathrm{ref}} \tag{1}$$

$$Q_{\mathrm{s}} = \frac{B}{B_{\mathrm{ref}}} Q_{\mathrm{s,ref}} \tag{2}$$

The large A_{u} hyperfine parameter is used to extract the magnetic moments of ^{69,71}Ge via Eq. (1). Since the hyperfine B parameters for both atomic states are comparable in magnitude, two sets of electric quadrupole moments are extracted from B_{l} and B_{u} using Eq. (2). We use the weighted average of the two quadrupole moments as the final

value, after taking into account the correlation between the two hyperfine B parameters [54]. The results are summarized in Tab. IV together with the literature values.

For the reference isotope ^{73}Ge, we also determine an independent set of nuclear moments, using the measured hyperfine parameters and calculated hyperfine fields for each of the three atomic states shown in Tab. III. These moments are fully consistent with the literature values (Tab. IV), in particular for the quadrupole moment reaching almost similar precision. This illustrates the significant progress that has been made in atomic calculations in the last few years.

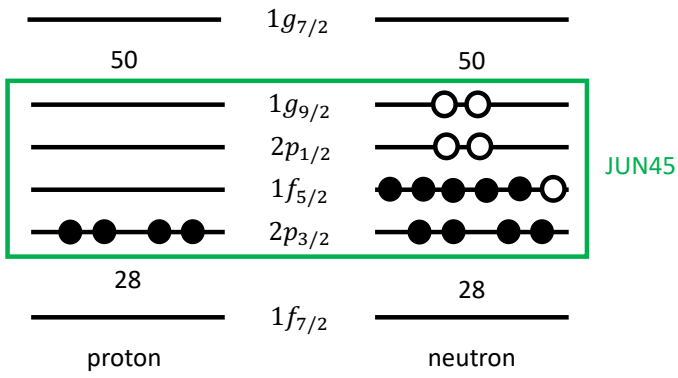

FIG. 5. Proton and neutron orbitals around the $Z, N = 28$ and the $Z, N = 50$ major shell closures according the nuclear shell-model. The model space of the effective interaction JUN45 is also marked.

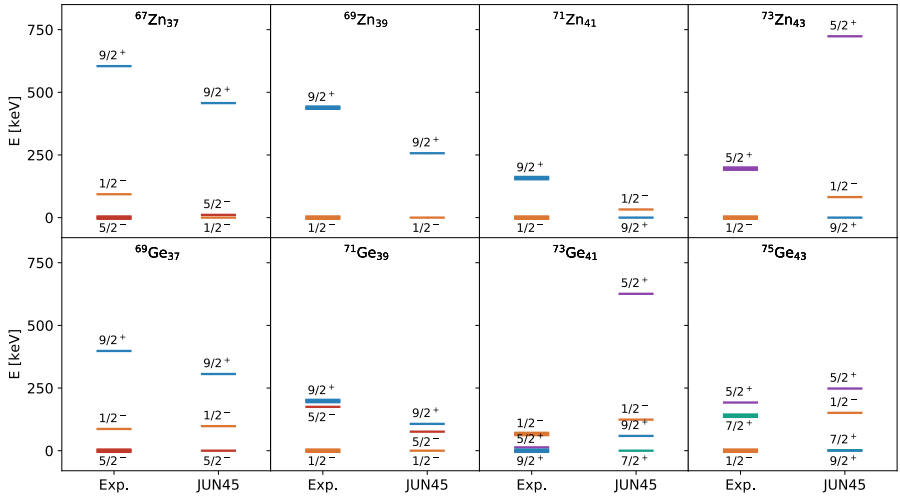

FIG. 6. Ground and low-lying excited (isomeric) states of $^{67-73}$Zn (top) and $^{69-75}$Ge (bottom) compared to results from JUN45 calculations. States with half-lives of at least 10 ns and a firm spin assignment are plotted. Thick lines represent states with half-lives longer than 1 ms.

IV. DISCUSSION

The relevant proton and neutron shells in the nickel mass region are displayed in Fig. 5. For the even-Z elements (like nickel, zinc and germanium), with neutron numbers between $N = 28$ and $N = 50$, the neutrons are expected to dominate the ground state structure of the odd-A isotopes in a naive single particle shell-model picture. By filling the $\nu 2p_{3/2}, \nu 1f_{5/2}, \nu 2p_{1/2}, \nu 1g_{9/2}$ orbitals, this would lead to ground-state (g.s.) spins of $3/2^-$, $5/2^-$, $1/2^-$ and $9/2^+$ for the odd-A isotopes, respectively. Thus, for ^{69}Ge and its isotones, ^{67}Zn and ^{65}Ni, with $N = 37$, the unpaired neutron is expected to occupy the $\nu f_{5/2}$ orbital,

resulting in a g.s. spin of $5/2^-$, which is consistent with the experimental assignment for each of these isotones [55–57]. For isotones with $N = 39$, a spin $1/2^-$ is then expected and also experimentally confirmed for ^{67}Ni, ^{69}Zn and ^{71}Ge [31, 56, 57]. So, below $N = 40$, the single-particle (SP) shell-model filling seems to be respected in germanium, despite having four valence protons, which could induce significant correlations and deformation. Moving to $N = 41$ and beyond, the filling of the $\nu g_{9/2}$ orbital is then beginning and the odd-N isotopes are all expected to have g.s. spin of $9/2^+$. This is indeed the case for ^{73}Ge and ^{69}Ni but not for ^{71}Zn [31, 32, 57]. This might suggest some stabilizing effect from a completely filled $\pi p_{3/2}$ orbital in ^{73}Ge, and onset of correlations between protons in the open $\pi p_{3/2}$ orbital in ^{71}Zn.

Recent studies have suggested that the structure of the zinc isotopes between $N = 40$ and $N = 50$ [5, 13] presents some complexity with long-lived SP-like or deformed isomers occurring in each of the odd-N isotopes. For the germanium isotopes, deformation was proposed for the even-A isotopes around $N = 40$ [22, 23] but a systematic discussion of the nuclear moments of the odd-N isotopes has not yet been done. We first investigate the nuclear structure around $N = 40$ by looking at the low-lying energy levels of $^{67-73}$Zn and $^{69-75}$Ge isotopes, as summarized in Fig. 6. Note that only the energy levels with a firm spin assignment and with measured half-lives longer than 10 ns are plotted, as nuclear moments have been measured for most of them [58]. These energy levels are also compared to large-scale shell-model calculations using the

JUN45 effective interaction [59] in the $f_{5/2}pg_{9/2}$ model space starting from a ^{56}Ni core, as illustrated in Fig. 5.

While the shell-model reproduces well the level ordering in germanium and zinc isotopes below $N = 40$, it fails to reproduce the complex level structure in both isotopic chains beyond $N = 40$ [13, 19–21]. This is apparent from the spins of the low lying states in ^{73,75}Ge and ^{73}Zn, which may not be easily understood from the normal filling of the shell-model orbitals. In the ^{73}Zn isotope, the isomeric character of the $5/2^+$ state allowed a measurement of its nuclear moments, and an unambiguous assignment of its spins and parity to be made, which was debated before in literature [5]. From the magnetic moment, it was clear that the unpaired neutrons mostly occupy the $g_{9/2}$ orbital, but the large quadrupole moment could be only explained by including proton and neutron excitations across $Z = 28$ and $N = 50$, leading to a triaxial shape [13]. Investigating the experimental electromagnetic properties of the low-lying states in the odd-A germanium isotopes will thus help to get a better understanding of their structure, which will be discussed in the following sections.

A. Magnetic Moments

The magnetic dipole moment, and more specifically the related g-factor ($g = \mu/I$), is an excellent probe of the orbital that is occupied by the unpaired particles (in this case neutrons). The available experimental g-factors of the ground and isomeric states of $^{69-75}$Ge are compared with the

effective SP g-factors of relevant orbitals, as presented in Fig. 7(a). The effective SP g-factors for the orbitals of $\nu f_{5/2}$, $\nu p_{1/2}$, $\nu g_{9/2}$ are calculated using effective g-factors of $g_s^{\rm eff} = 0.7 g_s^{\rm free}$ and $g_l^{\rm eff} = g_l^{\rm free}$, which are the typical values used in the region [14, 60].

The newly measured magnetic moment (and g-factor) of the $5/2^-$ g.s. of ^{69}Ge ($N = 37$) is in excellent agreement with the $\nu f_{5/2}$ effective SP value, intuitively pointing to its simple shell-model character of an unpaired valence neutron in the $\nu f_{5/2}$ orbital. The available experimental g-factors for the states with spin $9/2^+$ in ^{69,71,73}Ge lie close to the effective SP g-factor of the $g_{9/2}$ orbital, as shown in Fig. 7(a). Again this suggests a configuration dominated by an unpaired neutron in the $\nu g_{9/2}$ orbital. More interestingly, the g-factor of the $9/2^+$ state of ^{73}Ge deviates more from the effective SP g-factor (enhanced in Fig. 7(b)), pointing to a possible onset of collective effects from $N = 41$ onwards. As for the g.s. of ^{71,75}Ge, both having a spin/parity of $1/2^-$, the structure is likely dominated by an odd neutron in the $p_{1/2}$ orbital as the g-factors are close to the $\nu p_{1/2}$ SP value, yet deviate somewhat. Similar deviations have been observed for other $1/2^-$ states, e.g. in the neighbouring zinc isotopes [5], as well as for heavier isotopes with spin $1/2^-$ with a valence particle filling the $p_{1/2}$ orbital (e.g. Ag and In) [61].

These experimental g-factors are also compared with the shell-model calculations using the JUN45 interaction, as presented in Fig. 7(a). The calculations nicely reproduce the new experimental value of the $5/2^-$ g.s. of ^{69}Ge ($N = 37$) as well as the g-factors of the $9/2^+$ states in $^{69-73}$Ge.

However, the calculated wave functions for these states are found to be very fragmented. The calculated dominant configuration of the wave function for the $5/2^-$ g.s. of ^{69}Ge is about 26%. For the $9/2^+$ states of $^{69-73}$Ge, the main component of the wave function is, in all cases, less than 50%. For all the isotopes, the leading configuration is the same as that concluded from the effective SP g-factors. Surprisingly, the calculated g-factors of the $1/2^-$ g.s. of ^{71,75}Ge are close to the SP values, so they also deviate from the experimental values. Further theoretical investigation is needed to understand this deviation for the $1/2^-$ states.

Earlier studies have shown that the $N = 40$ subshell effect observed in the nickel and copper isotopes, quickly disappeared with more protons added above $Z = 28$, as described by various experimental observables: magnetic and quadrupole moments [5, 6, 8, 11], charge radii [3, 7, 16], nuclear masses [62, 63], $E(2^+)$ excitation energies, and $B(E2)$ transition rates [9, 10, 64, 65]. This indicates that an increase in collectivity around and above $N = 40$ is expected when going away from $Z = 28$, as has been observed in the zinc and gallium isotopes [5, 7–10, 13, 62–65].

In order to have a systematic investigation of the structural evolution from single-particle nature to the collective effect, we compare the experimental magnetic moments of the $9/2^+$ states for even-Z nuclei (zinc, germanium and selenium) around $N = 40$, as shown in Fig. 7(b). The g-factors of all the $9/2^+$ states in the region around $N = 40$ are close to the effective SP g-factor, clarifying the leading configuration of an unpaired neutron in the $g_{9/2}$ orbital in their wave functions. However,

a continuously increased deviation from the SP value is obvious from zinc, to germanium and selenium, giving a clear sign of the increased collectivity as more protons are added above $Z = 28$ closed shell. This is further confirmed by comparing the contribution of the main configuration of wave functions (single neutron in $g_{9/2}$ orbital), which is about ∼35% for ^{69}Zn and ∼14% for ^{71}Ge.

B. Quadrupole moments

The known experimental quadrupole moments of ground and isomeric states in $^{69-75}$Ge are presented in Fig. 8(a). The new value of the quadrupole moment of the $5/2^-$ g.s. in ^{69}Ge is well reproduced by the shell-model calculation. The same agreement can be found for the $9/2^+$ states of $^{71-73}$Ge. It is known from the above-discussed magnetic moments that the main configuration for these $9/2^+$ states comes from the unpaired valence neutron in the $\nu g_{9/2}$ orbital.

In Fig. 8(a), we see a linear trend in the quadrupole moments of these $9/2^+$ states, when more neutrons fill the $\nu g_{9/2}$ orbital. A similar trend has been observed in the neighboring zinc isotopes [5, 13], which are compared to those of germanium in Fig. 8(b). In the case of the zinc isotopic chain, the quadrupole moments of the $9/2^+$ states in ^{69}Zn ($N = 39$) and ^{79}Zn ($N = 49$) reflect a relatively pure configuration of single neutron particle and single neutron hole in the $\nu g_{9/2}$ orbital, respectively [5, 13], from which we estimated the SP quadrupole moment of $\nu g_{9/2}$ orbital (see Ref. [5] for more details). A linear trend for quadrupole moments with increased

neutron number for a seniority-1 $(\nu g_{9/2})^n$ configuration is then calculated, as shown with the black dash line in Fig. 8(b).

For the Ge isotopes, with only three measured quadrupole moments, it is difficult to make a firm conclusion. It appears that the slope of the curve is somewhat steeper than for the Zn isotopes, which would point to some enhanced deformation (correlations) for these isotopes with four protons outside the $Z = 28$ shell. However, more data on neutron-rich isotopes are needed to make a firm conclusion.

V. SUMMARY

The hfs of germanium atoms was measured for the first time in the $4s^2 4p^2\,{}^3P_1 \rightarrow 4s^2 4p 5s\,{}^3P_1^o$ atomic transition, taking advantage of the development of the laser frequency-mixing technique. A clear discrepancy with literature magnetic and electric hyperfine parameters is observed for ^{69}Ge. The systematic analysis of the hfs of ^{69,71,73}Ge isotopes obtained in this work requires a revision of the hyperfine constants for ^{69}Ge, resulting in new magnetic and quadrupole moments. State-of-the-art atomic relativistic Fock-Space Coupled-Cluster calculations were performed for the hyperfine fields in three atomic fine structure levels, allowing to determine the quadrupole moment of ^{73}Ge to a precision of 2%, in agreement with the precision value obtained from molecular theory calculations and experiments.

The available experimental nuclear moments of ground and isomeric states of $^{69-75}$Ge around $N = 40$ are interpreted through a comparison

to large-scale shell-model calculations in the $f_{5/2}pg_{9/2}$ model space. A comparison of the g-factors with the effective SP g-factors reveals the nature of the orbital occupied by the unpaired neutrons. Yet, the calculated wave functions reveal a very mixed configuration. Through a systematic comparison of the nuclear moments of germanium isotopes with its isotones (zinc and selenium) around $N = 40$, an increase in collectivity is observed, when protons are added to $Z = 28$, reflecting a sign of structural change from single particle to deformation when moving away from $Z = 28$.

To shed more light on the structural evolution in the region, further study of germanium isotopes up to $N = 50$ and even beyond is necessary, with the well-established laser systems and atomic transition studied in this work. This will allow us to have a better understanding of the structure changes in the nickel region, particularly, the gradual emergence of collectivity.

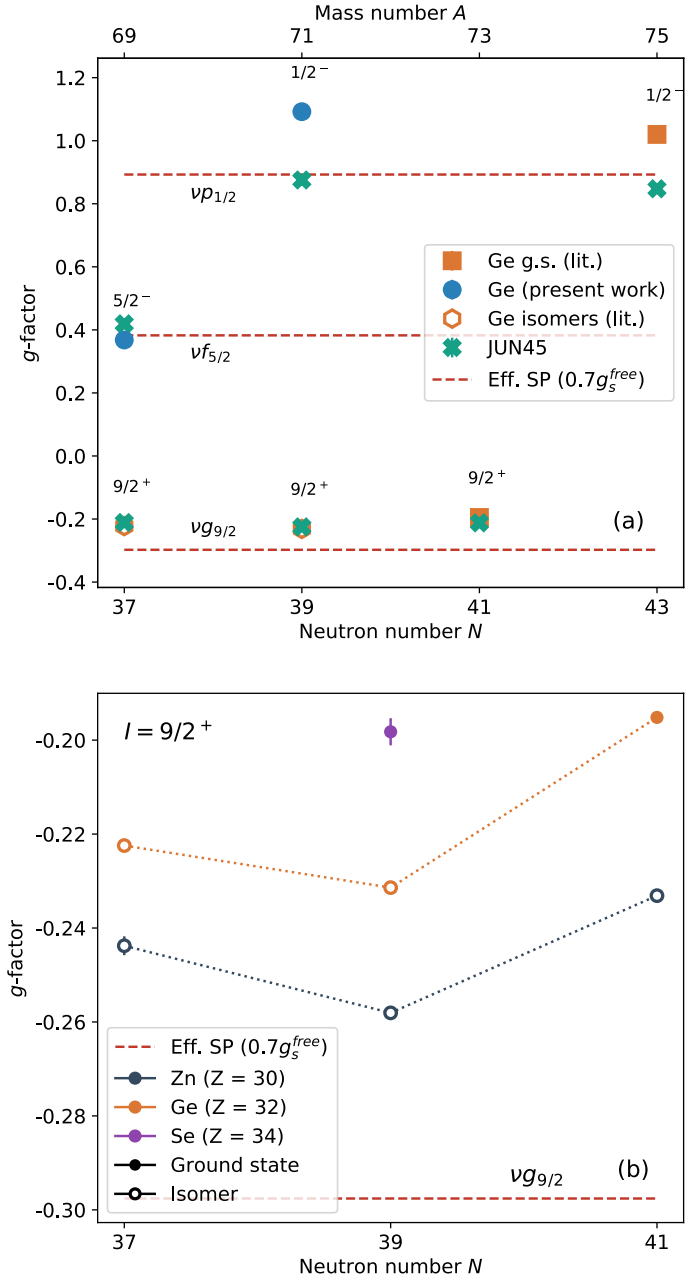

FIG. 7. (a) g-factor of ground and low-lying isomeric states of $^{67-75}$Ge, compared with the shell-model calculations using JUN45 interaction. (b) Experimental g-factors of ground and low-lying isomeric $9/2^+$ states of the isotones of even-Z, zinc, germanium and selenium isotopes.

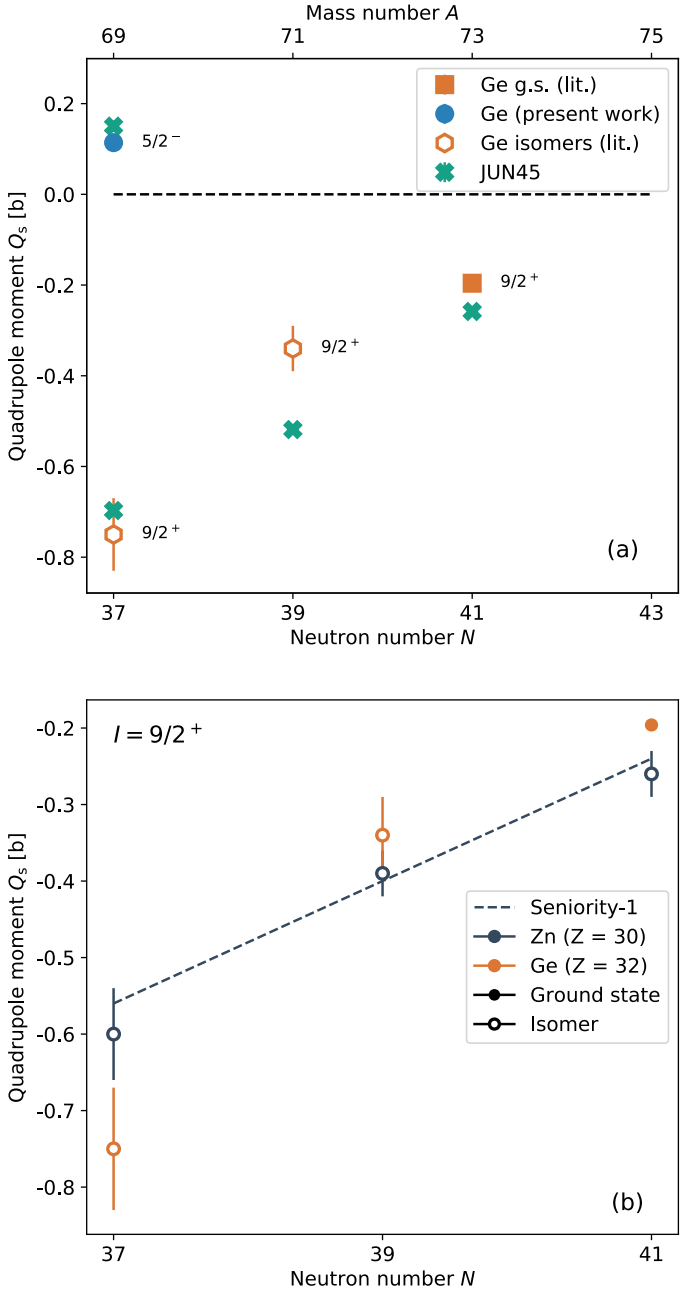

FIG. 8. (a) Quadrupole moments of ground and low-lying isomeric states of $^{67-75}$Ge, compared with the shell-model calculations using JUN45 interaction using effective charges $e_p^{\text{eff}} = 1.5e_p$ and $e_n^{\text{eff}} = 1.1e_n$. (b) Experimental quadrupole moments of ground and low-lying isomeric $9/2^+$ states of even-Z zinc, germanium and selenium.

ACKNOWLEDGMENTS

We acknowledge the support of the ISOLDE collaboration and technical teams. We would like to acknowledge the Center for Information Technology of the University of Groningen for their support and for providing access to the Peregrine high-performance computing cluster. This work was supported by the National Key R&D Program of China (No. 2018YFA0404403), the National Natural Science Foundation of China (No:11875073, U1967201); the BriX Research Program No. P7/12, FWO-Vlaanderen (Belgium), GOA 15/010 from KU Leuven; the UK Science and Technology Facilities Council grants ST/L005794/1 and ST/P004598/1; the NSF grant PHY-1068217, the BMBF Contracts No 05P18RDCIA, the Max-Planck Society, the Helmholtz International Center for FAIR (HIC for FAIR); the EU Horizon2020 research and innovation programme through ENSAR2 (No. 654002);

[1] O. Sorlin *et al.*, Phys. Rev. Lett. **88**, 092501 (2002).
[2] Z. Y. Xu *et al.*, Phys. Rev. Lett. **113**, 032505 (2014).
[3] M. L. Bissell *et al.*, Phys. Rev. C **93**, 064318 (2016).
[4] R. Taniuchi *et al.*, Nature **569**, 53 (2019).
[5] C. Wraith *et al.*, Phys. Lett. B **771**, 385 (2017).
[6] R. P. de Groote *et al.*, Phys. Rev. C **96**, 041302(R) (2017).
[7] L. Xie *et al.*, Phys. Lett. B **797**, 134805 (2019).
[8] B. Cheal *et al.*, Phys. Rev. Lett. **104**, 252502 (2010).
[9] N. Aoi *et al.*, Phys. Lett. B **692**, 302 (2010).

[10] C. J. Chiara *et al.*, Phys. Rev. C **84**, 037304 (2011).

[11] K. T. Flanagan *et al.*, Phys. Rev. Lett. **103**, 142501 (2009).

[12] B. Crider *et al.*, Phys. Lett. B **763**, 108 (2016).

[13] X. F. Yang *et al.*, Phys. Rev. C **97**, 044324 (2018).

[14] X. F. Yang *et al.*, Phys. Rev. Lett. **116**, 182502 (2016).

[15] P. Vingerhoets *et al.*, Phys. Rev. C **82**, 064311 (2010).

[16] T. J. Procter *et al.*, Phys. Rev. C **86**, 034329 (2012).

[17] S. Kaufmann *et al.*, Phys. Rev. Lett. **124**, 132502 (2020).

[18] R. P. de Groote *et al.*, Nat. Phys. **16**, 620 (2020).

[19] A. D. Ayangeakaa *et al.*, Phys. Lett. B **754**, 254 (2016).

[20] J. J. Sun *et al.*, Phys. Lett. B **734**, 308 (2014).

[21] Y. Toh *et al.*, Phys. Rev. C **87**, 041304(R) (2013).

[22] K. Heyde and J. L. Wood, Rev. Mod. Phys **83**, 1467 (2011).

[23] K. Heyde and J. L. Wood, Phys. Scr. **91**, 083008 (2016).

[24] A. F. Oluwole, S. G. Schmelling, and H. A. Shugart, Phys. Rev. C **2**, 228 (1970).

[25] R. Neugart *et al.*, J. Phys. G: Nucl. Part. Phys. **44**, 064002 (2017).

[26] E. Mané *et al.*, Eur. Phys. J. A **42**, 503 (2009).

[27] U. Köster *et al.*, Nuclear Instruments and Methods in Physics Research Section B: Beam Interactions with Materials and Atoms **204**, 303 (2003).

[28] A. Vernon *et al.*, Spectrochimica Acta Part B: Atomic Spectroscopy **153**, 61 (2019).

[29] K. Kreim *et al.*, Phys. Lett. B **731**, 97 (2014).

[30] S. Kaufmann *et al.*, J. Phys. Conf. Ser **599**, 012033 (2015).

[31] K. Abusaleem and B. Singh, Nucl. Data Sheets **112**, 133 (2011).

[32] B. Singh and J. Chen, Nucl. Data Sheets **158**, 1 (2019).

[33] M. L. Bissell and X. Yang, *Ground and isomeric state spins, moments and radii of Ge isotopes across the $N = 40$ subshell closure via laser spectroscopy*

at COLLAPS, Tech. Rep. CERN-INTC-2016-035. INTC-P-472 (CERN, Geneva, 2016).

[34] W. J. Childs and L. S. Goodman, Phys. Rev. **131**, 245 (1963).

[35] W. J. Childs and L. S. Goodman, Phys. Rev. **141**, 15 (1966).

[36] W. J. Childs and L. S. Goodman, Phys. Rev. C **1**, 750 (1970).

[37] W. Gins, R. de Groote, M. Bissell, C. Granados Buitrago, R. Ferrer, K. Lynch, G. Neyens, and S. Sels, Comput. Phys. Commun. **222**, 286 (2018).

[38] R. Neugart, S. L. Kaufman, W. Klempt, G. Moruzzi, E.-W. Otten, and B. Schinzler, in *Laser Spectroscopy III*, edited by J. L. Hall and J. L. Carlsten (Springer Berlin Heidelberg, Berlin, Heidelberg, 1977) pp. 446–447.

[39] N. Bendali, H. T. Duong, P. Juncar, J. M. S. Jalm, and J. L. Vialle, J. Phys. B: At. Mol. Phys. **19**, 233 (1986).

[40] W. Makulski, K. Jackowski, A. Antušek, and M. Jaszuński, J. Phys. Chem. A **110**, 11462 (2006).

[41] V. Kellö and A. Sadlej, Mol. Phys **96**, 275 (1999).

[42] U. Kaldor and E. Eliav, Adv. Quantum Chem. **31**, 313 (1998).

[43] L. Visscher, E. Eliav, and U. Kaldor, J. Chem. Phys **115**, 9720 (2001).

[44] A. Borschevsky, E. Eliav, and U. Kaldor, "High-accuracy relativistic coupled cluster calculations for the heaviest elements," in *Handbook of Relativistic Quantum Chemistry*, edited by W. Liu (Springer Berlin Heidelberg, 2016) pp. 825–855.

[45] A. Landau, E. Eliav, and U. Kaldor, in *New Perspectives in Quantum Systems in Chemistry and Physics, Part 1*, Advances in Quantum Chemistry, Vol. 39 (Academic Press, 2001) pp. 171 – 188.

[46] J. A. Pople, J. W. McIver, and N. S. Ostlund, J. Chem. Phys **49**, 2960 (1968).

[47] H. Yakobi, E. Eliav, L. Visscher, and U. Kaldor, J. Chem. Phys **126**, 054301

(2007).

[48] P. A. B. Haase, E. Eliav, M. Iliaš, and A. Borschevsky, J. Phys. Chem. A **124**, 3157 (2020).

[49] L. Visscher and K. G. Dyall, At. Data Nucl. Data Tables **67**, 207 (1997).

[50] "DIRAC, a relativistic ab initio electronic structure program, release DIRAC15," (2015), written by R. Bast, T. Saue, L. Visscher, and H. J. Aa. Jensen (see `http://www.diracprogram.org`).

[51] "DIRAC, a relativistic ab initio electronic structure program, release DIRAC17," (2017), written by L. Visscher, H. J. Aa. Jensen, R. Bast, and T. Saue (see `http://www.diracprogram.org`).

[52] K. G. Dyall, Theor. Chem. Acc **115**, 441 (2006).

[53] F. Gustafsson *et al.*, Accepted to Phys. Rev. A.

[54] W. Leo, *Techniques for Nuclear and Particle Physics Experiments: A How to Approach* (1987).

[55] E. Browne and J. Tuli, Nucl. Data Sheets **111**, 2425 (2010).

[56] H. Junde, H. Xiaolong, and J. Tuli, Nucl. Data Sheets **106**, 159 (2005).

[57] C. Nesaraja, Nucl. Data Sheets **115**, 1 (2014).

[58] T. Mertzimekis *et al.*, Nuclear Instruments and Methods in Physics Research A **807**, 56 (2016).

[59] M. Honma, T. Otsuka, T. Mizusaki, and M. Hjorth-Jensen, Phys. Rev. C **80**, 064323 (2009).

[60] G. J. Farooq-Smith *et al.*, Phys. Rev. C **96**, 044324 (2017).

[61] J. Eberz *et al.*, Nucl. Phys. A **464**, 9 (1987).

[62] S. Rahaman *et al.*, Eur. Phys. J. A **34**, 5 (2007).

[63] C. Guénaut *et al.*, Phys. Rev. C **75**, 044303 (2007).

[64] O. Perru *et al.*, Phys. Rev. Lett. **96**, 232501 (2006).

[65] C. Louchart *et al.*, Phys. Rev. C **87**, 054302 (2013).

6.1.1 Discussion on ^{69}Ge

In this publication, the hyperfine parameters of ^{69}Ge have been revised (and subsequently the nuclear moments), where the process and the reasons that lead to this revision are explained.

The older values have been acquired using the atomic-beam magnetic-resonance (ABMR) technique as described in Ref. [74]. This is a high-accuracy and sensitive experimental method. Using ABMR, transitions between the Zeeman levels of the hyperfine structure of an atomic state are being probed by resonant rf pulses. In the acquired spectra, a peak appears for every transition probed between the Zeeman hyperfine sublevels but assigning a wrong spin projection m_F to one of the two states of the transition will lead to a false hyperfine parameter result. This is the most probable source for the incorrect value of the hfs parameters of ^{69}Ge reported in Ref. [74].

While this might be the most common reason of false results in the ABMR technique, this does not exclude other sources of mistakes. Unfortunately, there is no reliable way to find the source of the problem in the results of 1970, but our analysis procedure give us all the necessary tools to unambiguously proceed with the revision of the hfs parameters of ^{69}Ge.

6.2 Charge radii of germanium isotopes

Using the analysis procedure and results presented in Ch. 5 for $^{68-74}$Ge, the isotope shifts of these isotopes is being summarised in Fig. 6.1(a) and Tab. 6.2.

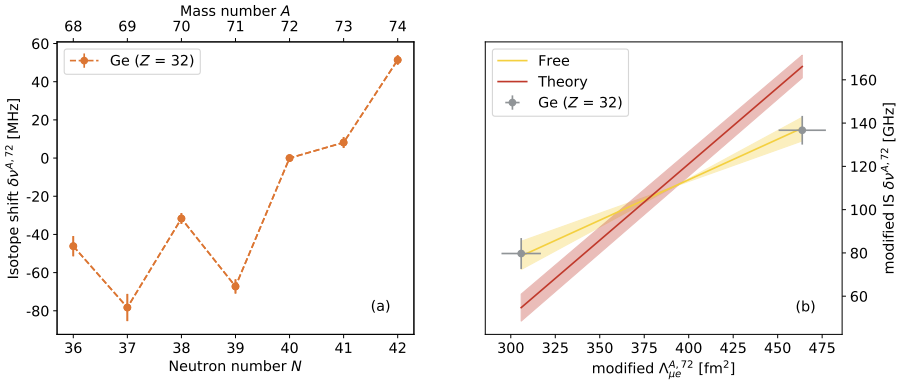

Figure 6.1: (a) Isotope shifts of $^{68-74}$Ge for the $4s^2 4p^2\,{}^3P_1 - 4s^2 4p 5s\,{}^3P_1^o$ (269 nm) atomic transition. The reference isotope is ^{72}Ge and the analysis procedure is described in Ch. 5. (b) King plot for the isotopes of germanium in the $4s^2 4p^2\,{}^3P_1 - 4s^2 4p 5s\,{}^3P_1^o$ (269 nm) atomic transition. The isotopes shifts $\delta\nu^{A,72}$ of ^{70,74}Ge were used against the nuclear charge parameters $\Lambda_{\mu e}^{A,72}$ taken from Ref. [23].

In order to extract the differences in the mean square charge radii $\delta\langle r^2\rangle$ from the isotope shifts the King plot method is employed as discussed in Ch. 2. To construct the King plot the isotopes shifts $\delta\nu^{A,72}$ extracted from the experimental data are plotted against the nuclear radius parameters $\Lambda_{\mu e}^{A,72}$, as defined in 2.49. The nuclear radius parameter $\Lambda_{\mu e}^{A,72}$ for germanium can be found in Ref. [23]. In order to perform this fit (with only two points) a Markov chain Monte Carlo (MCMC) random walk fit was performed [98]. Following the process presented in Sec. 2.4.2, the extracted field shift F and mass shift M can be seen in Tab. 6.1 while the King plot is presented in Fig. 6.1(b).

At the same time, the field shift F was also calculated for the $4s^2 4p^2\,{}^3P_1 - 4s^2 4p 5s\,{}^3P_1^o$ (269 nm) atomic transition of germanium using

the multireference relativistic FSCC method presented in Ref. [3]. The FSCC calculation result ($F_{\text{th}} = 706(6)$ MHz/fm^2) is not in agreement with the MCMC fit results from the King plot, as it can been seen by the red line in Fig. 6.1(b). For that reason, despite having only two points, it was decided to use the MCMC fit results for the field and mass shift.

Table 6.1: Field shift F and mass shift M for the $4s^2 4p^2\,{}^3P_1 - 4s^2 4p5s\,{}^3P_1^o$ (269 nm) atomic transition of germanium obtained using a MCMC fit from the King plot method.

Field shift F (MHz/fm^2)	Mass shift M (GHz)
+374(81)	-36(31)

Using the values of Tab. 6.1 for the field and the mass shift, the differences in the mean square charge radii $\delta\langle r^2\rangle^{A,72}$ were extracted, presented in Tab.6.2 and in Fig. 6.2(a). In Fig. 6.3 the differences of the mean square charge radii of relevant isotopic chains in the region are presented, along germanium. The trend between the differences in the charge radii of the germanium chain and the other isotopic chains in the region is in good agreement, strengthening the validity of the King plot results of F and M.

The differences in the mean square charge radii $\delta\langle r^2\rangle$ already contain all the necessary physics information but in some cases it is needed (or wanted) to extract the absolute values of root mean square charge radii $\langle r^2\rangle^{1/2}$. In order to do that, a reference value of a root mean square charge radius is needed and usually many different are available. In the context of this thesis the model dependent RMS charge radius of ^{72}Ge [23] was the choice of preference, leading to the mean square charge radii in Tab.6.2 and in Fig. 6.2(b).

No clear observations can be made from Fig. 6.2 but there are hints of the presence of interesting effects. In order to look into more detail to the odd-even staggering or a possible effect of the $N = 40$ subshell, the droplet model was employed as presented in Sec. 2.2.4. The mean square charge radii using the droplet model were calculated for the isotopic chains of copper ($Z = 29$), zinc ($Z = 30$), gallium ($Z = 31$) and germanium ($Z = 32$). In first order approximation, a simple spherical shape is assumed and thus all Legendre polynomials higher than second order

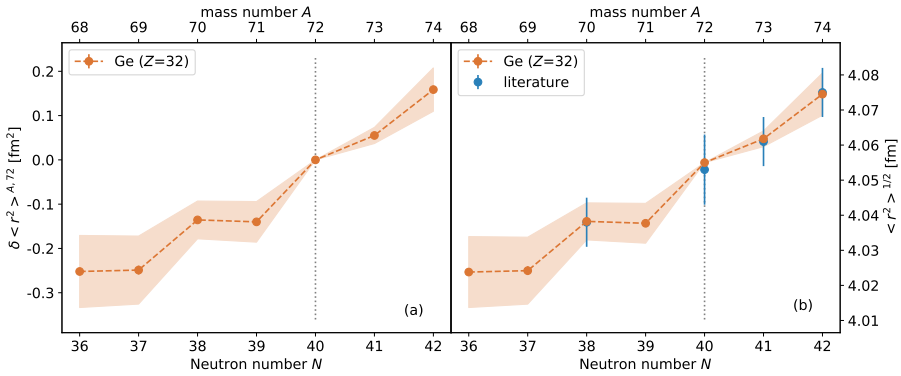

Figure 6.2: (a) Difference in the mean square charge radii and (b) root mean square charge radii for $^{68-74}$Ge compared with literature values from Ref. [23].

are equal to zero [32]. At the same time, the mean square charge radii of these isotopic chains were calculated from their respective differences in mean square charge radii [32, 50, 51]. The reference values for each chain were chosen to be the model dependent RMS charge radius found in Ref. [23], in favour of consistency.

The difference between the experimental mean square charge radii and the droplet model values $\delta\langle r^2\rangle_{\text{exp, DLM}}$ is presented in Fig. 6.4(a). By increasing the proton number Z, an increasing departure from zero is

Table 6.2: Isotope shifts, difference in mean square charge radii and the root mean square charge radii for $^{68-74}$Ge.

Isotope	$\delta\nu^{A,72}$ (MHz)	$\delta\langle r^2\rangle^{A,72}$ (fm)	$\langle r^2\rangle^{1/2}$ (fm)
^{68}Ge	-46(5)	-0.202(14)[81]	4.0238(9)[101]
^{69}Ge	-78(7)	-0.267(19)[77]	4.0242(13)[95]
^{70}Ge	-32(3)	-0.123(8)[43]	4.0382(5)[53]
^{71}Ge	-67(4)	-0.198(10)[46]	4.0377(7)[57]
^{72}Ge	0	0	4.055(0)[0]
^{73}Ge	+8(3)	+0.040(8)[18]	4.0618(5)[22]
^{74}Ge	+51(2)	+0.173(7)[49]	4.0745(4)[60]

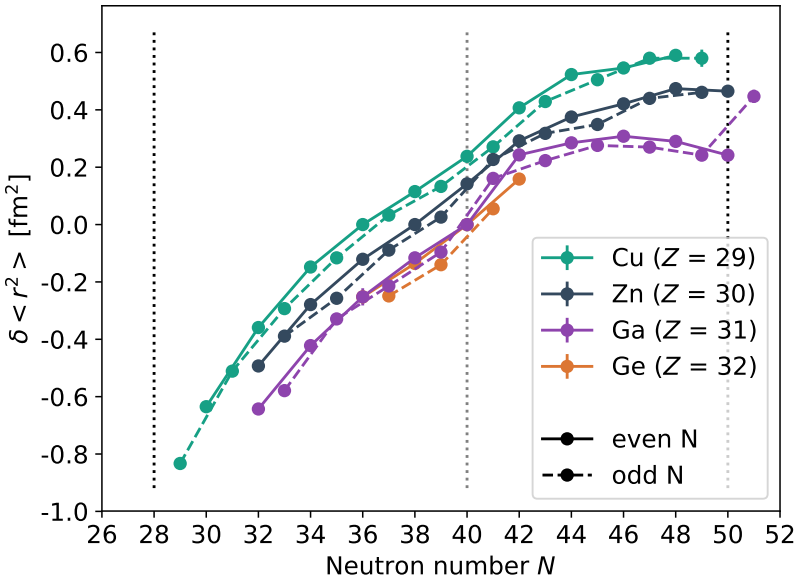

Figure 6.3: Difference in the mean square charge radii of the copper ($Z = 29$), zinc ($Z = 30$), gallium ($Z = 31$) and germanium ($Z = 32$) isotopic chains as given in Refs. [32, 50, 51]. No offset between the chains is included.

observed for each isotopic chain, indicating the increased collectivity of these nuclear systems going from copper to germanium. This departure gets its highest value around $N = 34$-36 while at $N = 40$ a dip is seen. At the same time, a kink is present at $N = 40$ on all the isotopic chains (including germanium). These two observations indicate the existence of the weak subshell effect (closure) at $N = 40$ that has been previously observed in the region [32, 50].

One more observation from Fig. 6.4(a) is the existence of odd-even staggering effect. The staggering parameter defined in Eq. 2.32 was calculated [49], in order to study the OES effect further.

The staggering parameters D of the copper ($Z = 29$), zinc ($Z = 30$), gallium ($Z = 31$) and germanium ($Z = 32$) isotopic chains are presented in Fig. 6.4(b)-(e). As expected, the OES effect is present throughout all

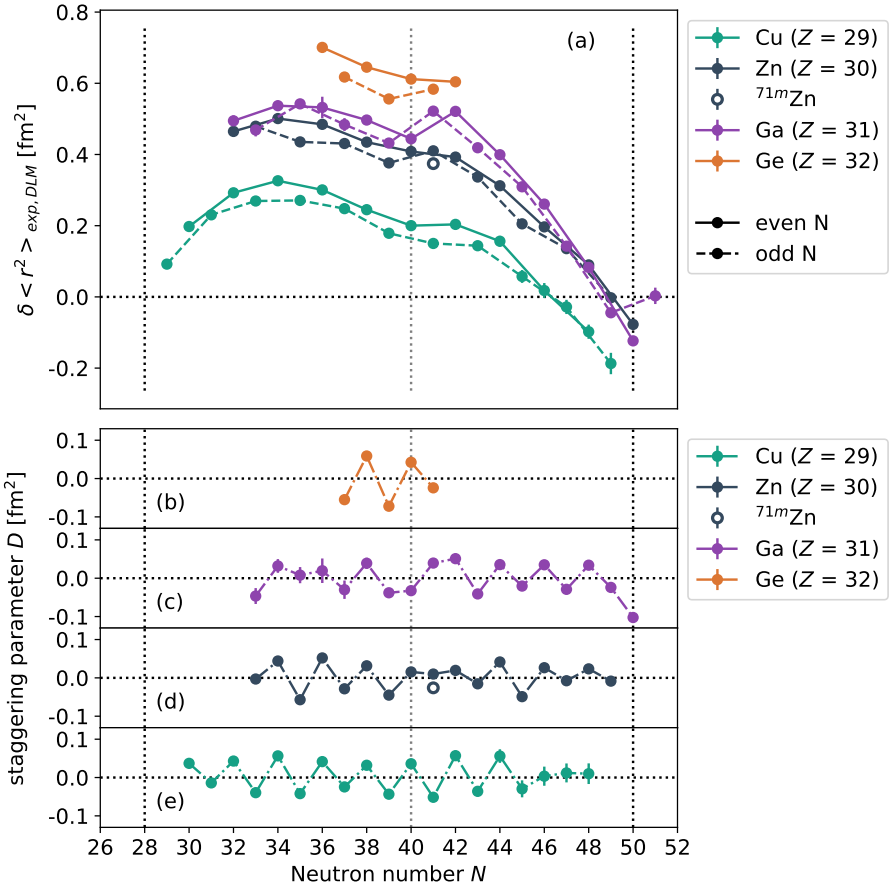

Figure 6.4: (a) Difference between experimental mean square charge radii and the droplet model values. (b)-(e) Staggering parameters for the isotopic chains in the region of nickel.

the isotopic chains but what is interesting to observe is the inverted OES present at $N = 41$ for zinc ($Z = 30$) and more strongly for gallium ($Z = 31$) (seen in Fig. 6.4(d) & (c) respectively). The presence of the inverted odd-even staggering effect in ^{71}Zn could point to a change in the single particle shell structure. For example, the single neutron sitting in the $\nu p_{1/2}$ that is dominating the wavefunction of this ground state [37]. In a simple shell model picture this single neutron would be expected to

sit in the $\nu g_{9/2}$ orbit, something that instead is happening for the first excited (and isomer) of ^{71}Zn. This "inversion" of the expected ground and isomeric state is the source of the observed inverted OES in ^{71}Zn, as can be seen in Fig. 6.4(d) where the staggering parameter of ^{71m}Zn is presented [50]. On the other hand, in order to reproduce the negative parity state, $I^{\pi} = 3^{-}$, of the ^{72}Ga g.s., in the $f_{5/2}pg_{9/2}$ valence space, the neutron should occupy the $\nu g_{9/2}$ orbit, while the proton presents a highly mixed configuration between the $\pi p_{3/2}$ and the $\pi f_{5/2}$ orbits [41, 6]. This collective behaviour of ^{72}Ga leads to the appearance of the inverted OES effect in this system. At $N = 42$, 43, the normal OES is restored. For the isotopic chain of germanium ($Z = 32$), the normal OES effect is observed for all isotopes, up to $N = 41$, and from the spin and moments the normal filling of the neutron orbitals is indeed confirmed.

As a conclusion, from the combined analysis of the moments, spins and radii in the isotopes from copper to germanium, it is clear that irregularities in the OES of the charge radii are an indication for a change in the underlying single particle nature of the wave function, which deviates from the expected "normal" shell model filling of the orbits.

Chapter 7

Conclusions & Outlook

In this thesis, the study of the nuclear structure of the germanium isotopes $^{68-74}$Ge near stability via collinear laser spectroscopy at the COLLLAPS setup of ISOLDE-CERN, is presented. These isotopes are located in the $N = 40$ region of the chart of nuclides that is famous for various nuclear structure evolution effects taking place. The nuclear magnetic dipole and spectroscopic electric quadrupole moments and differences in the mean square charge radii of these isotopes were determined.

The necessary development of a frequency mixing unit in the laser lab of COLLAPS is presented in order to produce the required light wavelength for these studies. A study of the systematics of the voltage multimeters is presented, as well, in order to determine the reliability of each multimeter device.

During the analysis process, a discrepancy in the nuclear moments of ^{69}Ge was observed. Through careful analysis of the hfs of the odd-A isotopes and with the help of FSCC atomic calculation of the hyperfine fields, a revision of the magnetic and quadrupole moments was performed.

Germanium isotopes with $Z = 32$, having five stable isotopes around the $N = 40$ provide an excellent case to study the nuclear evolution phenomena in the nickel region, such as the emergence of a weak subshell effect at $N = 40$ and collective effects around it, the origin of the appearance of the inverted odd-even staggering effect and deformation

and shape coexistence.

Comparing the experimental g-factors of the ground states of ^{69,71,73}Ge acquired from this work and the g-factors of the isomers of germanium in literature with the effective single-particle g-factors reveal the dominant configuration of the single unpaired neutron. Comparison with a large-scale shell-model calculation with the use of the JUN45 effective interaction provides a good agreement for all observed g-factors of long-lived states with spin different from 1/2, while for the spin 1/2 states the theory systematically deviates from the data. A comparison with the dipole moments of the isotones of germanium in the region reveal an increase in the collectivity when adding protons to the $Z = 28$.

Through comparison of the experimental quadrupole moments of the ^{69,71,73}Ge acquired from this work and those of the isomers of germanium in literature, a linear trend is observed in the quadrupole moments of these 9/2+ states, when neutrons fill the $\nu g_{9/2}$ orbital. This trend has also been observed in the neighbouring zinc chain and has been associated with a seniority-1$(\nu g_{9/2})^n$ configuration with the increased neutron number.

Though a comparison of the mean-square charge radii of germanium isotopes with the droplet model, a hint of a kink is observed when crossing the $N = 40$ revealing the presence of a weak sub-shell effect in the germanium chain as well. Comparing the difference between experimental values and the droplet model charge radii for germanium and other relevant chains in the region, the same increase in collectivity is revealed in the germanium chain with the addition of protons on the $Z = 28$ as observed in the moments. A comparison between the staggering parameters reveal the presence of normal OES effect when approaching and crossing the $N = 40$ in the germanium chain.

It is clear that germanium isotopes near $N = 40$ present collective effects but more input is needed to shed further light on the physics of the region. Measuring the $9/2^+$ isomers of ^{69,71}Ge, in a systematic and single dataset, and extend the study beyond $N = 40$ up to $N = 50$ and even beyond, will yield the necessary information to understand the structural evolution phenomena. There is already a reliable atomic transition that can be used but developments are in need, in order to combat the increasing beam

contamination in the heavier isotopes, in case a ZrO_2 target is used again, that reaches the experimental setup and increases the scattered laser light and thus, the measurement background photons. Additionally, a study on the isotopic chain of arsenic ($Z = 33$) and selenium ($Z = 34$) will help to breach two regions well known for structural evolution phenomena, the nickel-copper region with the krypton-rubidium region. Extending this study to heavier systems and towards the $N = 50$ could provide all the essential information to understand the nuclear phenomena that are present in $28 \leq N, Z, \leq 50$.

Appendix A

Files and file contents

On the tables included in this appendix, the information about the contents of the analysed files are included for all different isotopes. Below the abbreviations used in the table are explained.

file : run number of the file

go : number of subsequent runs included in the file

scans : number of scans per go

steps : number of steps per scan

scan range : scanning voltage range in V

step : voltage step in V

A : accumulation time of ISCOOL in ms

BG : beam Gate open time in ms

ISCOOL : platform voltage of ISCOOL in V

fluke : fluke voltage in V

Table A.1: Information of file contents for ^{72}Ge

file	go	scans	steps	scan range (V)	step (V)	A/BG (ms)	ISCOOL (V)	fluke (V)
118	1	100	251	-8.5→-5.5	0.01	1/9	49769.7	200.20
184	1	100	173	-7.5→-5.5	0.01	5/49	49768.9	200.18
197	1	100	173	-7.5→-5.5	0.01	5/4.9	49769.1	200.26
198	1	100	173	-7.5→-5.5	0.01	5/4.9	49769.1	200.26
204	1	100	173	-7.5→-5.5	0.01	5/4.9	49769.2	200.17
205	1	100	173	-7.5→-5.5	0.01	5/4.9	49769.2	200.17
211	1	100	173	-7.5→-5.5	0.01	5/4.9	49769.2	200.18
212	1	100	173	-7.5→-5.5	0.01	5/4.9	49769.3	200.18
216	1	100	173	-7.5→-5.5	0.01	5/4.9	49769.3	199.98
217	1	100	173	-7.5→-5.5	0.01	5/4.9	49769.3	199.98
230	1	100	173	-7.5→-5.5	0.01	5/4.9	49769.2	199.98
252	1	100	173	-7.5→-5.5	0.01	5/4.9	49769.3	200.37
259	2	100	173	-7.5→-5.5	0.01	5/4.9	49769.2	200.37
287	2	100	173	-7.5→-5.5	0.01	5/4.9	49769.2	200.27
294	2	100	173	-7.5→-5.5	0.01	5/4.9	49769.4	200.26
327	1	200	173	-7.5→-5.5	0.01	5/4.9	49770.2	200.13
333	1	200	173	-7.5→-5.5	0.01	5/4.9	49770.1	200.20
339	1	200	173	-7.5→-5.5	0.01	5/4.9	49770.0	200.20
340	1	200	173	-7.5→-5.5	0.01	5/4.9	49770.1	200.20
346	1	200	173	-7.5→-5.5	0.01	5/4.9	49769.8	200.11
351	1	200	173	-7.5→-5.5	0.01	5/4.9	49769.8	200.11
352	1	200	173	-7.5→-5.5	0.01	5/4.9	49769.8	200.11
355	1	200	173	-7.5→-5.5	0.01	5/4.9	49769.6	200.11
358	1	200	173	-7.5→-5.5	0.01	5/4.9	49769.6	200.11
359	1	200	173	-7.5→-5.5	0.01	5/4.9	49769.6	200.11
365	1	200	173	-7.5→-5.5	0.01	5/4.9	49769.5	199.98

Table A.2: Information of file contents for ^{68}Ge

file	go	scans	steps	scan range (V)	step (V)	A/BG (ms)	ISCOOL (V)	fluke (V)
223	4	100	117	-5.0→-3.6	0.01	5/2	49769.3	2851.10
229	6	100	117	-5.0→-3.6	0.01	5/1	49769.3	2851.10
348	2	500	117	-5.0→-3.6	0.01	5/1	49769.8	2851.13
360	1	500	117	-5.0→-3.6	0.01	5/1	49770.5	2857.65
364	4	500	117	-5.0→-3.6	0.01	5/1	49770.5	2857.64

Table A.3: Information of file contents for ^{70}Ge

file	go	scans	steps	scan range (V)	step (V)	A/BG (ms)	ISCOOL (V)	fluke (V)
253	1	1000	209	-6.5→-4.0	0.01	5/1	49769.2	1495.74
256	3	1000	209	-6.5→-4.0	0.01	5/1	49769.2	1495.73
330	1	1000	209	-6.5→-4.0	0.01	5/2	49770.2	1486.14
338	1	1000	209	-6.5→-4.0	0.01	5/2	49770.1	1495.56
349	1	1000	209	-6.5→-4.0	0.01	5/2	49769.9	1495.58
356	1	1000	209	-6.5→-4.0	0.01	5/2	49769.6	1482.04
357	1	1000	209	-6.5→-4.0	0.01	5/2	49769.5	1482.03

Table A.4: Information of file contents for ^{74}Ge

file	go	scans	steps	scan range (V)	step (V)	A/BG (ms)	ISCOOL (V)	fluke (V)
191	4	167	200	-6.0→-4.0	0.01	5/4.9	49769.0	-1279.43
195	4	167	200	-6.0→-4.0	0.01	8/7.9	49769.1	-1279.43

Table A.5: Information of file contents for ^{73}Ge

file	go	scans	steps	scan range (V)	step (V)	A/BG (ms)	ISCOOL (V)	fluke (V)
122/118	3	100	752	-7.5→1.5	0.01	10/9	49769.6	-592.39
207/205	1	100	485	-7.5→-1.7	0.01	10/9	49769.2	-591.33
210/211	3	100	485	-7.5→-1.7	0.01	10/9	49769.2	-591.32
343/340	2	1000	485	-7.5→-1.7	0.01	5/4	49769.9	-597.02

Table A.6: Information of file contents for ^{71}Ge

file	go	scans	steps	scan range (V)	step (V)	A/BG (ms)	ISCOOL (V)	fluke (V)
200/198	2	100	501	-8.0→-2.0	0.01	7/6.9	49769.1	786.04
202/204	2	100	501	-8.0→-2.0	0.01	7/6.9	49769.1	786.05
290/287	2	100	794	-8.5→1.0	0.01	20/19	49769.3	786.05
292/294	2	100	794	-8.5→1.0	0.01	20/19	49769.3	786.05

Table A.7: Information of file contents for ^{69}Ge

file	go	scans	steps	scan range (V)	step (V)	A/BG (ms)	ISCOOL (V)	fluke (V)
214/212	1	500	584	-8.5→-1.5	0.01	5/4	49769.3	2163.89
215/216	1	500	584	-8.5→-1.5	0.01	5/4	49769.2	2163.79
337/333	1	1500	501	-8.0→-2.0	0.01	5/2	49770.1	2170.02
353/352	1	1500	501	-8.0→-2.0	0.01	5/4	49769.7	2163.27

Appendix B

Hfs constants and CoG fitting results

In this appendix, the fitting results for the centre of gravity for every file is presented, grouped per isotope. The file number and the corresponding reference file number is presented. The isotope shift for every file-reference file set is calculated along the weighted mean for every isotope. Below the abbreviations used in the table are explained.

file : run number of the file

ref. : run number of the reference file

CoG : centre of gravity

ref. CoG : centre of gravity of the corresponding reference file

IS : isotope shift

fixed to lit. : as described in Ch. 5, the hfs constants are fixed to the literature values and free hfs peak intensities

free : as described in Ch. 5, the hfs constants are not constrained and free hfs peak intensities

free & Racah int. : as described in Ch. 5, the hfs constants are not constrained and the hfs peak intensities are fixed to the Racah values

Table B.1: CoG results for ^{72}Ge

file	CoG (MHZ)
118	-946(3)
184	-950(2)
197	-947(2)
198	-971(2)
204	-965(2)
205	-967(2)
211	-963(2)
212	-971(2)
216	-935(3)
217	-948(3)
230	-932(3)
252	-963(3)
259	-909(2)
287	-966(3)
294	-944(3)
327	-1005.7(11)
333	-1004.1(10)
339	-1002.8(14)
340	-1003.6(15)
346	-998.9(17)
351	-1003.6(17)
352	-1000.5(16)
355	-1000.0(17)
358	-998.1(18)
359	-1000.9(17)
365	-1003.2(16)

Table B.2: CoG and IS results for ^{68}Ge

file/ref.	ref. CoG (MHz)	CoG (MHz)	IS (MHz)
223/217	-948(3)	-976(6)	-28(7)
229/230	-932(3)	-975(5)	-43(5)
348/346	-998.9(17)	-1057(9)	-58(9)
360/359	-1000.9(17)	-1060(8)	-59(8)
364/365	-1003.2(16)	-1054(6)	-51(6)
total			-46(5)

Table B.3: CoG and IS results for ^{70}Ge

file/ref.	ref. CoG (MHz)	CoG (MHz)	IS (MHz)
253/252	-963(3)	-993(11)	-31(11)
256/259	-909(2)	-934(6)	-26(7)
330/327	-1005.7(11)	-1035(4)	-29(4)
338/339	-1002.8(14)	-1036(6)	-33(6)
349/351	-1003.6(17)	-1022(6)	-18(6)
356/355	-1000.0(17)	-1038(5)	-38(5)
357/358	-998.1(18)	-1040(6)	-42(6)
total			-32(3)

Table B.4: CoG and IS results for ^{74}Ge

file/ref.	ref. CoG (MHz)	CoG (MHz)	IS (MHz)
191/184	-950(2)	-898(3)	+52(4)
195/197	-947(2)	-896(3)	+51(3)
total			+51(2)

Table B.5: CoG and IS results for ^{73}Ge

file/ref.	ref. CoG	fixed to lit.		free		free & Racah int.	
		CoG (MHz)	IS (MHz)	CoG (MHz)	IS (MHz)	CoG (MHz)	IS (MHz)
122/118	-946(3)	-937(5)	+9(6)	-940(4)	+7(5)	-933(2)	+13(4)
207/205	-967(2)	-962(6)	+5(6)	-965(5)	+2(5)	-958(4)	+8(5)
210/211	-963(2)	-953(5)	+10(5)	-956(4)	+6(4)	-949(3)	+13(3)
342/340	-1003.6(15)	-996(5)	+8(5)	-999(4)	+5(4)	-993(3)	+11(3)
total			+8(3)		+5(2)		+12(2)

Table B.6: CoG and IS results for ^{71}Ge

file/ref.	ref. CoG	fixed to lit.		free		free & Racah int.	
		CoG (MHz)	IS (MHz)	CoG (MHz)	IS (MHz)	CoG (MHz)	IS (MHz)
200/198	-971(2)	-1038.1(15)	-67(3)	-1037.5(15)	-67(3)	-1039.2(15)	-68(3)
202/204	-965(2)	-1037.7(17)	-73(3)	-1037.1(18)	-72(3)	-1039.7(17)	-75(3)
290/287	-966(3)	-1035(2)	-68(4)	-1034(2)	-68(4)	-1037(3)	-70(4)
292/294	-944(3)	-996(3)	-53(4)	-996(3)	-53(4)	-998(5)	-54(6)
total			-67(4)		-67(4)		-70(3)

Table B.7: CoG and IS results for ^{69}Ge

file/ref.	ref. CoG	fixed to lit.		free		free & Racah int.	
		CoG (MHz)	IS (MHz)	CoG (MHz)	IS (MHz)	CoG (MHz)	IS (MHz)
214/212	-971(2)	-1044(3)	-73(4)	-1041(3)	-70(4)	-1046(3)	-75(4)
215/216	-935(3)	-1038(3)	-103(4)	-1038(3)	-102(4)	-1042(3)	-106(4)
337/333	-1004.1(10)	-1084(3)	-80(3)	-1081(3)	-77(3)	-1085(2)	-81(3)
353/352	-1000.5(16)	-1072(3)	-71(4)	-1070(3)	-69(3)	-1075(3)	-74(3)
total			-81(7)		-78(7)		-83(7)

Appendix C

Fitting input and other fitting results

In this appendix, the rest of the result are presented. Below the abbreviations used in the table are explained.

file : run number of the file

ToF Gate : time-of-flight gate in μs used to gate the hfs spectra

FWHMG : gaussian Full-Width at Half Maximum of the voigt line shape

background : hfs background

scale : For the even-A cases, scale represents the height of the peak since in these spectra there is only one peak. For the odd-A cases, since the transition rates are free parameters, scale is a fixed value and the amplitudes are the fittable parameters that are used to much the height of the peaks.

Table C.1: Other results for ^{72}Ge

file	ToF Gate (μs)	FWHMG (MHz)	background (cts)	scale
118	51.2→58.7	63(13)	840(2)	256(15)
184	52.3→56.6	96(8)	87.6(10)	171(6)
197	52.3→56.7	59(8)	76.0(9)	214(7)
198	52.3→56.3	79(8)	72.5(9)	178(6)
204	52.3→56.2	72(8)	58.1(8)	159(6)
205	52.3→56.4	73(8)	59.7(8)	155(6)
211	52.4→56.2	56(9)	51.5(7)	149(6)
212	52.3→56.2	60(9)	50.4(7)	148(6)
216	52.3→56.2	83(9)	40.8(7)	108(5)
217	52.3→56.2	68(10)	37.3(6)	95(5)
230	52.3→56.7	70(10)	53.8(7)	105(5)
252	52.3→56.4	41(13)	47.0(7)	98(6)
259	52.3→56.5	59(9)	80.5(9)	170(7)
287	52.3→56.5	63(11)	70.5(8)	107(6)
294	52.3→56.2	79(10)	67.6(8)	116(5)
327	51.6→57.6	50(6)	207.0(15)	523(12)
333	51.6→57.6	28(9)	192.7(14)	507(14)
339	51.6→57.6	26(11)	169.5(13)	313(11)
340	51.6→57.6	35(9)	167.1(13)	310(11)
346	51.6→57.3	33(11)	142.1(12)	239(10)
351	51.6→57.4	29(12)	128.1(11)	215(10)
352	51.6→57.6	20(16)	178.3(13)	276(12)
355	51.6→57.2	29(12)	161.1(12)	242(10)
358	51.6→57.4	44(10)	173.1(13)	236(10)
359	51.6→57.6	22(15)	175.7(13)	248(11)
365	51.6→57.6	23(14)	175.0(13)	270(11)

Table C.2: Other results for ^{68}Ge

file	ToF Gate (μs)	FWHMG (MHz)	background (cts)	scale
223	49.4→56.5	56(27)	405(3)	89(11)
229	49.4→56.5	2(39)	487(3)	121(13)
348	49.4→56.5	78(32)	1033(4)	106(15)
360	49.4→56.5	1(96)	644(3)	84(17)
364	49.4→56.5	57(25)	2546(6)	227(26)

Table C.3: Other results for ^{70}Ge

file	ToF Gate (μs)	FWHMG (MHz)	background (cts)	scale
253	51.3→56.8	126(34)	7848(9)	307(38)
256	51.3→56.8	71(24)	15320(12)	618(65)
330	50.2→58.7	33(24)	26717(16)	1142(104)
338	50.2→58.7	53(24)	23644(15)	819(88)
349	50.2→58.7	15(23)	18316(13)	599(75)
356	50.5→57.9	29(30)	15007(12)	733(80)
357	50.5→57.9	49(24)	14997(12)	678(72)

Table C.4: Other results for ^{74}Ge

file	ToF Gate (μs)	FWHMG (MHz)	background (cts)	scale
191	52.2→58.2	47(15)	324.1(19)	185(11)
195	52.2→58.2	57(13)	327.3(19)	198(11)

Table C.5: Other results for ^{73}Ge

file	ToF Gate (μs)	FWHMG (MHz)	background (cts)	scale (fixed)
122	51.6→58.0	39(11)	166.8(6)	81
207	52.3→57.0	30(19)	34.3(3)	20
210	52.3→57.0	35(13)	100.4(6)	52
343	52.3→57.0	15(25)	717.2(15)	117

Table C.6: Other results for ^{71}Ge

file	ToF Gate (μs)	FWHMG (MHz)	background (cts)	scale (fixed)
200	52.0→56.0	57(5)	113.6(6)	342
202	52.0→56.0	64(5)	104.2(6)	278
290	51.5→56.6	25(10)	82.5(4)	126
292	51.5→56.6	31(10)	81.3(4)	99

Table C.7: Other results for ^{69}Ge

file	ToF Gate (μs)	FWHMG (MHz)	background (cts)	scale (fixed)
214/212	50.1→56.0	64(9)	419.6(11)	264
215/216	50.1→56.0	23(14)	416.3(11)	285
337/333	49.3→57.9	48(9)	2119(3)	663
353/352	50.1→56.0	1(15)	1803(2)	578

Table C.8: HFS normalised transition amplitudes for ^{73}Ge

7/2→7/2	7/2→9/2	9/2→7/2	9/2→9/2	9/2→11/2	11/2→9/2	11/2→11/2
0.8(6)	1.1(9)	1.1(9)	0.03(3)	1.7(15)	1.2(10)	1

Table C.9: HFS normalised transition amplitudes for ^{71}Ge

1/2→1/2	1/2→3/2	3/2→1/2	3/2→3/2
0.464(19)	0.40(2)	0.399(18)	1

Table C.10: HFS normalised transition amplitudes for ^{69}Ge

3/2→3/2	3/2→5/2	5/2→3/2	5/2→5/2	5/2→7/2	7/2→5/2	7/2→7/2
0.45(5)	0.56(5)	0.58(6)	0.22(6)	0.85(10)	0.78(8)	1

Appendix D

Correlation plot of King plot analysis

In this appendix, the correlation plot of the Markov chain Monte Carlo (MCMC) random walk fit performed for the King plot analysis is presented. The King plot can be seen in 6.1(b) where the random walk fit is presented by the yellow line.

We can see that there is a clear negative strong correlation between the two variables, i.e. the field and the mass shift. For this fit, it is attempted to fit a straight line through two points leads to the strong correlation that it is observed in D.1.

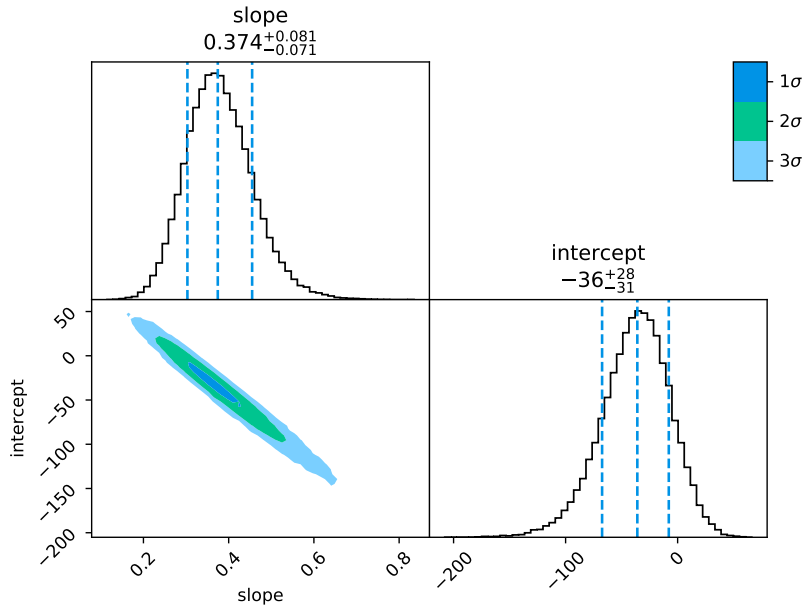

Figure D.1: Correlation plot of the MCMC random walk fit performed for the King plot analysis.

Bibliography

[1] Maria Goeppert Mayer. On closed shells in nuclei. ii. *Phys. Rev.*, 75:1969–1970, Jun 1949.

[2] M. Honma, T. Otsuka, T. Mizusaki, and M. Hjorth-Jensen. *Physical Review C*, 80(6):064323, dec 2009.

[3] A. Kanellakopoulos, X. F. Yang, M. L. Bissell, M. L. Reitsma, et al. *Phys. Rev. C*, 102:054331, Nov 2020.

[4] Fundamental physics constants, may 2019.

[5] X. F. Yang, C. Wraith, L. Xie, et al. *Physical Review Letters*, 116(18):182502, may 2016.

[6] G. J. Farooq-Smith, A. R. Vernon, et al. *Physical Review C*, 96(4):044324, oct 2017.

[7] B. Castel, P.P.B. Castel, I.S. Towner, and T.P.B.I.S. Towner. *Modern Theories of Nuclear Moments*. Oxford science publications. Clarendon Press, 1990.

[8] William D Myers and W.J Swiatecki. *Annals of Physics*, 55(3):395–505, dec 1969.

[9] William D. Myers and Karl-Heinz Schmidt. *Nuclear Physics A*, 410(1):61–73, nov 1983.

[10] William D. Myers. *Atomic Data and Nuclear Data Tables*, 17(5-6):411–417, may 1976.

[11] D. Berdichevsky and F. Tondeur. *Zeitschrift für Physik A Atoms and Nucleir Physik A Atoms and Nuclei*, 322(1):141–147, mar 1985.

[12] *Atomic Data and Nuclear Data Tables*, 99(1):69–95, jan 2013.

[13] Mihai Horoi. *Physical Review C*, 50(6):2834–2840, dec 1994.

[14] Richard A. Uher and Raymond A. Sorensen. *Nuclear Physics*, 86(1):1–46, 1966.

[15] Balbir S. Reehal and Raymond A. Sorensen. *Nuclear Physics A*, 161(2):385–400, 1971.

[16] R. Neugart and G. Neyens. *Nuclear Moments*, pages 135–189. Springer Berlin Heidelberg, Berlin, Heidelberg, 2006.

[17] E. C. Seltzer. *Physical Review*, 188(4):1916–1919, dec 1969.

[18] Uzi Kaldor and Ephraim Eliav. volume 31 of *Advances in Quantum Chemistry*, pages 313–336. Academic Press, 1998.

[19] Lucas Visscher, Ephraim Eliav, and Uzi Kaldor. *The Journal of Chemical Physics*, 115(21):9720–9726, 2001.

[20] Jenny E Rosenthal and G Breit. *Phys. Rev.*, 41(4):459–470, aug 1932.

[21] Aage Bohr and V. F. Weisskopf. *Physical Review*, 77(1):94–98, jan 1950.

[22] J.R. Persson. *Atomic Data and Nuclear Data Tables*, 99(1):62–68, jan 2013.

[23] G. Fricke and K. Heilig. *Nuclear Charge Radii*. Landolt-Börnstein: Numerical Data and Functional Relationships in Science and Technology - New Series. Springer Berlin Heidelberg, 2004.

[24] R. Casten and R.F. Casten. *Nuclear Structure from a Simple Perspective*. Oxford science publications. Oxford University Press, 2000.

[25] R. Broda et al. *Physical Review Letters*, 74(6):868–871, 1995.

[26] H. L. Seifert et al. *Zeitschrift für Physik A Hadrons and Nuclei*, 349(1):25–32, mar 1994.

[27] E.A. McCutchan. *Nuclear Data Sheets*, 113(6):1735 – 1870, 2012.

[28] O. Sorlin et al. *Physical Review Letters*, 88(9):092501, feb 2002.

[29] K. Langanke, J. Terasaki, F. Nowacki, D. J. Dean, and W. Nazarewicz. *Physical Review C*, 67(4):044314, apr 2003.

[30] C. Guénaut et al. *Physical Review C*, 75(4):044303, apr 2007.

[31] S Rahaman et al. *The European Physical Journal A*, 34(1):5–9, oct 2007.

[32] M. L. Bissell et al. *Physical Review C*, 93(6):064318, jun 2016.

[33] P. Vingerhoets et al. *Physical Review C*, 82(6):064311, dec 2010.

[34] Meng Wang, W.J. Huang, F.G. Kondev, G. Audi, and S. Naimi. *Chinese Physics C*, 45(3):030003, mar 2021.

[35] *Physical Review C*, 82(4):041302, oct 2010.

[36] T.J. Mertzimekis, K. Stamou, and A. Psaltis. *Nuclear Instruments and Methods in Physics Research Section A: Accelerators, Spectrometers, Detectors and Associated Equipment*, 807:56–60, 2016.

[37] C. Wraith, X.F. Yang, et al. *Physics Letters B*, 771:385–391, aug 2017.

[38] X. F. Yang et al. *Physical Review C*, 97(4):044324, apr 2018.

[39] T. Otsuka, Y. Tsunoda, T. Abe, N. Shimizu, and P. Van Duppen. *Phys. Rev. Lett.*, 123:222502, Nov 2019.

[40] B. Cheal, E. Mané, et al. *Physical Review Letters*, 104(25):252502, jun 2010.

[41] E. Mané, B. Cheal, et al. *Physical Review C*, 84(2):024303, aug 2011.

[42] L. C. Aamodt and P. C. Fletcher. *Physical Review*, 98(5):1224–1229, jun 1955.

[43] N J Stone et al. *Hyperfine Interactions*, 133(1):117–120, 2001.

[44] M Keim et al. Technical report, 1995.

[45] F. Buchinger et al. *Physical Review C*, 42(6):2754–2754, dec 1990.

[46] F. Buchinger et al. *Physical Review C*, 41(6):2883–2897, jun 1990.

[47] P. Lievens et al. *Physical Review C*, 46(2):797–800, aug 1992.

[48] C. Thibault et al. *Physical Review C*, 23(6):2720–2729, jun 1981.

[49] P Lievens et al. *Europhysics Letters (EPL)*, 33(1):11–16, jan 1996.

[50] L. Xie, X.F. Yang, et al. *Physics Letters B*, page 134805, jul 2019.

[51] T. J. Procter et al. *Physical Review C*, 86(3):034329, sep 2012.

[52] Kris Heyde and John L. Wood. *Reviews of Modern Physics*, 83(4):1467–1521, nov 2011.

[53] A.N. Andreyev et al. *The European Physical Journal A - Hadrons and Nuclei*, 6(4):381–385, Dec 1999.

[54] A N Andreyev et al. *Nature*, 405(6785):430–433, 2000.

[55] N Bijnens et al. *Zeitschrift für Physik A Hadrons and Nuclei*, 356(1):3–4, 1996.

[56] P. Van Duppen et al. *Phys. Rev. Lett.*, 52:1974–1977, May 1984.

[57] P. Van Duppen, E. Coenen, K. Deneffe, M. Huyse, and J.L. Wood. *Physics Letters B*, 154(5):354 – 357, 1985.

[58] P. Van Duppen et al. *Phys. Rev. C*, 35:1861–1877, May 1987.

[59] M. Bernas et al. *Physics Letters B*, 113(4):279–282, jun 1982.

[60] S. Suchyta et al. *Physical Review C - Nuclear Physics*, 89(2), feb 2014.

[61] M. Lahanas et al. *Nuclear Physics A*, 455(3):399 – 412, 1986.

[62] B. Fogelberg. *Physics Letters B*, 37(4):372 – 374, 1971.

[63] K Nomura et al. *PHYSICAL REVIEW C*, 95:64310, 2017.

[64] J. J. Sun et al. *Physics Letters, Section B: Nuclear, Elementary Particle and High-Energy Physics*, 734:308–313, jun 2014.

[65] A. D. Ayangeakaa et al. *Physics Letters, Section B: Nuclear, Elementary Particle and High-Energy Physics*, 754:254–259, mar 2016.

[66] A. D. Ayangeakaa et al. *Physical Review Letters*, 123(10):102501, sep 2019.

[67] K Wrzosek-Lipska and L P Gaffney. *Journal of Physics G: Nuclear and Particle Physics*, 43(2):024012, jan 2016.

[68] N.V. Zamfir and R.F. Casten. *Physics Letters B*, 260(3):265 – 270, 1991.

[69] E. A. McCutchan et al. *Phys. Rev. C*, 76:024306, Aug 2007.

[70] Y. Toh et al. *Physical Review C*, 87(4):041304, apr 2013.

[71] C.S. Lee, P. Raghavan, and R.S. Raghavan. *Nuclear Instruments and Methods in Physics Research Section B: Beam Interactions with Materials and Atoms*, 56-57:851–854, may 1991.

[72] R Vianden. Quadrupole interaction prequencies in metals. *Hyperfine Interactions*, 10(1):1243–1272, 1981.

[73] J G Correia, H Haas, J G Marques, A A Melo, J C Soares, and the ISOLDE Collaboration. *Hyperfine Interactions*, 80(1):1321–1327, 1993.

[74] Abiodun F. Oluwole, Stephen G. Schmelling, and Howard A. Shugart. *Physical Review C*, 2(1):228–237, jul 1970.

[75] J. Christiansen, H. E. Mahnke, et al. *Physical Review C*, 1(2):613–618, feb 1970.

[76] W. J. Childs and L. S. Goodman. *Physical Review*, 141(1):15–21, jan 1966.

[77] *Physics Letters B*, 27(6):370–372, aug 1968.

[78] *Nuclear Physics A*, 150(2):282–290, jul 1970.

[79] D Riegel. Relaxation Rates of Excited Nuclei in Liquid Metals. *Physica Scripta*, 11(3-4):228–236, mar 1975.

[80] N Bräuer, F Dimmling, Th. Kornrumpf, K Nishiyama, and D Riegel. Quadrupole relaxation rates of71Ge and115Sn nuclei in liquid GaIn alloys. *Hyperfine Interactions*, 2(1):265–267, 1976.

[81] W Sahm and A. Schwenk. *Zeitschrift für Naturforschung A*, 29a:1763–1766, 1974.

[82] W. Makulski, K. Jackowski, A. Antušek, and M. Jaszuński. *Journal of Physical Chemistry A*, 110(40):11462–11466, oct 2006.

[83] W. J. Childs and L. S. Goodman. *Physical Review C*, 1(2):750–750, feb 1970.

[84] Pekka Pyykkö. *Molecular Physics*, 106(16-18):1965–1974, aug 2008.

[85] H. Haas, E. Ivanov, and E. Recknagel. *Physics Letters B*, 58(4):423–424, sep 1975.

[86] Loren Pfeiffer, T. Kovacs, G. K. Celler, J. M. Gibson, and M. E. Lines. *Physical Review B*, 27(7):4018–4026, apr 1983.

[87] María J G Borge and Klaus Blaum. *Journal of Physics G: Nuclear and Particle Physics*, 45(1):010301, nov 2017.

[88] E. Mané, J. Billowes, et al. *The European Physical Journal A*, 42(3):503–507, dec 2009.

[89] Mark Lloyd Bissell and Xiaofei Yang. Ground and isomeric state spins, moments and radii of Ge isotopes across the $N = 40$ subshell closure via laser spectroscopy at COLLAPS. Technical Report CERN-INTC-2016-035. INTC-P-472, CERN, Geneva, Jun 2016.

[90] A.R. Vernon et al. *Spectrochimica Acta Part B: Atomic Spectroscopy*, 153:61–83, mar 2019.

[91] S. Kaufmann. *Laser Spectroscopy of Nickel Isotopes with a new Data Acquisition System at ISOLDE*. PhD thesis, Institut für Kernphysik, TU Darmstadt, 2019.

[92] Á. Koszorús, X. F. Yang, et al. *Physical Review C*, 100(3):034304, sep 2019.

[93] W.J. Huang, G. Audi, et al. *Chinese Physics C*, 41(3):030002, mar 2017.

[94] W. Gins et al. *Computer Physics Communications*, 222:286–294, jan 2018.

[95] A.C. Mueller et al. *Nuclear Physics A*, 403(2):234–262, 1983.

[96] N Bendali et al. *Journal of Physics B: Atomic and Molecular Physics*, 19(2):233–238, jan 1986.

[97] W. J. Childs and L. S. Goodman. *Physical Review*, 131(1):245–250, jul 1963.

[98] Daniel Foreman-Mackey, David W. Hogg, Dustin Lang, and Jonathan Goodman. *Publications of the Astronomical Society of the Pacific*, 125(925):306–312, mar 2013.

FACULTY OF SCIENCE
DEPARTMENT OF PHYSICS AND ASTRONOMY
NUCLEAR MOMENTS
Celestijnenlaan 200D box 2418
B-3001 Leuven
anastasios.kanellakopoulos@kuleuven.be
https://fys.kuleuven.be/iks/nm